

ABSTRACT

SRIVASTAVA, SHUBHAM. Numerical Simulation of Synthesis of One-Dimensional Molybdenum Oxide Nanostructures in Flame Environment. (Under the direction of Dr. Alexei Saveliev).

The past few decades have seen a great amount of interest in the field of nanotechnology. As our world moves towards miniaturized devices nanotechnology is set to revolutionize the electronics, storage and sensing industry. Various methods for synthesis of different types of nanoparticles are being explored. A few of these processes that hold great promise for the future are the flame synthesis methods. These methods are highly efficient but at the same time it is difficult to control the morphology of the produced nanoparticles due to a high number of control parameters involved because of the complex flow processes. These issues demand a better understanding before these processes can be exploited to their maximum potential.

Most numerical methods developed cater to the simulation of spherical nanoparticles. However, it is now being increasingly understood that the shape and structure of a nanoparticle plays critical role in determining its chemical, physical and electronic properties. Therefore a high level of control on the shape of nanoparticles is highly imperative. With this purpose in mind this work proposes a novel numerical scheme to simulate the synthesis of one-dimensional nanorods and further presents mathematical simulations based on it followed by validation with experimental results.

The ability to predict the morphology of a nanoparticle formed by a synthesis process adds a distinct advantage. Therefore, intricate solutions have been found for the fluid flow and these

have been coupled to each stage of nanoparticle development, namely monomer formation, nucleation, particle growth and particle transport. The numerical scheme takes into account all the details of the complex surface phenomena taking place on a nanorod. Later, factors are studied which transition the growth characteristics of a nanoparticle from one dimensional to a spherical structure, thus encompassing all the factors that influence the particle shape.

Group characteristics of nanoparticles have also been modeled by employing methods that track the growth of the entire set of nanoparticles in the flame volume. This gives a clear picture of the growth of the particle ensemble in addition to the individual particles.

This work provides a first of its kind numerical model for one-dimensional growth of nanoparticles and establishes the control parameters to achieve controlled growth of nanorods in flames.

© Copyright 2014 Shubham Srivastava

All Rights Reserved

Numerical Simulation of Synthesis of One-Dimensional Molybdenum Oxide Nanostructures
in Flame Environment

by
Shubham Srivastava

A dissertation submitted to the Graduate Faculty of
North Carolina State University
in partial fulfillment of the
requirements for the degree of
Doctor of Philosophy

Mechanical Engineering

Raleigh, North Carolina

2014

APPROVED BY:

Dr. Alexei Saveliev
Committee Chair

Dr. Tarek Echekki

Dr. Tiegang Fang

Dr. Kevin Lyons

DEDICATION

*I dedicate this thesis to my parents for their
unconditional love and support*

BIOGRAPHY

Shubham Srivastava was born on 29th May 1984 in Agra, the city of the famous Taj Mahal, in India. He obtained his Bachelor of Science degree in Mechanical Engineering from Manipal Institute of Technology, India in 2007. To advance his knowledge in Thermal Science he enrolled as a Masters student in North Carolina State University in Fall 2009 and was awarded the Masters degree in August 2011. Owing to his deep interest in research he continued onto his PhD under the guidance of Dr. Alexei Saveliev.

ACKNOWLEDGMENTS

To begin with, I owe an enormous debt to Dr. Alexei Saveliev for giving me the opportunity to undertake this research. His guidance, inspiration and patience have been a major contributing factor to the completion of this work. To him, I owe the vital learning from this research.

I would like to express my sincere gratitude to Dr. Tarek Echehki, Dr. Tiegang Fang, Dr. Kevin Lyons and Dr. Kazufumi Ito for serving as the co advisors in my defense committee. Their valuable suggestions and advice were crucial for the completion of this manuscript.

I am very thankful to my lab mates Parth, RC, Mengbai and Kundu for their support and company. A special thanks to my roommates Tripathi Ji and Arun for all their help and for putting up with the mess of my papers and books in our house. Dileep, my friend and colleague, deserves a special mention for extending his generosity during my days of relocation.

Above all, I would like to express my heartfelt gratitude to my parents and family for all their care and never ending support. Their love has been my most valuable possession.

TABLE OF CONTENTS

LIST OF TABLES.....	ix
LIST OF FIGURES.....	x
Chapter 1 Introduction	1
1.1 Definition of Nanomaterial and One-Dimensional Nanostructures.....	1
1.2 Transition Metal Oxide Nanostructures	3
1.3 Flame Synthesis of Nanoparticles.....	5
1.3.1 Steps in Flame Synthesis of Nanoparticles	7
1.3.2 Parameters Affecting Flame Synthesis	9
1.3.3 Flame Synthesis of One-Dimensional Nanostructures	11
1.4 Numerical Modeling of Flame Synthesis of Nanoparticles.....	12
1.5 Thesis Objectives	14
1.6 Layout of the Thesis.....	15
Chapter 2 Experimental Study	16
2.1 Experimental Set-up.....	17
2.1.1 Thermophoretic Sampling Technique.....	18
2.1.2 Effect of Oxidizer Composition on the Flame	19
2.1.3 Effect of Strain Rate on the Flame.....	20
2.2 Experimental Results	21
2.2.1 Nanoparticle synthesis from 1.00 mm diameter molybdenum probe	22
2.2.2 Nanoparticle Synthesis from 0.75 mm Diameter Molybdenum Probe.....	26
2.3 Conclusions of Experimental Results	28
Chapter 3 Brief Introduction to the Numerical Model	30
3.1 Details of the Growth Model	32
3.2 Assumptions.....	33
Chapter 4 Flame Modeling	36
4.1 Opposed Flow Flame Model.....	37
4.2 Transport Properties	40
4.2.1 Mixture Averaged Properties	41
4.3 Solution Procedure.....	43
4.4 GRI mechanism	43

4.5 Results of the Flame Model	44
Chapter 5 Monomer Formation	50
5.1 Molybdenum Oxidation	51
5.2 Oxidation Regimes of Molybdenum.....	52
5.3 Mechanism of Molybdenum Oxidation	55
5.4 Rate Equation for Molybdenum Oxidation.....	56
5.5 Calculation of Molybdenum Probe Temperature and Molybdenum Dioxide Concentration.....	60
5.6 Verification of the Molybdenum Oxidation Kinetic Model	61
Chapter 6 Nucleation.....	63
6.1 Classical Nucleation Theory (CNT)	65
6.1.1 Assumptions in CNT.....	69
6.2 Lothe and Pound	69
6.3 Reiss, Katz and Cohen	71
6.4 On the Use of Classical Nucleation Theory in this Research	73
6.5 Verification of Implementation of Classical Nucleation Theory.....	74
6.5.1 Nucleation with varying temperature.....	75
6.5.2 Nucleation with varying supersaturation ratio	77
6.6 Conclusion for Nucleation Theory.....	79
Chapter 7 Nanorod Growth Model.....	80
7.1 Rough Growth.....	81
7.2 Layered Growth	81
7.3 Growth Mechanism in Molybdenum Oxide Nanorods.....	84
7.3.1 Chemical Potential and Supersaturation Ratio	84
7.3.2 Phase Transition and Supersaturation Ratio	85
7.3.3 Variation of Growth Pattern with the Driving Force	87
7.3.4 Effect of Probe Diameter on Nanoparticle Morphology.....	88
7.4 Different Growth Modes on Nanorod Surfaces	89
7.5 Mechanism of Growth on Nanorod Tips	90
7.5.1 Direct Impingement	92
7.5.2 Diffusion of Atoms from Lateral Sides	94
7.6 Mechanism of Growth of Lateral Surfaces	98

Chapter 8 Particle Transport Model.....	101
8.1 Drag.....	103
8.1.1 Stokes' Law	104
8.2 Thermophoretic Force.....	107
8.2.1 Theory	108
8.2.2 Thermophoretic Force in the Free Molecular Regime.....	108
8.2.3 Thermophoretic Force in the Continuum Regime	109
Chapter 9 Results of the Growth Model.....	112
Chapter 10 General Dynamic Equation Modeling	129
10.1 General Dynamic Equation.....	130
10.1.1 Sectional Methods.....	132
10.1.2 Monte Carlo Methods	133
10.1.3 Moment Methods	133
10.2 Method of Moments.....	134
10.2.1 Physical Significance of Moments.....	134
10.2.2 General Dynamic Equation for Method of Moments	135
10.2.3 Restrictions to Method of Moments	136
10.2.4 Method of Moments with Interpolative Closure.....	137
10.3 Quadrature Method of Moments.....	138
10.3.1 Quadrature-Based Closure	139
10.3.2 Product Difference Algorithm	140
10.3.3 Verification of the Quadrature Method of Moments Algorithm	141
10.4 Quadrature Method of Moments Applied to Nanorod Synthesis	147
10.4.1 Growth	148
10.4.2 Nucleation	150
10.4.3 Particle Transport.....	151
10.4.4 Final Equations and Procedure for Quadrature Method of Moments.....	151
10.5 Results of Quadrature Method of Moments applied to Nanorod synthesis	153
Chapter 11 Conclusions.....	158
REFERENCES.....	160
APPENDICES.....	173
Appendix A: Derivation for Rate of Oxidation for Molybdenum.....	174
Appendix B: Product – Difference Algorithm.....	178

Appendix C: Derivation for the Thermophoretic Force Expression in Free Molecular Regime.....	180
Appendix D: Solution Scheme for Calculating the Diffusion Flux from the Lateral Surfaces.....	182
Appendix E: Dillmann-Meier Theory.....	184
Appendix F: Mass Diffusivity Data for Various Species using Cantera.....	189
Appendix G: Thermal Diffusivity Data for Various Species using Cantera.....	191

LIST OF TABLES

Table 5-1: Thermochemical data for Oxides of Molybdenum	53
Table 5-2: Classification scheme; oxidation of molybdenum (Gulbransen et. al., 1963)	54
Table 5-3: Comparison of calculated temperature of molybdenum probe to the experimental temperature.....	62
Table 8-1: Values for various Cunningham corrections constants.....	106
Table 10-1: Inversion of initial moments for figure 10-1.....	144

LIST OF FIGURES

Figure 1-1: TEM images of BaTiO ₃ nanowires (Cao, 2004).....	2
Figure 1-2: SEM images of ZnO nanobelts (Cao, 2004).....	3
Figure 1-3: Transition metals shown on the periodic table (Wikipedia, 2014)	4
Figure 1-4: Different burner configurations (a) premixed flat flame burner (b) counterflow diffusion flame burner (c) coflow diffusion flame burner (Rosner, 2005)	6
Figure 1-5: Steps in particle formation in flames (Roth, 2007).....	9
Figure 2-1: Schematic representation of the set-up (Desai, 2010).....	17
Figure 2-2: Thermophoretic sampling technique (Merchan-Merchan, et al., 2003)	18
Figure 2-3: Methane flames at a strain rate of 20 s ⁻¹ formed by a) 21% O ₂ , 79% N ₂ b) 50% O ₂ , 50% N ₂ c) 100% O ₂ (Desai, 2010).....	20
Figure 2-4: Flames at various strain rates (35% O ₂ + 65% N ₂): (a) SR = 10 s ⁻¹ (b) SR = 20 s ⁻¹ (c) SR = 30 s ⁻¹ (Desai, 2010).	21
Figure 2-5: Schematic of probe position (Desai, 2010).....	22
Figure 2-6: Low resolution TEM image of nanoparticles collected at Z = 12 mm from the fuel nozzle (Desai, 2010).....	23
Figure 2-7: TEM images of nanostructures obtained at Z = 10 mm from the fuel nozzle (Desai, 2010).....	24
Figure 2-8: Magnified images of the nanoparticles sampled at Z = 10 mm (Desai, 2010). ...	25
Figure 2-9: Low resolution TEM image of nanoparticles formed by 0.75 mm probe at Z = 10 mm (Desai, 2010).....	27

Figure 2-10: Magnified TEM images of nanoparticles formed by 0.75 mm probe (Desai, 2010)	28
Figure 3-1: Subdivisions of the numerical model.....	32
Figure 4-1: Schematic diagram of opposed flow diffusion flame.	37
Figure 4-2: Chemical species concentration profiles for counter-flow oxy-methane flame. .	46
Figure 4-3: Temperature of the flame.....	47
Figure 4-4: Gas velocity as a function of axial position.	48
Figure 6-1: Distribution functions of embryos of different sizes according to Volmer and Becker-Doring theories of nucleation (Christian, 2002).....	68
Figure 6-2 Comparison of all three theories to experiment (Hung, et al., 1989).....	73
Figure 6-3: Rate of nucleation as a function of temperature at supersaturation ratios 5, 7, 10.	75
Figure 6-4: Size of critical nucleus vs Temperature for Supersaturation ratio = 10, 7, 5.....	76
Figure 6-5: Rate of nucleation as a function of supersaturation ratio at T = 300, 400, 500 K	77
Figure 6-6: Size of critical nucleus vs saturation ratio at T = 300, 400, 500 K.....	78
Figure 7-1: 2D nucleation	83
Figure 7-2: Growth by screw dislocation (Venables, 1994).....	83
Figure 7-3: Variation in crystal growth pattern with the driving force (Sunagawa, 2005)	87
Figure 7-4: Schematic of a nanorod growth process showing direct impingement of atoms on the rough ends, diffusion of atoms on the nanorod surface, and 2-D layered nucleation.....	90
Figure 7-5: Attachment of monomer atoms to nanorod ends.	91
Figure 7-6: Variation of free energy across phases	92

Figure 7-7: Various atomic processes taking place on the surface.....	94
Figure 7-8: Depiction of the monomer flux and the diffusion flux of atoms (Markov, 1941)	98
Figure 9-1: Zones in the flame for various nanorod growth processes.....	113
Figure 9-2: Variation of saturation pressure of MoO ₂ through the nanoparticle trajectory with the growth timespan.....	115
Figure 9-3: Rate of nucleation for 0.75 mm and 1.00 mm molybdenum probes during the nucleation timespan	117
Figure 9-4: Variation of monomer partial pressure with the growth timespan.....	118
Figure 9-5: Variation of atomic flux on the growing nanorods with the growth timespan ..	119
Figure 9-6: Variation of length and diameter of nanorod from 1.00 mm diameter probe with the growth timespan	121
Figure 9-7: Variation of length and diameter of nanorod from 0.75 mm diameter probe with growth timespan.....	123
Figure 9-8: Comparison of the contribution to the rate of increase in nanorod length by surface diffusion and direct impingement with growth timespan.....	124
Figure 9-9: Trajectory followed by the nanoparticles from 1.00 mm and 0.75 mm probes during the growth timespan	126
Figure 9-10: Variation of aspect ratio of nanoparticles with monomer partial pressure	127
Figure 10-1: Solution of the Khrgian-Mazin size distribution, QMOM (solid), analytical (dots).....	143
Figure 10-2: Procedure for Quadrature Method of Moments.....	147
Figure 10-3: Variation of 0th moment during nucleation with nucleation timespan.....	154

Figure 10-4: Variation of 1st moment during growth with growth timespan..... 155

Figure 10-5: Variation of higher moments for the nanorod size distribution with growth timespan 157

Chapter 1

Introduction

1.1 Definition of Nanomaterial and One-Dimensional

Nanostructures

Nanomaterials are defined as structures with dimensions that fall between the size range of 1 to 100 nm. This miniaturization of material is fairly new and thus has been the subject of growing attention of modern science. Through successful efforts in this field many new opportunities can be realized especially pertaining to memory storage, electronics and computing. Nanomaterials are quite fascinating in many respects, mainly in the peculiar properties that they exhibit. Owing to their extremely miniscule size the properties of nanostructures are considerably different from their bulk materials (Cao, 2004). For instance, the melting temperature of many nanostructures has been found to be significantly less than the bulk material (sometimes by as much as 1000°C). Materials seem to lose their ferromagnetic behavior when reduced to nanoscale dimensions. Many of the properties of nanomaterials are also attributed to their very high surface to volume ratio. A small fraction of atoms in a bulk substance are present on the surface whereas in nanoparticles this fraction

is rather high and ensures that many constituent atoms are exposed on their surface. A keen interest in the production of nanoparticles was spurred by their display of some highly desirable traits such as increased catalytic activity (Beck, et al., 1992), superplasticity (Karch, et al., 1987) and higher theoretical densities. The products manufactured with some nanomaterials show higher toughness (Karch, et al., 1990) and ductility. One-dimensional nanostructures are commonly defined as nanoparticles with an aspect ratio greater than or equal to 3. One-dimensional nanostructures include a wide variety of products like whiskers, fibers, nanowires and nanorods. Although whiskers and nanorods are generally considered shorter than nanowires and fibers. 1-D nanostructures, as generally accepted, provide a sound basis to investigate the dependence of electrical and thermal transport on the dimensionality of nanostructures.

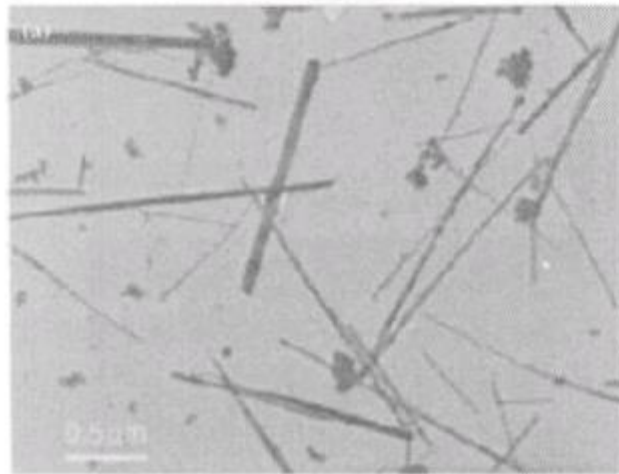


Figure 1-1: TEM images of BaTiO₃ nanowires (Cao, 2004).

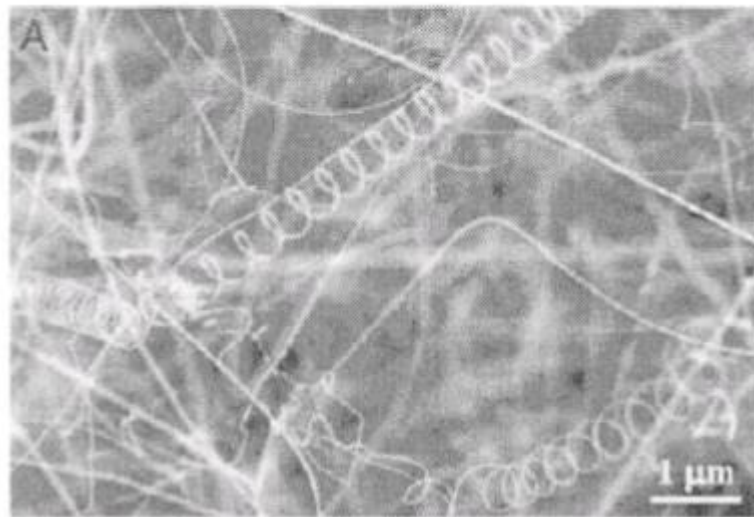


Figure 1-2: SEM images of ZnO nanobelts (Cao, 2004).

1-D nanostructures possess even higher surface to volume ratios making them perfectly suited to sensing and catalytic applications. Their surfaces have been modified to implement them as highly sensitive, real time sensors for pH and biological species (Cui, et al., 2001). The charge on the surface of the particle changes as a result of the adsorption. Recently, (Kind, et al., 2002) found the conductance of ZnO nanowires to be extremely sensitive to ultraviolet light exposure thus making it possible for them to make highly sensitive electrical switches.

1.2 Transition Metal Oxide Nanostructures

The International Union of Pure and Applied Chemistry (IUPAC) defines a transition metal as “an element whose atom has a partially filled *d* sub-shell or which can give rise to cations

with an incomplete d sub-shell.” They are the elements occupying groups 3 to 12 on the periodic table.

Main-group Elements		Transition Metals										Main-group Elements					
H																	
Li	Be																H He
Na	Mg											B	C	N	O	F	Ne
K	Ca	Sc	Ti	V	Cr	Mn	Fe	Co	Ni	Cu	Zn	Al	Si	P	S	Cl	Ar
Rb	Sr	Y	Zr	Nb	Mo	Tc	Ru	Rh	Pd	Ag	Cd	Ga	Ge	As	Se	Br	Kr
Cs	Ba	La	Hf	Ta	W	Re	Os	Ir	Pt	Au	Hg	In	Sn	Sb	Te	I	Xe
Fr	Ra	Ac	Rf	Ha	106	107	108	109				Tl	Pb	Bi	Po	At	Rn

Lanthanides	Ce	Pr	Nd	Pm	Sm	Eu	Gd	Tb	Dy	Ho	Er	Tm	Yb	Lu
Actinides	Th	Pa	U	Np	Pu	Am	Cm	Bk	Cf	Es	Fm	Md	No	Lr

Figure 1-3: Transition metals shown on the periodic table (Wikipedia, 2014)

Transition metals have unique properties because of their oxidation states. They form wide variety of colored compounds because of their electronic transitions from a ligand orbital to a metal orbital when the metal is in a high oxidation state or from a metal to a ligand when the metal is in a low oxidation state. They also exhibit paramagnetic properties when they have one or more unpaired d electrons. Ferromagnetism is found when individual atoms are

paramagnetic and the spin vectors are aligned parallel to each other (Figgis, et al., 1960). Owing to their oxidation states they can also make a plethora of ionic compounds. When oxygen combines with transition metals it gives rise to many interesting properties. Silicon oxide and titanium oxide are used for biomolecule immobilization by exploiting their large surface area (Zhuo, et al., 2005). Zirconium oxide is used for catalytic action due to its high surface energy (Xiao, et al., 2003). In recent years some effort has been devoted to the synthesis of molybdenum oxide due to its unique electronic and catalytic properties (Zhou, et al., 2003). They have found tremendous use in petroleum refining and recording media (Song, et al., 2011) (He, et al., 2003).

1.3 Flame Synthesis of Nanoparticles

Flame synthesis has gained immense popularity as a method for producing nanoparticles. The volumes of commercial flame production of nanoparticles has scaled to several million metric tons per annum with around 100 metric tons per day (Kammler, et al., 2001). The success and wide spread application of combustion synthesis is chiefly attributed to the following advantages –

- i. the heat of combustion easily activates precursor pyrolysis, hydrolysis and vaporization
- ii. many parameters can be varied to control the final morphology of the nanoparticles
- iii. high heat allows the production of particles to be conducted under high purity conditions

- iv. flame processes can often be completed in a single step as compared to multiple steps in wet-chemical methods
- v. flame methods are highly scalable

There are different configurations of flames that are used for nanoparticle synthesis. The three basic type of burners are shown in Fig 1-4 .

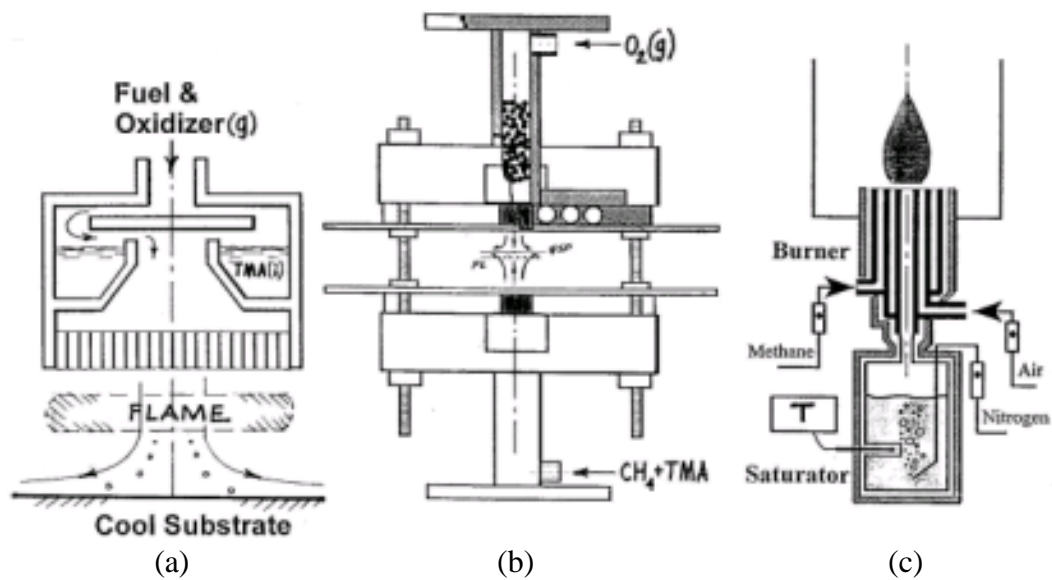


Figure 1-4: Different burner configurations (a) premixed flat flame burner (b) counterflow diffusion flame burner (c) coflow diffusion flame burner (Rosner, 2005)

Premixed flat flame burner

This kind of a burner configuration is used for oxide synthesis under sub-atmospheric conditions. The flow of fuel and oxidizer takes place either from the top or bottom to pass

over a vaporizing precursor. The flame is stabilized between the burner and a cooled substrate (Zhao, et al., 2005)

Counterflow diffusion flame burner

In a counterflow burner the particle precursor vapors are added either to the gaseous fuel or the gaseous oxidizer. The end product is produced in the confined flame (Chung, et al., 1985) (Zachariah, et al., 1989) (Kim, et al., 2005)

Coflow diffusion flame burner

In a coflow burner the gaseous fuel and the oxidizer streams are separated from the stream carrying the precursor particles. This capability can be used to control the location of particle inception in the flame (Zhu, et al., 1997).

1.3.1 Steps in Flame Synthesis of Nanoparticles

The formation of nanoparticles involves a series of steps as depicted in Figure 1-5. The building blocks of the nanoparticles are monomers. Monomers are distinctly identifiable particles having characteristic dimensions which come together to form clusters. Monomers are formed by the interaction of flame with the raw material introduced. Once the interaction happens a series of chemical reactions occur converting the raw material into embryonic units. Some of these monomers polymerize to form nuclei which are the primary particles. Nucleation can either be homogeneous or heterogeneous in nature (Wooldridge, 1998). When nuclei are generated by the condensation of the gaseous monomers itself the process is called *homogeneous nucleation*. At low supersaturation ratio of monomers the condensation

takes place on some existing nuclei without formation of new ones. This process is called *heterogeneous nucleation*. These nuclei then collide to form aggregates providing sites for heterogeneous deposition. The aggregates grow by surface deposition of monomers on these structures. When they are sufficiently large they may even undergo coalescence to form even bigger structures thus giving them final shape. If the characteristic time for coalescence has the same order as the characteristic time for collision, branchy or hard aggregates are formed. All these processes are highly susceptible to variables like pressure, temperature and residence time.

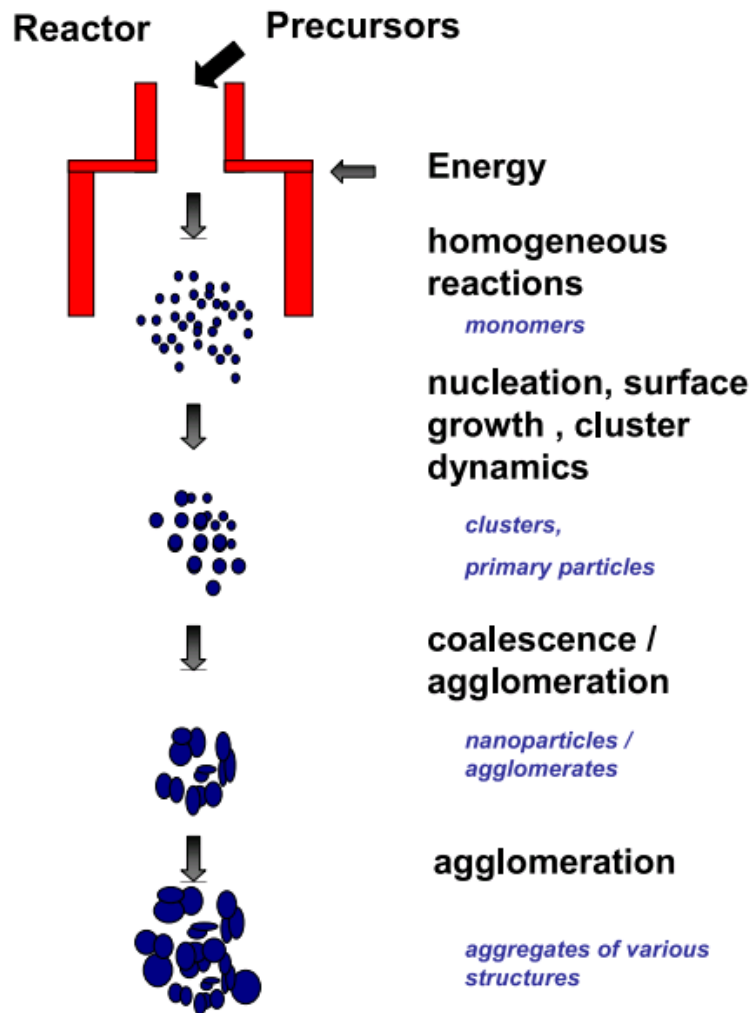


Figure 1-5: Steps in particle formation in flames (Roth, 2007)

1.3.2 Parameters Affecting Flame Synthesis

In the flame process nanoparticles are formed by gas-to-particle conversion mechanism. This mechanism has a characteristic of producing non-agglomerated particles. For production of a large quantity of nanoparticles like in industry turbulent co-flow reactors are used whereas

for the purpose of experimental examination laminar flames are preferred as turbulence brings in other uncertainties. The process is affected by a number of parameters chiefly temperature, particle residence time, precursor concentration and additives. Irrespective of the configuration of the flame the effect of these parameters remains rather unchanged. Other variables like flame stoichiometry, gas flow rate etc. can be altered to control the particle morphology.

It has been observed that increasing precursor loading resulted in an increase in the particle size. This effect has been attributed to increased agglomeration of the primary particles since the increase in precursor loading favors surface growth onto existing particles. The increased collision frequency diminishes the available precursor concentration for any further homogeneous nucleation. The precursor loading also increased the density due to higher agglomeration. This surge in density provides more number of attachment points in the particle and sintering occurs more rapidly. The precursor also affects the process temperature if a considerable amount of heat is provided by the combustion of the precursor increasing the adiabatic flame temperature (Kammler, et al., 2001).

Flame temperature and particle residence time have been shown to be the most critical parameters in determining the particle morphology. An increase in temperature enhances the precursor reactions thereby providing a boost to the monomer production but this also enhances the sintering process. Therefore an increase in temperature results in smaller primary particles if they do not get time to coalesce. The use of oxygen instead of air also increases the product size as the precursor oxidation as well as growth and sintering are enhanced.

Burner geometry also plays a significant role in the process (Wegner, et al., 2002). Reducing the burner diameter by a quarter they were able to produce silica particles that were four times smaller. This was the result of the enhanced mixing of gases in the smaller reactor which lead to a steeper temperature gradient. The smaller burner diameter also resulted in higher outlet velocities thus reducing the residence time of the particle and consequently there is less time for their growth and sintering.

The particle size can also be controlled by using additives. These do affect the purity of the product but can still be used to monitor the crystallinity and extent of agglomeration in the nanostructure. Small amounts of AlCl_3 are infused to promote the formation of rutile titania and to slow down the aggregation of the product (Braun, 1997). Stable and fully oxidized nanoparticles are normally obtained in flames burning under lean conditions. The oxygen stoichiometry in the particles depends on the distribution of oxygen concentration in the flames. The stoichiometry of oxide particles affect their crystalline morphology and lattice structure. Many metals exist in various oxidation states and can form a variety of sub-oxides.

1.3.3 Flame Synthesis of One-Dimensional Nanostructures

Limited work is available on flame synthesis of one-dimensional nanostructures as opposed to spherical nanostructures. These efforts include gas phase as well as solid support synthesis utilizing flame aerosol, flame spray pyrolysis, plasma flame synthesis and flame gradient method. SnO_2 nanorods were prepared from the flame aerosol process using dopant species like Fe, Li and Zn (Liu, et al., 2010) (Bakrania, et al., 2007). Dopants increase the tendency

to form nanorods especially Fe. The dimensions observed were 200 nm in length and 20 nm in diameter. Carrier gases also play a vital role.

ZnO nanorods have also been prepared by using flame spray pyrolysis in a coflow diffusion flame (Height, et al., 2006). Here too dopant species were used, primarily In, Sn and Li. The formation of nanorods took place in the vapor phase and depends on the dopant valency. The nanorods produced were about 150 nm in diameter and 4 μm to 200 nm in length. Layer growth mechanism is responsible for this process. ZnO nanorods have also been prepared by using oxygen microwave plasma torch flame (Hong, et al., 2006).

1.4 Numerical Modeling of Flame Synthesis of Nanoparticles

Flame methods for nanoparticle synthesis are quite complex and it is difficult to control their every aspect. This is one of the prime reasons that a perfect numerical simulation of nanoparticle synthesis still remains elusive. In flame processes the chemical reaction and particle growth take place simultaneously and both are extremely fast processes. The complex fluid flow accompanied with short residence time makes it extremely difficult to capture the physics (Pratsinis, 1998). Flame methods also contain a wide array of particle sizes and shapes which makes the particle characterization very difficult. The essence of modeling is to gain knowledge to increase the quality and scale of production. For this purpose intricate understanding of physical and chemical processes in formation and transport is required.

A literature review in the subject reveals various modeling strategies ranging from thermodynamics to stochastic methods and many other approaches that have been undertaken. (Barnard, et al., 2005) has suggested a thermodynamic model to describe the shape of nanoparticle as a function of size and chemical environment. This model is based on the concept of minimizing the total energy and hence used equilibrium thermodynamics. Although this model was able to successfully predict crystal structures but being based on equilibrium principles was unable to model kinetic growth of crystals. Kinetic models have also been developed based on the assumption that under non-equilibrium conditions different crystal planes have different kinetic parameters (Xu, et al., 2007). Although these models work whether the growth is in the solvent or the vapor phase, they are unable to take into account surface atomic processes. Flames contain polydisperse particles and non-spherical fractal structures for which non-spherical particle dynamic simulations and flame analysis have not been carried out. The simulation of synthesis of fine titania done by (Johannessen, et al., 2000) employed a monodisperse model thus losing the effect of polydispersity. Similarly, (Yu, et al., 1998) developed a discrete sectional model to be applied to flames but once again assumed spherical particles.

Population Balance Equation (PBE) has proved to be immensely helpful in modeling the population of particles undergoing nucleation, coalescence and sintering. The PBE can either be univariate or bivariate depending on the requirements. Monodisperse models typically use volume of the particle for characterization but if sintering plays an important role in the particle growth then an additional variable for surface area is also used.

Another approach towards solving the PBE is Sectional Methods. They divide the entire distribution into bins and track the evolution of particles in each bin. Coupled differential equations are formed together with the neighboring bin and the accuracy depends on the discretization schemes used. However, these techniques suffer from the problem of numerical diffusion to neighboring bins. This problem can be solved by increasing the number of bins but that makes it computationally more expensive. These methods are easy to solve but run into high computational cost (Hounslow, et al., 1988).

Motivated by this, the work done in this thesis has been aimed at developing a numerical model which is able to predict the shape of non-spherical (typically one-dimensional nanostructures) as they are grown in a flame environment in the gas phase. Due consideration has been given to the atomic processes taking place in each individual nanoparticle and also towards the collective dynamics of the entire group of particles undergoing morphological changes in the flame volume (Srivastava, et al., 2014).

1.5 Thesis Objectives

The goal of this thesis is to develop an innovative numerical scheme for simulating the growth of one-dimensional nanostructures in flames and to validate it using the results from previous experiments. We have chosen an opposed flow flame configuration involving precursor transport and aggregation. An attempt has been made to incorporate all physical processes possible.

A counterflow flame has been simulated which interacts with the nanoparticles right from inception to final development. Detailed molybdenum surface oxidation chemistry has been employed to simulate source precursor formation. Every development stage from nucleation to surface growth has been thoroughly examined along with flame-particle interaction and particle transport. Results of the model have been compared to the experimental studies. A statistical analysis has also been performed on the synthesis process by using the Quadrature Method of Moments to study the collective characteristics of the group of nanoparticles.

1.6 Layout of the Thesis

Chapter 2 gives the experimental details of the Flame Gradient Method against which the simulation results have been compared. Chapter 3 introduces the basics of growth mechanism of nanorods in flames followed by the subparts of the model in Chapters 4, 5, 6, 7 and 8. These chapters are Flame modeling, Monomer formation, Nucleation, Nanorod growth and Particle transport respectively. Together they form the entire nanorod growth mechanism. Chapter 9 discusses the results of the growth model and Chapter 10 explains the implementation of Quadrature Method of Moments to solve for the size distribution of the particles.

Chapter 2

Experimental Study

An experimental study into the formation of one-dimensional molybdenum oxide nanostructures has been carried out in the University of Oklahoma (Merchan-Merchan, et al., 2009). They explored the synthesis of transition metal oxide nanostructures produced in the gas phase in oxy-methane flames through the *Flame Gradient Method*. More details can be found at (Desai, 2010). Their findings have been used to validate the numerical study undertaken in this research. For the purpose of providing an insight into the Flame Gradient Method and physical realm of things some information about the experiments is being provided here.

2.1 Experimental Set-up

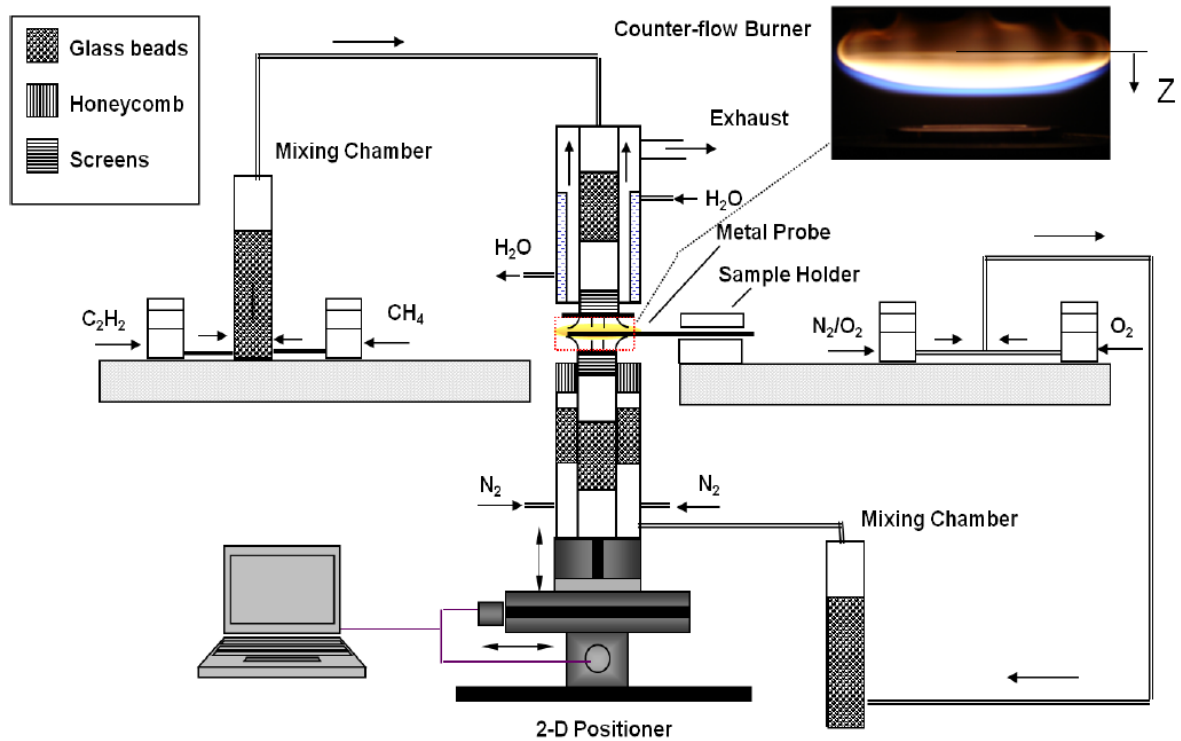


Figure 2-1: Schematic representation of the set-up (Desai, 2010).

In the Flame Gradient Method a counterflow flame is utilized to produce one-dimensional nanostructures. The fuel used is 96% methane with 4% acetylene and the oxidizer utilized is 50% oxygen and 50% nitrogen. The fuel is introduced from the top nozzle whereas the oxidizer inlet is from the bottom nozzle. The two streams impinge onto each other to form an opposed flow diffusion flame. The major advantage of a diffusion flame is the presence of high gradients of temperature and chemical species concentrations. Depending on the requirements various zones of the flame can be employed for nanoparticle formation. There

is also an inlet of nitrogen from the outer annulus of the oxidizer nozzle. This layer of nitrogen is maintained to contain the diffusion flame and also to shield it from external air effects. The nozzle separation is 25.4 mm and all experiments were performed at a strain rate of 20 s^{-1} . Before combustion all the gasses are thoroughly mixed in the mixing chambers.

2.1.1 Thermophoretic Sampling Technique

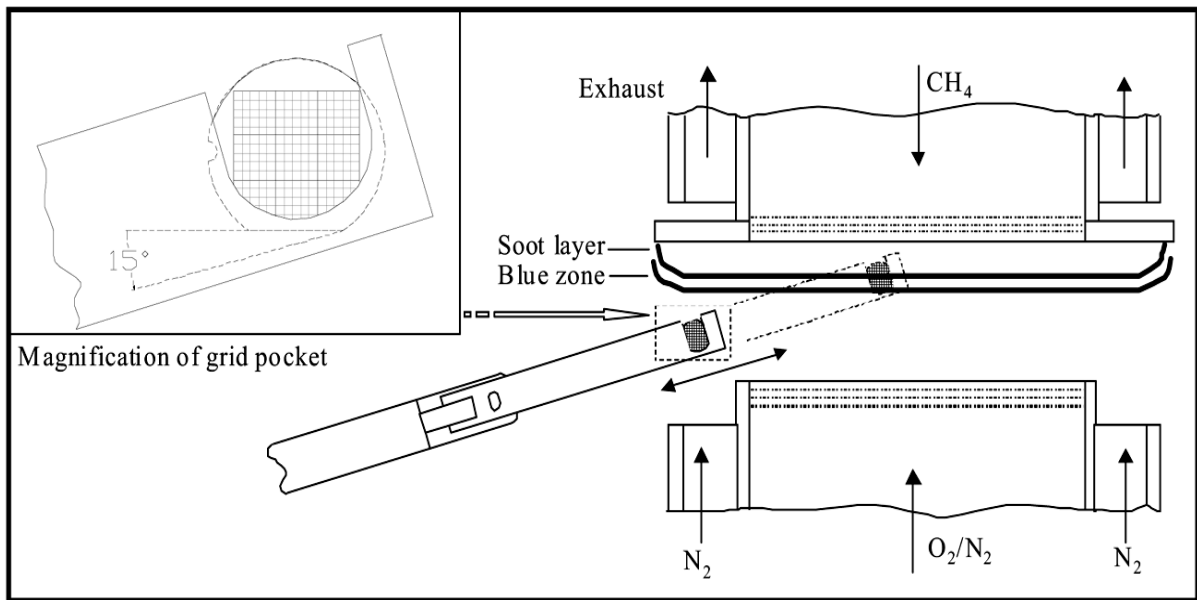


Figure 2-2: Thermophoretic sampling technique (Merchan-Merchan, et al., 2003)

Thermophoretic sampling technique is extensively used to capture particles in flame volume and has been applied in the study of soot formation (Megaridis, et al., 1988). Similar method has been applied in this experimental study to sample the nanoparticles formed in the flame. The counter-flow diffusion flame possesses steep gradients in temperature and velocity and

hence the growth of nanoparticles occurs rather quickly in a thin stretch of the flame. For this reason the thermophoretic sampling has to be extremely precise. The grid used here has a copper mesh and has a thin film of 20 nm of pure carbon on one side. It is placed at an angle of 15° with plane perpendicular to the burner axis to minimize the travel time of the grid in the particle formation area. Care should be taken while inserting the thermophoretic grid into the flame because of two main reasons.

- i. The grid should not stay so long as to alter the flow of gases in the flame
- ii. The duration of the sampling process should be long enough to capture the nanoparticle effectively.

The nanoparticles captured were analyzed using a high-resolution transmission electron microscopy (TEM) to analyze their structure and morphology.

2.1.2 Effect of Oxidizer Composition on the Flame

The opposed flow diffusion flame is composed of two distinct regions –

- i. Blue zone – rich in oxygen atoms
- ii. Yellow zone – rich in carbon atoms

For the synthesis of metal oxide nanostructures the molybdenum probe should be introduced into the blue zone. By varying the content of oxygen in the oxidizer the thickness of these zones can be controlled.

Figure 2-3 is obtained at a strain rate of 20 s^{-1} by varying the concentration of oxygen from 21% all the way to 100% (Desai, 2010)

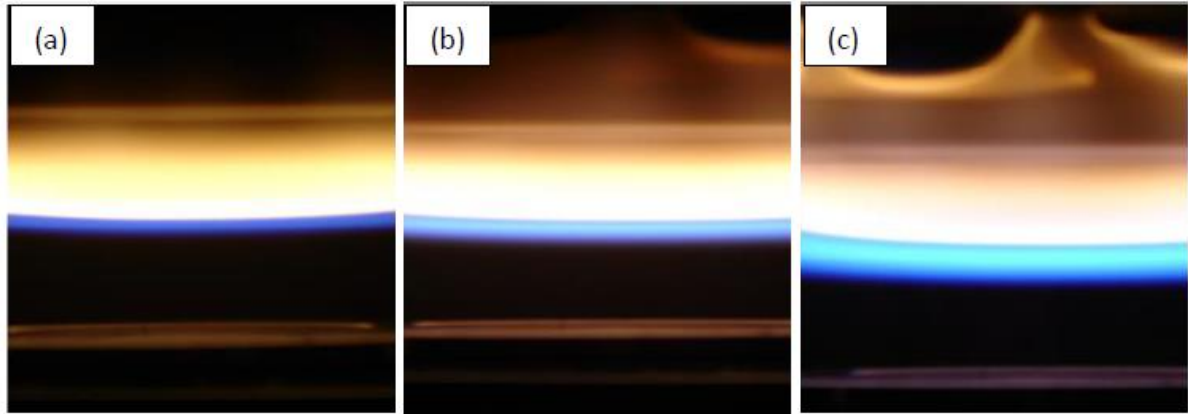


Figure 2-3: Methane flames at a strain rate of 20 s^{-1} formed by a) 21% O_2 , 79% N_2 b) 50% O_2 , 50% N_2 c) 100% O_2 (Desai, 2010)

As can be seen from the Figure 2-3 21% O_2 flame has a huge yellow zone whereas 100% O_2 flame has a blue zone. On the other hand 50% O_2 and 50% N_2 has an ideal thickness of both blue and yellow zone and hence this combination has been used in the experiments.

2.1.3 Effect of Strain Rate on the Flame

At lower strain rates the yellow zone is most distinct and bright. This signifies an active carbon rich zone. As the strain rate increases the blue zone also increases in thickness but beyond a certain limit of strain rates the thickness of the blue zone again starts to recede. Therefore, the ideal strain rate for the experiments is 20 s^{-1} as shown in the Figure 2-4.

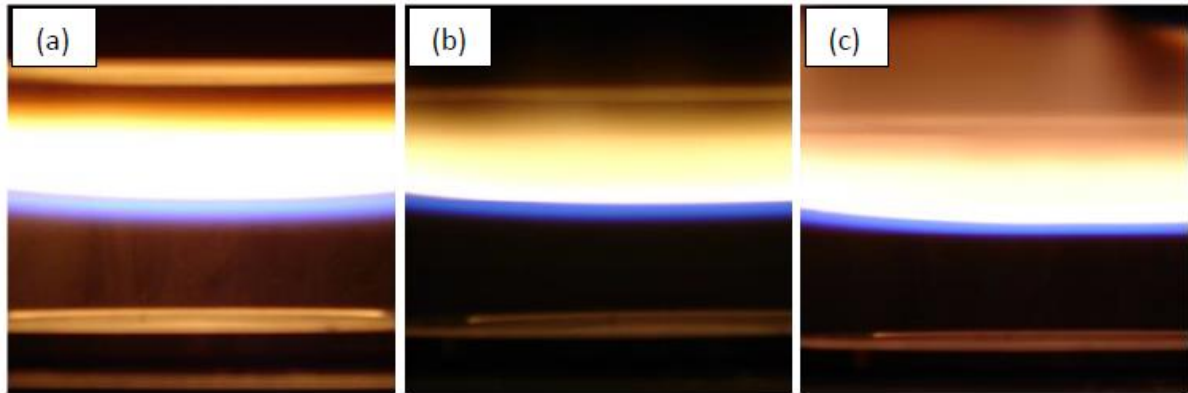


Figure 2-4: Flames at various strain rates (35% O₂ + 65% N₂): (a) SR = 10 s⁻¹(b) SR = 20 s⁻¹(c) SR = 30 s⁻¹ (Desai, 2010).

2.2 Experimental Results

The *Flame Gradient Method* involves the production of nanomaterial through the interaction of a metal in the form of a probe and the counter-flow flame. For molybdenum oxide nanoparticles molybdenum probes of different diameters act as the material source. Two probes of diameters 1.00 mm and 0.75 mm are used. These metal probes are inserted into the flame at a distance of 13 mm from the fuel nozzle. In an oxy-methane counter-flow flame temperature gradients of 2000 K/cm exist along with steep chemical gradients. Due to this the interaction of the probe with the flame is strongly affected by the probe position. The synthesized nanoparticles are sampled out using the thermophoretic technique at three levels in the flame volume ($Z = 12\text{mm}, 11\text{ mm}, 10\text{ mm}$) as measured from the fuel nozzle.

The flame environment causes oxidation and material etching from the molybdenum probes. The oxidized material is then carried with the flame and is later collected by the

thermophoretic grid. Significant modifications occur in the transported nanomaterial and it forms nanoparticles of different morphologies depending on the ambient conditions in the flame.

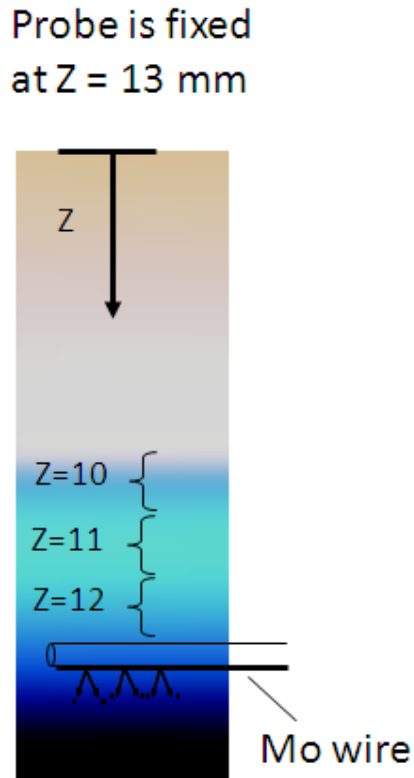


Figure 2-5: Schematic of probe position (Desai, 2010).

2.2.1 Nanoparticle synthesis from 1.00 mm diameter molybdenum probe

The TEM image shown in Figure 2-6 shows the nanoparticles collected thermophoretically at a distance of 12 mm from the fuel nozzle when 1.00 mm diameter molybdenum probe was used as the material source.

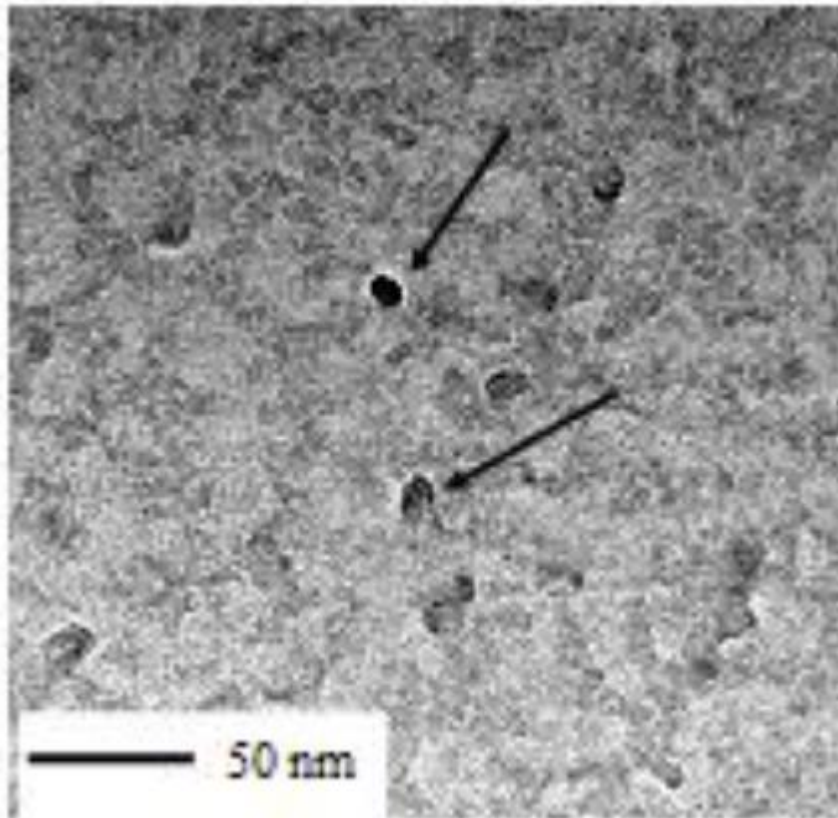


Figure 2-6: Low resolution TEM image of nanoparticles collected at $Z = 12$ mm from the fuel nozzle (Desai, 2010).

The figure shows a plethora of small particles along with some heavy nucleated particles. The size of the nucleated particles is less than 8 nm and they are invariably spherical in shape. Their amorphous nature suggests that the particles are still in the process of maturing and the vapor to solid transition has just begun.

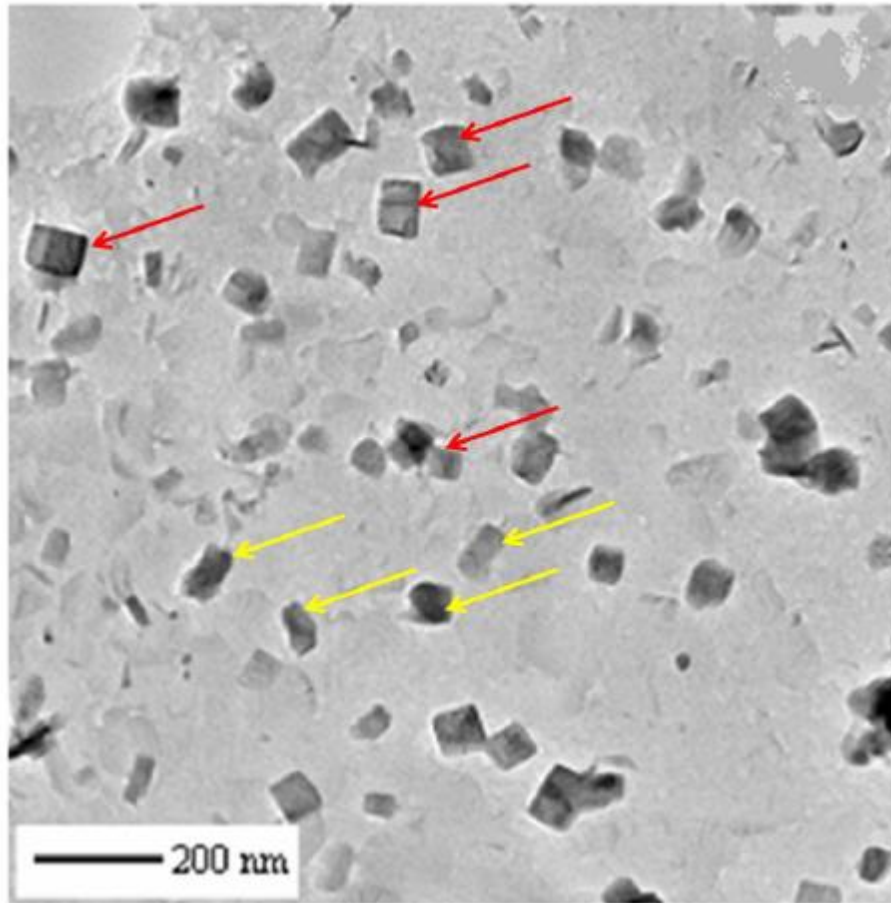


Figure 2-7: TEM images of nanostructures obtained at $Z = 10$ mm from the fuel nozzle

(Desai, 2010)

As the molybdenum oxide vapors travel through the flame they condense and undergo a phase transformation to form solid nanoparticles. This phase change depends on the residence time of the particles which increases as the sampling height of the experiments increases. At a distance of $Z = 10$ mm from the fuel inlet the particles show exciting

transformations (Figure 2-7). As compared to Figure 2-6 the nanostructures here have a more pronounced morphology. The structures are well-defined nanorods.

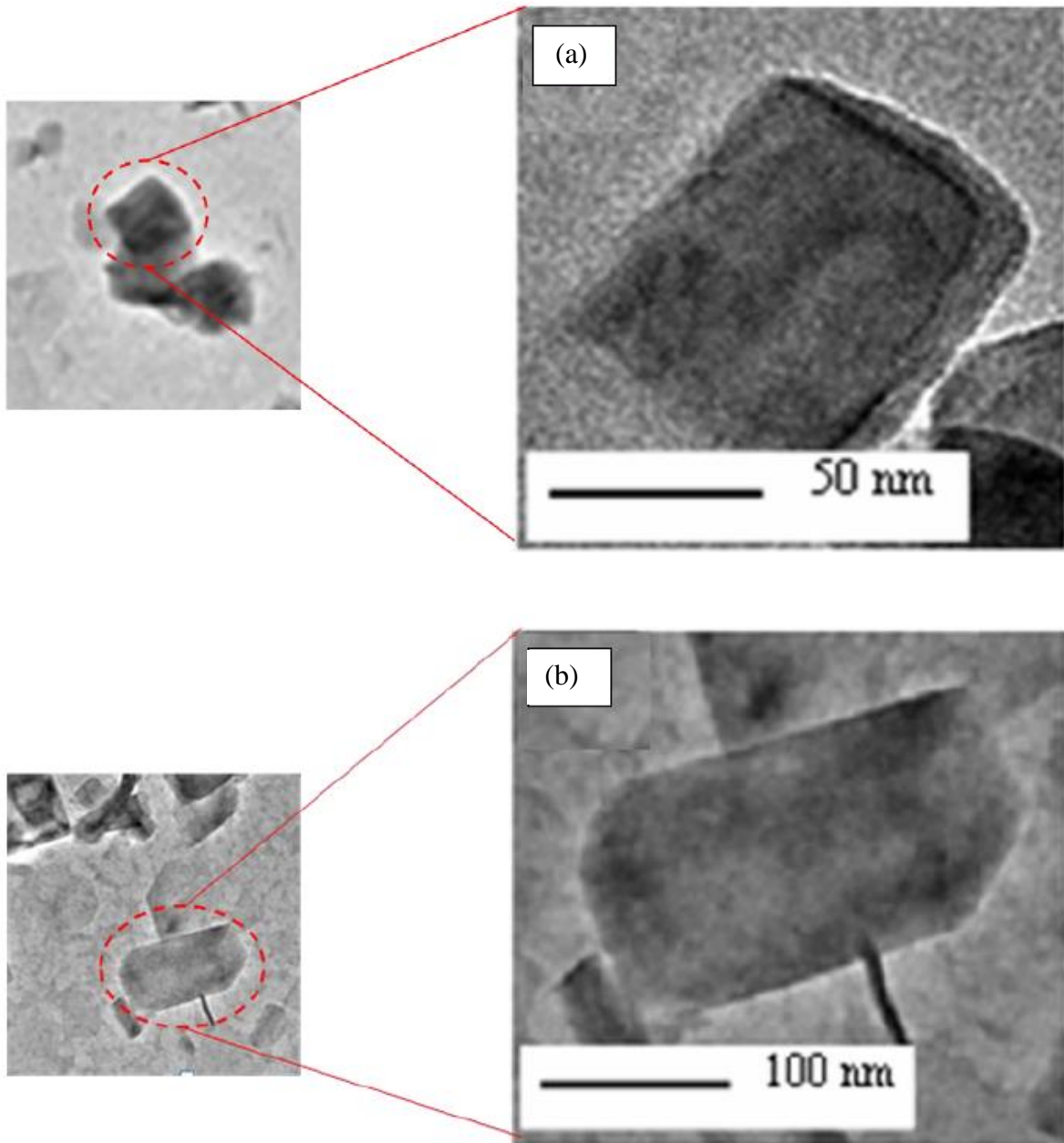


Figure 2-8: Magnified images of the nanoparticles sampled at $Z = 10$ mm (Desai, 2010).

In order to thoroughly investigate the geometry of the structures the TEM grid is rotated to give a magnified view of the captured nanomaterial (Figure 2-8). Examination of these images shows well faceted longitudinal particles with well-defined aspect ratios. Figure 2-8 (c) shows a nanorod with length ~100 nm and lateral dimension ~40 nm.

2.2.2 Nanoparticle Synthesis from 0.75 mm Diameter Molybdenum Probe

The 0.75 mm diameter probe is inserted into the flame at the same height of 13 mm from the fuel nozzle and the developed nanoparticles are collected thermophoretically for analysis.

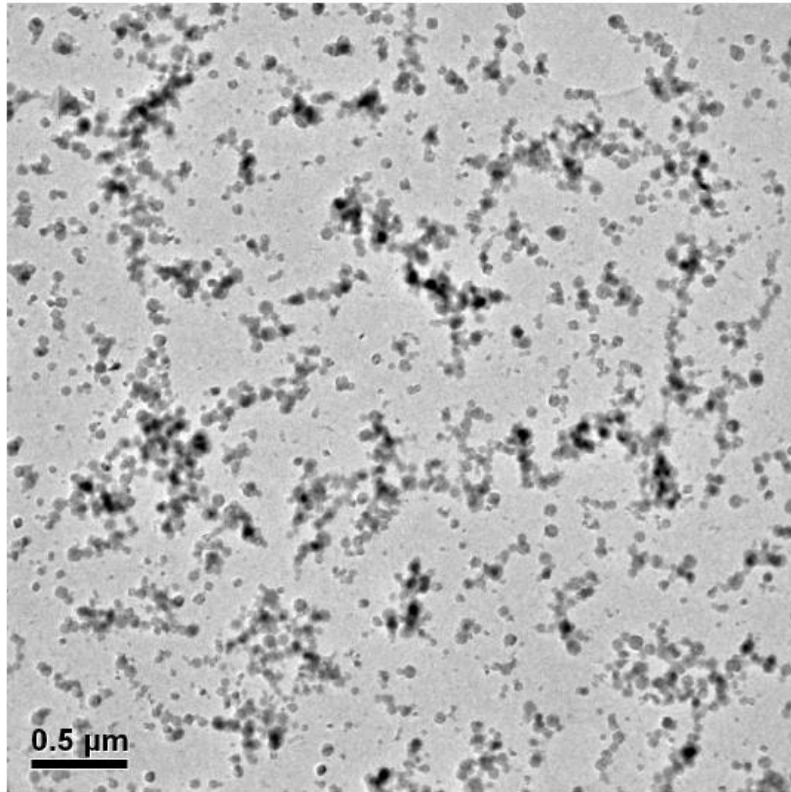


Figure 2-9: Low resolution TEM image of nanoparticles formed by 0.75 mm probe at $Z = 10$ mm (Desai, 2010)

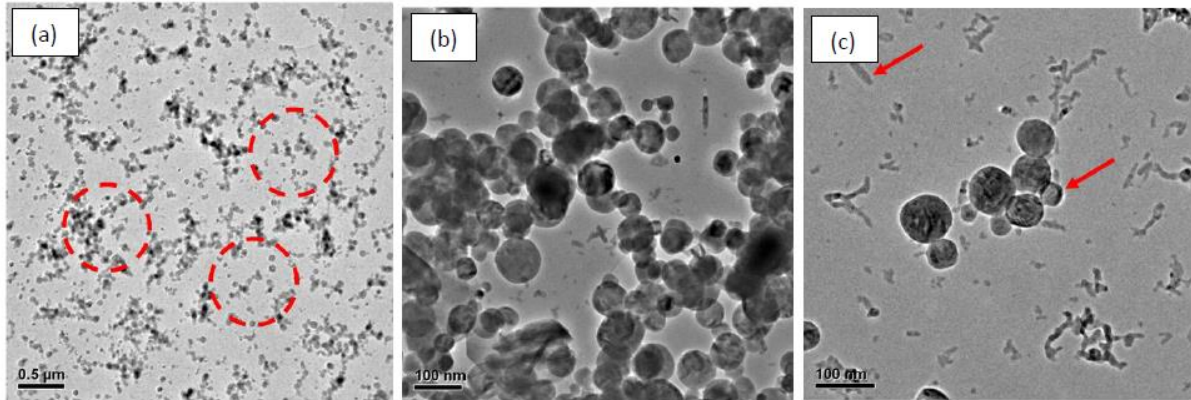


Figure 2-10: Magnified TEM images of nanoparticles formed by 0.75 mm probe (Desai, 2010)

Looking at Figure 2-9 it is evident that the number of particles formed are clearly much higher than the ones formed when the 1.00 mm diameter probe was used as the material source. But there is a marked difference in their morphologies. The particles collected in Figure 2-10 even at a distance of 10 mm all exhibit spherical geometries. There are no traces of any nanorods or polyhedral shaped nanoparticles. The largest particles are approximately 80 nm in diameter and the smallest are about 5 nm.

2.3 Conclusions of Experimental Results

Probes of different diameters (1.00 mm and 0.75 mm) were placed in the highly oxidative environment of the oxy-methane diffusion flame. The probes interact with the flame and material etching occurs. The strong chemical and temperature gradients provide ideal

conditions for the nanoparticles to grow in the flame volume. The variation in the probe diameter strongly affects the morphology of the resulting nanostructures. Experiments with 1.00 mm diameter probe yield well defined nanorods whereas the 0.75 mm diameter results in the synthesis of mainly spherical amorphous nanoparticles. For nanorods preferential material addition takes place in the longitudinal direction unlike the spherical nanoparticles which grow by random agglomeration.

Chapter 3

Brief Introduction to the Numerical Model

The mechanism of growth and morphology of nanoparticles is dictated by internal as well as external factors. It depends on the structure of the unit cell, defects in the crystal (internal factors), the growth conditions and the type of synthesis method employed (external factors). The interplay of these external and internal factors is imperative to comprehend the mechanism behind nanoparticle growth and predicting the texture and structure of the nanoparticles. During the growth of a nanoparticle various surface defects develop in the structure and along with impurity elements play an active role in determining the morphology of the particle. The process of understanding their role leads to the development of methods of controlling perfection and homogeneity of nanostructures according to their utility in the industry owing to their unique desirable qualities.

Nanoparticle formation begins only when a driving force perturbs the equilibrium of the system and a nucleus begins to grow. This growth can take place in any ambient condition (gas or liquid). In the growth process of a nanocrystal heat and mass transfer play active roles

but their relative contribution is determined by the type of growth mode and the ambient conditions.

As will be seen later, the interface of a nanoparticle can be classified into atomically rough and smooth surfaces. The two types of surfaces have different type of growth modes and eventually give rise to crystals having different morphologies. Nanoparticles formed under small driving force conditions will generally exhibit polyhedral forms as well as elongated structures like nanorods, whiskers, hollow tubes etc. Whether a nanoparticle is freely grown or bounded by a substrate also affects the shape.

Heat and mass transfer being an important part of the growth process exert varying levels of contribution depending on the ambient phase. For growth of particles in a dilute phase the mass transfer plays a greater role whereas for the growth in a condensed (liquid) phase heat transfer is of prime importance since the densities of the solid and melt phases don't differ a lot.

Finally, the entire process of nanoparticle growth is divided into three major steps –

- i. A driving force in the form of a difference in the supersaturation levels provides the initial push for the supersaturated phase to condense into an aggregate state.
- ii. Precursor atoms called *monomers* come together to form small clusters. Some of these clusters combine and grow larger than the critical size while the ones who are unable to overcome the critical size barrier wither away. This process is called *nucleation*.
- iii. The clusters that have grown larger than the critical size grow further in a desired fashion and go on to form nanoparticles of various morphologies.

3.1 Details of the Growth Model

The entire mathematical scheme for simulating the development of one-dimensional nanorod in the flame has been divided into two parts as shown in Figure 3-1 below

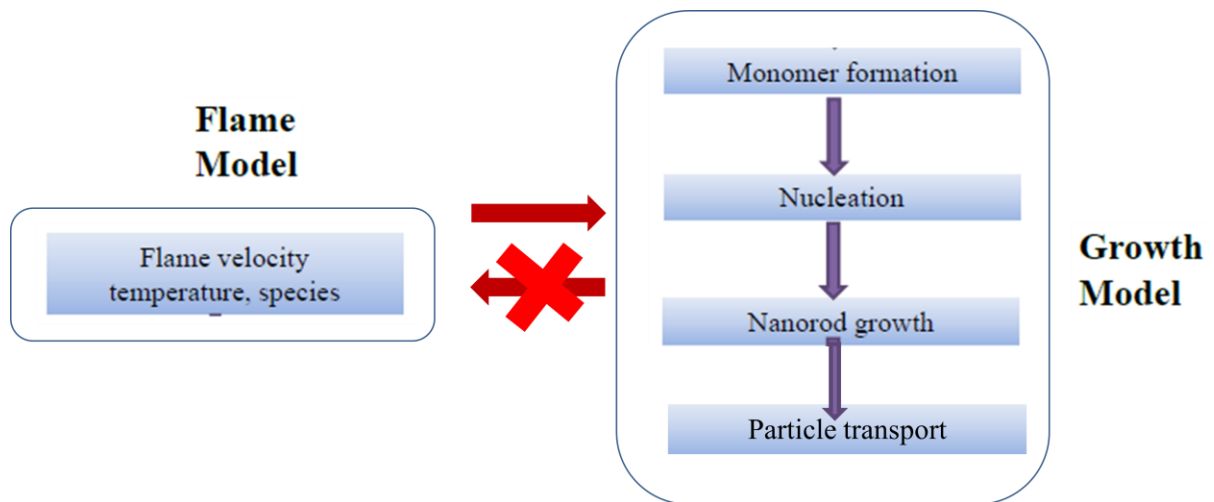


Figure 3-1: Subdivisions of the numerical model.

The Flame Model employs the open source software Cantera (Goodwin, 2009) to simulate the 1-D counter-flow diffusion flame. It solves for the species, mass, momentum and energy transport. The Growth Model is partitioned into *Monomer formation*, *Nucleation*, *Nanorod growth* and *Particle transport*. Each of these divisions handles a separate physical phenomenon as explained in the later sections of the literature. Both, the Flame Model and the Growth Model work in tandem to accurately simulate the nanoparticle synthesis. There is

however a one way coupling between the two sections. Information is passed from the Flame Model over to the Growth Model but no passage of information takes place from the Growth Model to the Flame Model. This has been done with the assumption that the volume of nanoparticles created is extremely minuscule in comparison to the flame and there is no change in the flow field due to the nanoparticles.

The Growth Model focuses on the development of a single nanorod and simulates its development through time in various conditions. Simulation of the entire group of nanoparticles is the content of study for Chapter 10 where the entire distribution of the nanorods produced in the flame has been studied.

In accordance with the experiments the numerical simulations have been carried out to understand the growth processes for two monomer sources –

- i. 0.75 mm diameter molybdenum probe
- ii. 1.00 mm diameter molybdenum probe

3.2 Assumptions

Nanorod formation is an extremely complicated process and entails several intricately related physical parameters. Being the first step towards the modeling of 1-D nanorods, this work necessitates the inclusion of certain assumptions. This chapter enumerates all the assumptions in this research.

- i. While calculating the temperature of the molybdenum probes the transfer of heat has been assumed to occur only through convection. The axial conduction has been neglected.
- ii. Upon oxidation the molybdenum probes form molybdenum dioxide monomers. Since the concentration of the monomers is considerably small they have been treated as an ideal gas and their concentration has been measured in terms of partial pressure.
- iii. The nucleation process has been modeled using the Classical Nucleation Theory. As a result the assumptions of CNT have also been imbibed into the simulation. Hence in spite of the fact that the formed nuclei are suspended in the flame environment, the properties of the molybdenum dioxide nuclei have been taken to be equal to that of the bulk material and the shapes of all the nuclei have been assumed to be spheres as is the case with liquid droplets.
- iv. All the nanorods have been assumed to have developed from equal sized critical nuclei.
- v. The growth of the nanorods only starts after the nucleation attains completion by reaching its maximum peak value.
- vi. The growth on the lateral surfaces of the nanorods proceeds by 2-D nucleation which give rise to single layers of atoms. Beyond a threshold this maturation should transcend into multi-layered growth. However, instead of simulating the multi-layered growth this layered growth has been considered to transform into rough growth as this type of growth ideally forms the upper limit for the surface processes.

vii. The distribution of various sizes of nanoparticles in a process develops due to differences in their growth times and growth rates. Although in the simulation all the particles start their growth simultaneously, the Quadrature Method of Moments has been used to introduce moment methods into nanorod development so they can be enhanced subsequently. To implement this study an initial distribution has been imposed by assuming a normal distribution of the particles with their mean size as the critical size of the nuclei and the standard deviation as the difference in the size of the nuclei at the beginning and at the end of nucleation.

Chapter 4

Flame Modeling

The Flame Gradient Method uses a one dimensional counter flow flame for the production of 1-D nanostructures. The fuel used is 96% methane and 4% acetylene along with the oxidizer which comprises of 50% oxygen and 50% nitrogen. The flame strain rate is 20 s^{-1} . The flame has been modeled using Cantera (Goodwin, 2009). The one dimensional code solves for the steady state solution for axisymmetric diffusion flame with opposing nozzles for fuel and oxidizer. The solution predicts species, temperature and velocity profiles in the flame.

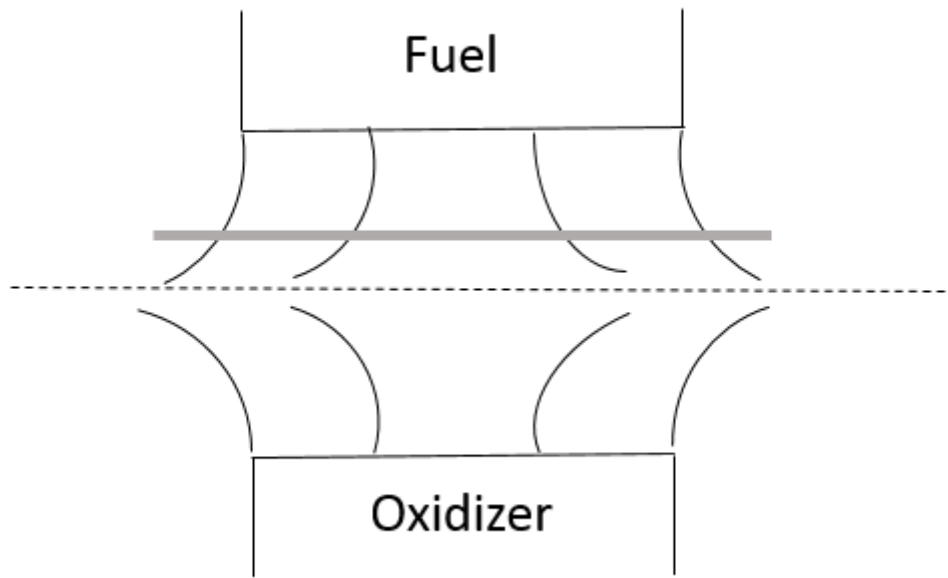


Figure 4-1: Schematic diagram of opposed flow diffusion flame.

4.1 Opposed Flow Flame Model

A counterflow flame configuration consists of two circular nozzles directed towards each other. The flow of oxidizer and fuel, coming from opposing directions, impinge and form a stationary flame. The location where the momentum of the two streams balance is known as the Stagnation Plane which can be controlled by altering the flow rate of either the fuel or the oxidizer mass flow rates. Since, as compared to the fuel more oxidizer is required by mass, the flame sits on the oxidizer side of the stagnation plane.

This type of counter flow flame structure is especially suited to studies in nanoparticle formation for two reasons –

- i. The flame is suspended freely in space, being completely free from burner heat losses and catalytic effects
- ii. It is assumed that the flow properties are functions of axial distance only and the radial velocities vary linearly, thus essentially reducing the two dimensional flow into one-dimensional

A detailed derivation of the governing equations is given by (Kee, et al., 1988) but a short summary of these equations is given below.

The mass conservation equation in cylindrical coordinates –

$$\frac{\partial}{\partial x}(\rho u) + \frac{1}{r} \frac{\partial}{\partial r}(\rho v r) = 0 \quad (4.1)$$

where u and v are the axial and radial velocity components and ρ is the density. Two dimensional flow has been reduced here to a one dimensional description by assuming the fluid properties to be dependent only on the axial direction and a linear variation of the radial properties with the radial distance. Equation (4.1) is satisfied by stream function

$$\psi(x, r) = r^2 U(x)$$

By defining

$$G(x) = -\frac{\rho v}{r} \text{ and } F(x) = \frac{\rho u}{2} \text{ equation (4.1) reduces to}$$

$$G(x) = \frac{dF(x)}{dx}$$

Since G and F are functions of x only so now the temperature, density, velocity and mass fractions all become functions of x only.

Introducing the above mentioned assumptions into the Navier Stokes equation it becomes clear that $1/r(\partial p / \partial r)$ and $(\partial p / \partial x)$ are functions of x alone. Since

$$\frac{\partial}{\partial x} \left(\frac{1}{r} \frac{\partial p}{\partial r} \right) = \frac{1}{r} \frac{\partial}{\partial r} \left(\frac{\partial p}{\partial x} \right) = 0$$

Therefore, for the radial momentum equation

$$H = \frac{1}{r} \frac{\partial p}{\partial r} = \text{constant}$$

$$H - 2 \frac{d}{dx} \left(\frac{FG}{\rho} \right) + \frac{3G^2}{\rho} + \frac{d}{dx} \left[\mu \frac{d}{dx} \left(\frac{G}{\rho} \right) \right] = 0 \quad (4.2)$$

Energy equation-

$$\rho u \frac{dT}{dx} - \frac{1}{C_p} \frac{d}{dx} \left(\lambda \frac{dT}{dx} \right) + \frac{\rho}{C_p} \sum_k C_{pk} Y_k V_k \frac{dT}{dx} + \frac{1}{C_p} \sum_k h_k \dot{\omega}_k = 0 \quad (4.3)$$

Species equation-

$$\rho u \frac{dY_k}{dx} + \frac{d}{dx} (\rho Y_k V_k) - \dot{\omega}_k W_k = 0 \quad (4.4)$$

The diffusion velocities can either be given in the multi-component form

$$V_k = \frac{1}{X_k \bar{W}} \sum_{j=1}^K W_j D_{kj} \frac{dX_j}{dx} - \frac{D_k^T}{\rho Y_k T} \frac{1}{dx} \frac{dT}{dx} \quad (4.5)$$

or in the mixture-averaged form

$$V_k = -\frac{1}{X} D^{km} \frac{dX_k}{dx} - \frac{D_k^T}{\rho Y_k T} \frac{1}{dx} \frac{dT}{dx} \quad (4.6)$$

where
$$D_{km} = \frac{\sum_{j \neq k}^K X_j M_j}{\bar{M} \sum_{j \neq k}^K X_j / D_{jk}}$$

Y_k is the mass fraction, C_p is the specific heat, h_k is the species molar enthalpy, W_k is the species molar mass and $\dot{\omega}_k$ is the chemical production rate, μ is the viscosity and λ is the conductivity.

D_{kj} , D_{km} and D_k^T are the binary diffusion, mixture averaged and thermal diffusion coefficient respectively.

Generally the temperature, mixture composition and the inlet velocity are specified at the inlet and the symmetry conditions are applied at the stagnation plane. Equations (4.1) to (4.6) form a boundary value problem.

4.2 Transport Properties

Solving the above equations requires the knowledge of transport properties like diffusion coefficients, viscosities, thermal conductivities and thermal diffusion coefficients (Kee, et al., 1986). The transport properties can be calculated either in mixture averaged or multicomponent fashion. Mixture averaged properties carry the advantage of simplicity and low computational expense but they also have the following disadvantages –

- i. Accuracy – The mixture averaged quantities are accurate only for simple cases as binary mixtures or when diffusion is taking place into a pure substance.

- ii. Mass conservation – Mixture averaged method does not necessarily ensure overall conservation of mass in the species conservation equation.

4.2.1 Mixture Averaged Properties

A short summary of the procedures followed by any standard combustion simulation code to calculate the mixture averaged transport properties is given here. For more detailed explanations and for procedures to calculate multicomponent transport properties refer (Kee, et al., 1986). To calculate the mixture averaged or multicomponent properties the transport properties of pure species must first be known. Polynomial fits are generated for the temperature dependent part of the pure species properties. This ensures the absence of any redundancy in calculating the collision integrals and other expensive operations. Their expressions have been summarized below (Hirschfelder, et al., 1954)

Viscosity –

$$\mu_k = \frac{5}{16} \frac{\sqrt{\pi W_k k_B T}}{\pi \sigma_k^2 \Omega} \quad (4.7)$$

where σ_k is the Lennard-Jones collision diameter, m_k is the molecular mass, k_B is the Boltzmann constant. The collision integral Ω depends on the reduced temperature and the reduced dipole moment.

Binary diffusion coefficients –

$$D_{jk} = \frac{3}{16} \frac{\sqrt{2\pi k_B^3 T^3 / m_{jk}}}{P \pi \sigma_{jk}^2 \Omega} \quad (4.8)$$

where m_{jk} is the reduced molecular mass and σ_{jk} is the reduced collision diameter. In considering the reduced quantities care should be taken whether the molecules are polar or non-polar.

Mixture averaged diffusion coefficient for species k –

$$D_{km} = \frac{\sum_{j \neq k}^K X_j M_j}{\bar{M} \sum_{j \neq k}^K X_j / D_{jk}} \quad (4.9)$$

Mixture averaged viscosity –

$$\eta = \frac{\sum_{k=1}^K X_k \eta_k}{\sum_{j=1}^K X_j \Phi_{kj}} \quad (4.10)$$

$$\text{where } \Phi_{kj} = \frac{1}{\sqrt{8}} \left(1 + \frac{M_k}{M_j} \right)^{-\frac{1}{2}} \left(1 + \left(\frac{\eta_k}{\eta_j} \right)^{\frac{1}{2}} \left(\frac{M_j}{M_k} \right)^{\frac{1}{4}} \right)^2$$

Mixture averaged thermal conductivity –

$$\lambda = \frac{1}{2} \left(\sum_{k=1}^K X_k \lambda_k + \frac{1}{\sum_{k=1}^K X_k / \lambda_k} \right) \quad (4.11)$$

here λ_k is the species specific thermal conductivity

4.3 Solution Procedure

The flow equations contain convective and diffusive terms. The discretization technique followed is a non-uniform grid where upwind differencing is used for convective terms and central differencing for diffusive terms. The upwind scheme ensures better convergence and has a first order approximation whereas the central differencing gives a second-order error approximation.

The initial grid can be defined by the user or it can be generated automatically with the initial number of grid points being chosen by the user. The above equations, applied at each point of the grid form two point boundary value problems. TWOPNT (Grcar, 1992) solver program is used to solve these steady state system of equations.

4.4 GRI mechanism

GRI-Mech 3.0 (Smith, et al.) provides all the relevant information for describing the combustion of methane and natural gas including NO formation and reburn chemistry. It involves 325 elementary chemical reactions of 53 species and has been validated for all the major steps in the combustion process deriving from the knowledge of reaction rate theory. The mechanism has been optimized for a temperature range of 1000 K to 2500 K, pressures of 10 Torr to 10 atm and equivalence ratios of 0.1 to 5 for premixed systems. Certain modifications have been made to it from its predecessor and the additions include propane and C₂ oxidation products and new formaldehyde and NO formation and reburn targets.

However, it does not incorporate certain aspects of methane combustion like soot formation and the chemistry behind selective non-catalytic reduction of NO. In spite of its lack of optimization for ethane, propane, methanol, ethylene and acetylene it has been incredibly successful as a combustion mechanism. GRI mechanism was originally developed for methane combustion but its applicability for acetylene has been established by comparison with the Warnatz mechanism (Movileanu, et al., 2012).

4.5 Results of the Flame Model

Counter-flow diffusion flames possess large gradients of temperature and chemical species concentrations. These gradients constitute the prime advantage of the Flame Gradient Method over other synthesis techniques to study the formation mechanism of nanoparticles. Depending on the required material and the characteristics of the nanoparticle product various zones of the counter-flow flame can be utilized. Figure 4-2 shows the chemical species profiles in the opposed flow oxy-methane flame. The flow equations have been solved using Cantera (Goodwin, 2009). Fuel used in these simulations is the same as the one used in the experiments (96% CH₄ + 4% C₂H₂) and the oxidizer used is also same as the one used in the experiments (50% O₂ + 50% N₂). The distance between the nozzles is 25.4 mm and the strain rate is 20 s⁻¹. The plot shows the fuel nozzle on the left side and the oxidizer nozzle on the right side with all the distances being measured from the fuel inlet. Methane and oxygen are at their highest concentrations at their nozzle inlets respectively and decrease as they approach the flame. This distribution divides the flame into two zones –

- i. oxygen rich zone
- ii. carbon rich zone

For producing metal oxide nanoparticles the raw material is introduced into the oxygen rich zone which instantly oxidizes the metal in the hot environment to form metal oxide precursors. Conversely, for producing carbon nanorods the raw material is placed in the carbon rich zone of the flame. Acetylene concentrations also follow similar trends as the methane concentration. Addition of acetylene has a marked effect on the temperature of the flame. A minute quantity of 4% of acetylene causes the temperature to rise by about 40°C which provides a conducive atmosphere for the molybdenum oxide nanorods to grow. Increase in oxygen content also increases the temperature but most of all it increases the thickness of the blue zone in the flame and the ideal thickness for molybdenum oxide nanorods is obtained at 50% O₂ and 50% N₂ composition.

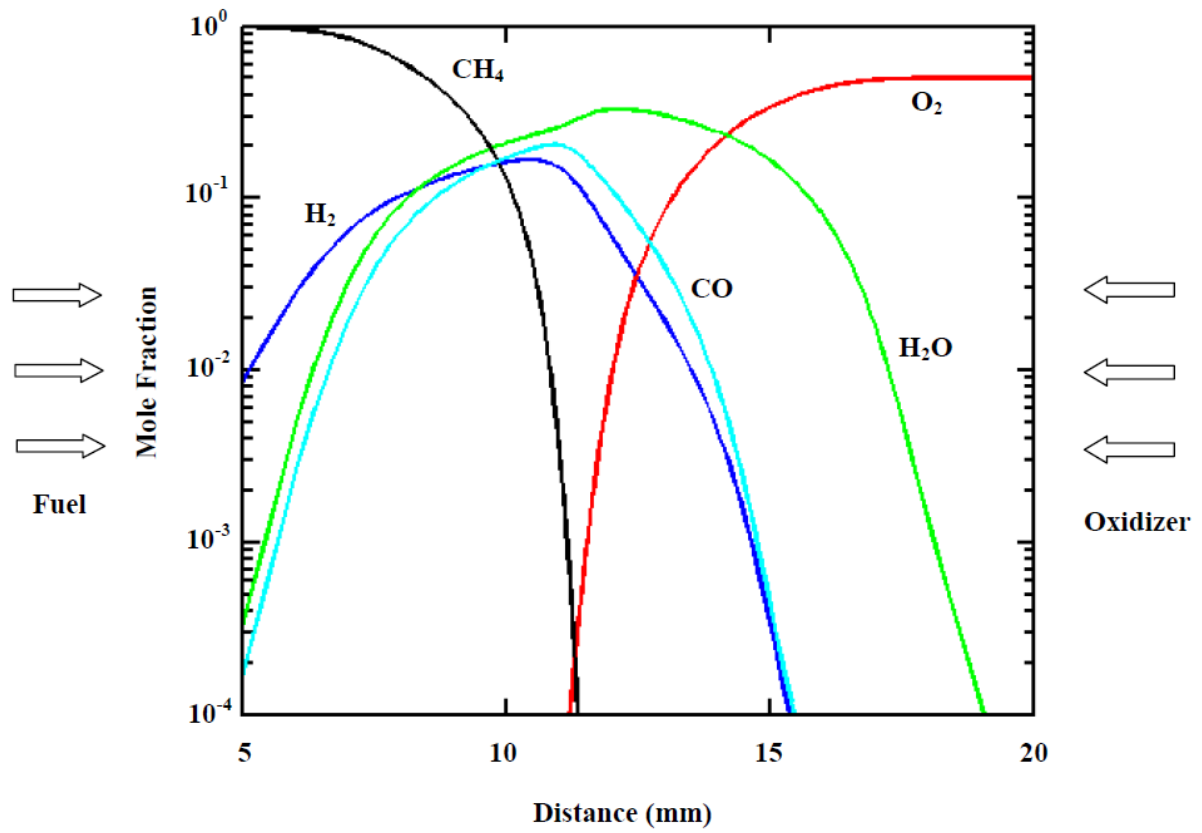


Figure 4-2: Chemical species concentration profiles for counter-flow oxy-methane flame.

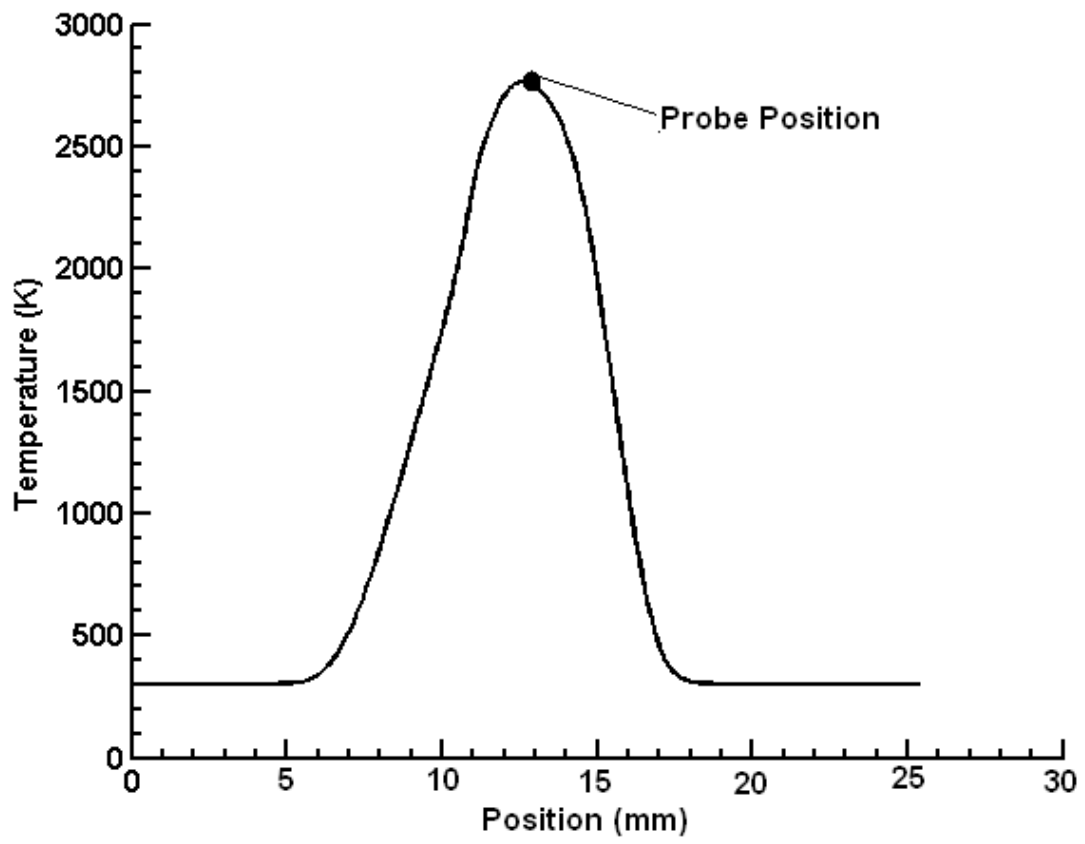


Figure 4-3: Temperature of the flame.

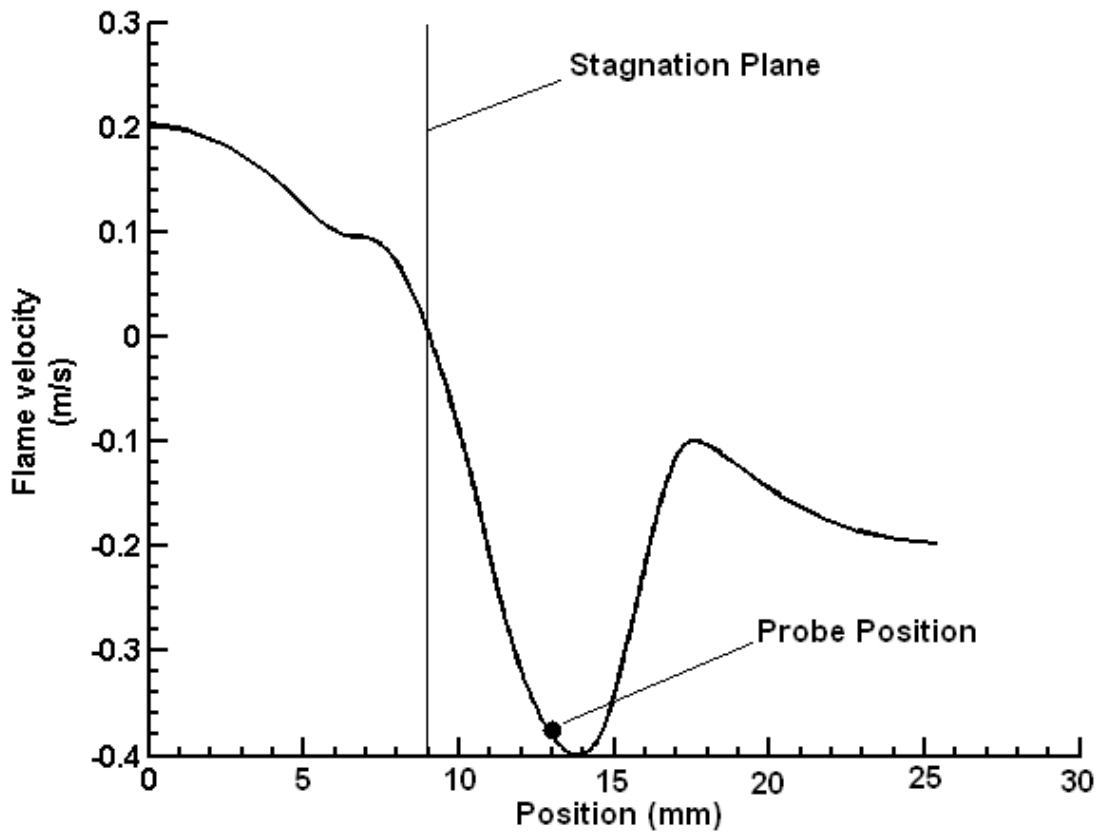


Figure 4-4: Gas velocity as a function of axial position.

Figure 4-3 and Figure 4-4 give the details of the temperature and the gas velocity. The maximum temperature of 2780°C results near the 13 mm mark from the fuel nozzle. The gas velocity is also plotted as a function of distance. Negative values of velocity signify the direction of gases to be from oxidizer to the fuel side and from fuel to the oxidizer side in case of positive values. A stagnation plane is formed in the region where the flow velocities from both the nozzles cancel each other to give a zero velocity. This position lies at 9 mm

from the fuel nozzle. The inlet gas velocities have been calculated from the strain rate equation.

$$S.R. = \frac{2U}{L}$$

where U is the inlet gas velocity and L is the distance between the nozzles.

Chapter 5

Monomer Formation

Monomers are the basic building units of complex molecules and structures. They bind with each other chemically to give rise to larger crystal shapes. In the case of molybdenum oxide nanorods the monomers are single molecules of MoO_2 which undergo different attachment patterns to form different shapes under varying conditions of supersaturation ratio.

In a nutshell the mechanism of monomer formation is as follows. When the probe is introduced into the oxygen rich zone of the flame it gets oxidized forming MoO_3 . MoO_3 being extremely volatile starts to move up with the flame and as it approaches the fuel nozzle the reducing atmosphere converts the MoO_3 to MoO_2 , forming the monomers. To completely comprehend the monomer formation and its implications on the growth of nanostructures a monomer formation model has been developed which incorporates a molybdenum oxidation mechanism. The information on amount of molybdenum oxidized also provides the knowledge of amount of MoO_2 formed from MoO_3 thus giving the concentration of monomers in the flame volume.

5.1 Molybdenum Oxidation

Commercial interest in molybdenum is particularly high due to its ability to withstand high temperatures. It has a melting point of above 2000 K hence making it ideal for applications in furnaces and high speed, high temperature flight. It also possesses considerable strength at high temperatures as compared to other common metals. However, molybdenum is highly susceptible to oxidation and the rate of oxidation continues to increase with temperature until the metal loses all its use. This severely reduces the lifespan of the metal component and restricts its functionality. The oxidation behavior of molybdenum has been studied (Douglass, 1970) (Kubaschewski, et al., 1967) and in oxidizing atmosphere molybdenum starts to sublime above 500°C. The reaction of molybdenum with oxygen is complex and from room temperature to 1700°C involves a number of different oxidation processes (Saburi, et al., 2001).

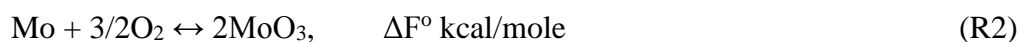
A number of studies have been dedicated to understand the complicated phenomena of molybdenum oxidation since it has different oxidation regimes under different temperature conditions. Under the temperature limit of 400°C adherent oxide layers were observed on the surface of the metal (Gorbounova, et al., 1956). The oxidation rate data was fitted under a parabolic curve and energy of activation of 36 kcal/mole was determined. Considerable deviations to this parabolic law were observed over 400°C with volatilization occurring at 475°C under vacuum conditions. When the pressure was increased to 1 atm the vaporization temperature changed to 650°C. (Simnad, et al., 1955) observed the behavior between 500°C and 1000°C and were able to fit the data on a parabolic law at 500°C and by a linear rate

above 500°C. However, catastrophic oxidation set in at 725°C (Lustman, 1950). (Peterson, et al., 1954) investigated the oxidation of molybdenum at higher temperatures as a function of temperature and pressure and found that it followed a linear rate law at all temperatures and pressures thus indicating that a non-protective oxide was formed.

Another interesting aspect to the oxidation process is the transport phenomena. To include the effects of transport (Bartlett, et al., 1958) conducted experimental studies with the reaction system in air between 760°C and 1204°C using a flow system. The flow rate was found to affect the rate of oxidation which slowly increased with the temperature as well as the flow rate.

5.2 Oxidation Regimes of Molybdenum

(Gulbransen, et al., 1963) conducted a detailed study into the oxidation regimes of molybdenum, its chemical mechanism and the rate controlling factors. Since under certain conditions molybdenum forms both oxide scale and volatile molybdenum trioxide therefore a) it was essential to determine the nature of the reaction b) the kinetics of oxidation was studied over a wide temperature and pressure range to study the primary chemical reaction c) it was essential to ascertain the transition zone between chemical and transport controlled oxidation. They considered the following five reactions with the listed standard free energies of reaction and equilibrium pressures–



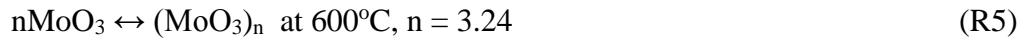


Table 5-1: Thermochemical data for Oxides of Molybdenum

<i>Temp, K</i>	<i>R1</i> $\Delta F^\circ, \text{ kcal}$	<i>R2</i> $\Delta F^\circ, \text{ kcal}$	<i>R3</i> $P_{\text{O}_2}, \text{ atm}$	<i>R4</i> $\Delta F^\circ, \text{ kcal}$
298	- 127.45	-159.7	5.38×10^{-48}	+ 63.0
400	- 122.9	-153.45	4.44×10^{-34}	+ 61.85
600	- 114.1	- 141.35	1.42×10^{-20}	+ 59.6
800	- 105.55	- 129.6	7.23×10^{-14}	+ 57.45
1000	- 97.15	- 118.1	7.10×10^{-10}	+ 55.3
1200	- 88.95	- 112.7	9.51×10^{-8}	+ 50.4
1400	- 80.95	- 108.25	1.56×10^{-6}	+ 43.7
1600	- 73.05	- 99.55	----	----
1800	- 65.35	----	----	----
2000	- 58.0	----	----	----

They observed that pressure had little effect on the reaction below 800°C but beyond that limit the effect of pressure on the reaction rate was large and the rate followed the 1.5 power of the pressure. Oxidation studies too showed similar phenomena. The percentage of oxygen forming oxide scales reduces with temperature. At 700°C only 30% of the oxygen is employed in the formation of scales. Molybdenum metal is oxidized forming three layers: the outermost MoO₃, the innermost MoO₂ and the intermediate layer which can be expressed by Mo_xO_{3x-1} (Mo₄O₁₁, Mo₈O₂₃, Mo₉O₂₆). At 800°C however, all of the oxygen used forms volatile molybdenum trioxide at atmospheric pressure. They concluded that between 600°C and 800°C both solid oxide and volatile oxide occur. But above 800°C only volatile molybdenum trioxide is formed. The various oxidation regimes of molybdenum can be summarized as follows –

Table 5-2: Classification scheme; oxidation of molybdenum (Gulbransen et. al., 1963)

Class	Reaction Condition	Oxidation Process	Rate controlling
1	Below 450°C	Adherent oxide films or scales form	Diffusion of metal or oxygen through oxide
2	500° – 700°C	Oxide scales form also oxide volatizes	Oxide scales not protective. Chemical type processes on metal surface
3	801°C to transition temperature	Liquid oxide can form, volatizes as soon as oxide forms	Chemical processes on metal surface

Table 5-2 Continued

4	Above transition temperature	Oxide volatilizes as fast as it forms	Transport of oxygen to metal interface. Turbulence in gas is important
---	------------------------------	---------------------------------------	------------------------------------------------------------------------

In the Flame Gradient Method the temperature of molybdenum oxidation is always greater than the *transition temperature* hence the mode of oxidation always has transport of oxygen as the critical factor.

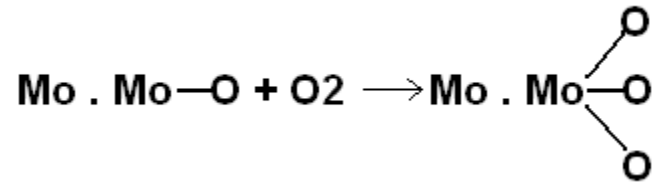
5.3 Mechanism of Molybdenum Oxidation

The entire process of oxidation of molybdenum comprises of five major steps (Jones, et al., 1958)–

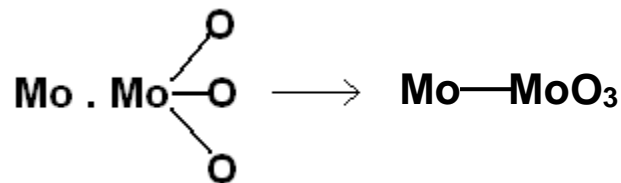
- i. transport of oxygen to the surface
- ii. chemisorptions of the oxygen
- iii. chemical reaction at the surface
- iv. desorption
- v. transport of reaction products

The slowest of these is the rate controlling step. Processes ii, iii and iv are chemical processes and are marked by a large activation energy whereas processes i and v are transport processes and depend on mass transfer parameters.

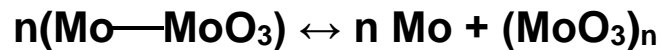
Primarily a monolayer of oxygen is adsorbed with a much lower activation energy followed by mobile adsorption of O₂ on this monolayer (Gulbransen, et al., 1963)



The resulting complex undergoes a chemical reaction



Finally the desorption takes place resulting in gaseous molybdenum trioxide



5.4 Rate Equation for Molybdenum Oxidation

Metals are easily prone to oxidation at high temperatures and invariably form oxides which are solid at temperatures below the melting point of the metal. These oxides later form a protective layer around the metal which inhibits any direct contact with oxygen. For any further oxidation to take place the oxygen has to diffuse through the oxide coatings. This diffusion process is usually slow and hence forms the sole rate determining step in the entire process.

Molybdenum on the other hand forms oxides whose melting and boiling points lie below the melting point of the metal. The most stable of its oxides is molybdenum trioxide whose melting point is 1428 K which is much lower than the melting point of molybdenum which is 2890 K. Under appropriate conditions and at sufficiently high temperature molybdenum trioxide completely volatilizes as soon as it is formed. The immediate vaporization of molybdenum trioxide from the metal leaves the surface bare and completely susceptible to vigorous attack by oxygen atoms. Since there is no need for diffusion the concentration of oxygen around the metal becomes the rate determining factor now. However as the reaction progresses the oxygen layer gets depleted and now the transport of oxygen becomes crucial. The rate of transport of oxygen to the metal surface depends on two factors –

- i) diffusivity of oxygen in the ambient gas mixture
- ii) the velocity of flow of gas over the metal.

Attempts to determine the activation energy of the oxidation of molybdenum yield unreasonable results with discontinuities and anomalies. This is because the Arrhenius equation is not entirely valid for reactions which have gaseous diffusion as their rate determining step (Semmel, 1959). That is why the analysis used in this study incorporates chemical as well as mass transfer effects.

In the flame gradient method the molybdenum wire is placed in the oxidizing atmosphere of the flame. The gases flow past the cylindrical wire oxidizing the molybdenum to molybdenum trioxide which is volatile at these temperatures. The oxidation rate at a point on the surface of the metal wire (expressed as oxygen consumed) can be written using kinetic theory of gases (Laidler, et al., 1940) as

$$k = \frac{Y_{O_2,w} U \rho}{4} \exp\left(-\frac{E_a}{RT_p}\right) \quad (5.1)$$

$Y_{O_2,w}$ and ρ are the mass fraction of oxygen near the metal surface and the density of gas respectively. U is the average molecular speed of oxygen given by

$$U = \sqrt{\frac{8RT}{\pi W_{O_2}}} \quad (5.2)$$

For steady state conditions the rate of consumption of oxygen should be equal to its mass transport. Thus

$$k = h_m (Y_{O_2} - Y_{O_2,w}) \quad (5.3)$$

h_m being the mass transfer coefficient. From equations (5.1) and (5.3) $Y_{O_2,w}$ is unknown and hence can be eliminated. This results in

$$k = \frac{Y_{O_2} h_m \frac{U}{4} \exp\left(-\frac{E_a}{RT_p}\right)}{\frac{U}{4} \exp\left(-\frac{E_a}{RT_p}\right) + \frac{h_m}{\rho}} \quad (5.4)$$

Equation (5.4) contains in itself the effects of chemical as well as transport factors and changes its form depending on the factor that dominates in the given circumstances (Schryer, et al., 1961). There is however an assumption to be made here that the density and the mean molecular weight of the gas stays the same. Equation (5.4) has two unknowns- activation energy E_a and mass transfer coefficient h_m .

Values of activation energy for oxidation of thin flat plates of molybdenum have been numerically calculated and experimentally verified by (Schryer, et al., 1966). The overall

E_a mean value calculated was 8.51×10^7 J/(kg mole) which agrees within 3% obtained by (Gulbransen, et al., 1963) using experimental methods from an Arrhenius plot. Generally this form of computation of activation energy from experimental means is unreliable owing to the role played by gas transport for a volatile oxide. However, since the experiments were conducted under the chemically controlled regime where mass transfer effects don't play a role, makes this measurement rather authentic.

Mass transfer coefficients are not readily available but extensive information is known about heat transfer coefficients in different geometries and flow configurations. Certain analogies can be developed between heat and mass transfer which are justified and those can be used to get information about the mass transfer coefficients. A reasonable approximation is to assume Lewis number as unity ($Le = 1$). Now the mass transfer coefficient can be found by equating the Prandtl and Schmidt numbers and using the Nusselt number correlation for flow across a cylinder (Cengel, 2003).

$$Nu_{cyl} = 0.3 + \frac{0.62 Re^{1/2} Pr^{1/3}}{\left[1 + \left(\frac{0.4}{Pr}\right)^{2/3}\right]^{1/4}} \left[1 + \left(\frac{Re}{282000}\right)^{5/8}\right]^{4/5} \quad (5.5)$$

$$h_m = \frac{Nu_{cyl}}{d} \rho D_{O_2} \quad (5.6)$$

d is the diameter of the molybdenum wire and D_{O_2} is the diffusivity of oxygen in the gas.

To calculate the values of Re and Pr, the average viscosity and thermal conductivity of the flow were calculated using Cantera subroutines *viscosity*() and *thermalconductivity*(). They were 1.94×10^{-5} kg/(m s) and 0.0265 W/(m K) respectively. The value for D_{O_2} was computed

using the Cantera subroutine *mixDiffusioncoeffs*(). The mass diffusivity and thermal diffusivity data for various species has been reported in *Appendix E* and *F* respectively.

A detailed derivation of these expressions is given in Appendix A

5.5 Calculation of Molybdenum Probe Temperature and Molybdenum Dioxide Concentration

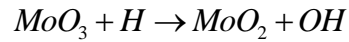
The oxidation process also plays a very important role in the heat balance of the metal probe. This wire when inserted into the flame gets heated by convection and cooled by radiation. The axial conduction losses are neglected. Further the enthalpies of molybdenum oxidation and evaporation of the formed molybdenum trioxide contribute to heat loss. Then the steady state heat balance can be written as-

$$h_{cyl}A_p(T - T_p) - \sigma \varepsilon A_p T_p^4 + E_{reac} \frac{d}{dt}[MoO_3] - E_{vap} \frac{d}{dt}[MoO_3] = 0 \quad (5.7)$$

h_{cyl} is the heat transfer coefficient, E_{reac} and E_{vap} are the enthalpies of oxidation and vaporization on per unit mass basis (kJ/kg) and A_p and T_p are the surface area and temperature of the molybdenum probe. Since it takes 1.5 moles of oxygen to produce 1 mole of molybdenum trioxide therefore $\frac{d}{dt}[MoO_3] = 0.1482 \cdot kA_p$ on a per unit mass basis. The value of emissivity for the surface has been taken as 0.5. Iterating through equation (5.7) gives us the correct probe temperature. Determination and verification of the probe

temperature also acts as a sanity check for the values of rate of oxidation obtained from equation (5.4).

Molybdenum dioxide is assumed to be primarily formed by the reaction



It is assumed that the rate of formation of molybdenum dioxide is equal to that of molybdenum trioxide and the concentration of molybdenum dioxide monomers has been converted into partial pressure using the mass conservation equation.

5.6 Verification of the Molybdenum Oxidation Kinetic Model

Modeling the oxidation rates of a volatile oxide is an extremely challenging task. The chemical as well transport phenomena working in tandem make things quite complicated. To verify the veracity of the molybdenum oxidation model equation (5.7) was solved and compared to the results obtained from experiments. The temperature of the molybdenum probes was measured during the experiments. For the numerical simulations the temperature of the probes is obtained by solving equation (5.7) through thermal balance.

Table 5-3: Comparison of calculated temperature of molybdenum probe to the experimental temperature

<i>Probe Diameter</i>	<i>Rate of Oxidation</i>	<i>Experimental Temperature</i>	<i>Calculated Temperature</i>
1.00 mm	2.06×10^{-7} kg/s	1100 °C	1187°C
0.75 mm	2.26×10^{-7} kg/s	1300 °C	1402°C

The calculated temperatures for the two probe diameters show slight variations from the measured values.

However, the increasing trend of the calculated probe temperature with decrease in probe diameter is encouraging and as a first cut approach these values of the rate of oxidation have been utilized in the remaining modules of the numerical model.

Chapter 6

Nucleation

Product and process design are highly affected by crystal size and shape. For this purpose it is essential to improve the methodologies of prediction and control of crystal shape and structure. Nucleation being a key player in the growth and polymorph selection has attracted a considerable amount of interest. Through the past couple of decades various models have been proposed for providing satisfactory explanations to the nucleation phenomenon but there have been many hurdles in an effort to bridge the gap between theoretical and experimental understanding. These can be grouped into three categories (Yau, et al., 2001):

- i. the constituent atoms or molecules are so small that even if the clusters are detected their structures cannot be discerned by most microscopic techniques
- ii. the critical clusters exist for extremely short times after which they either grow to macroscopic crystals or decay
- iii. the critical clusters are relatively small, and due to Brownian diffusion, they freely move throughout the available volume of the mother phase

A prominent feature of nucleation is the metastability of the old phase, the transition requires the passage over a free energy barrier (Vekilov, 2004).

Nucleation can essentially be of two types –

- i. Heterogeneous
- ii. Homogeneous

Homogeneous nucleation occurs all through the mother phase as a result of random perturbation in the density whereas heterogeneous nucleation occurs at the interfaces having been incited by the surface defects. Both these events are primarily driven by a difference in the pressures of the particle and the surrounding phase called supersaturation. Further, the nanomorphology of the particles is affected by forces which are thermodynamic or kinetic in nature such as temperature, chemical environment and electric fields. Grasping the contribution of each of these is the key to understanding nucleation and all of the theories have been designed with this purpose in mind.

Phase transformations are always driven by the differences in initial and final free energies of the configurations. These first order phase transitions result in nucleation of a new phase due to fluctuations. A rigorous thermodynamic definition of a nucleus and an explanation of the accompanying processes was initially provided by the Classical Nucleation Theory (CNT). This theory was able to satisfactorily demonstrate an agreement with the experiments for quite some time with a variety of systems. However, in the successive years as the understanding of nucleation increased questions began to be raised on the validity of CNT. This resulted in a series of modifications and corrections to the original theory.

This chapter will discuss the implementation of CNT to this research and limits to its applicability along with other proposed modifications.

6.1 Classical Nucleation Theory (CNT)

CNT was formulated to describe simple nucleation processes like condensation of pure vapor to liquid. Gibbs has been credited with the postulation of laws of phase transformation (Gibbs, 1928). Volmer, Becker and Doring (Volmer, et al., 1926) and Zeldovich later extended Gibbs' work to give a structure to CNT. The theory takes a macroscopic approach employing concepts of thermodynamics and statistical physics to account for the different aspects of phase change. The free energy involved in the formation of a new phase and a surface is the main parameter of CNT (Anisimov, 2003).

In the creation of a nucleus the energy decreases due to the transition to a lower energy phase but at the same time the energy also increases due to the formation of an interface between the two phases. This change in free energy can be written as –

$$\Delta G = n(\mu_l - \mu_v) + 4\pi r^2 \sigma \quad (6.1)$$

Here n is the number of molecules in the nucleus, μ_l and μ_v are the chemical potentials of molecules in liquid and vapor phases, r is the radius of the nucleus and σ is the surface energy. Equation (6.1) can also be written as

$$\Delta G = -\frac{4}{3}\pi \frac{r^3}{v_l} k_B T \ln S + 4\pi r^2 \sigma \quad (6.2)$$

where S is the supersaturation ratio and v_l is the volume of monomer molecule in liquid state.

As can be seen that both the terms depend on the radius but the first term is negative and the second one is positive. Therefore there must exist a critical radius ' r_c ' where the free energy is zero. If the nucleus is larger than this critical size it has a higher probability to grow than

decay and if the nucleus is smaller than this critical size then it has a higher probability to decay (Lovette, et al., 2008). This radius is found to be

$$r_c = \frac{2\sigma v_l}{k_B T \ln S} \quad (6.3)$$

In CNT the nucleus is assumed as a sphere with properties exactly same as the bulk liquid (Christian, 2002)

Herein lays the problem. The nucleus having a diameter of a couple of molecules is in a transition zone with properties in between the bulk and the vapor phase. Also the surface energy will vary with the position chosen as the radius of curvature is of the order of the transition region.

As the understanding about nucleation grew serious doubts began to be cast on CNT including the ones mentioned above. Various corrections were made by many contributors in order to achieve adequate accuracy in the results. Many of these problems and their solutions have been discussed later.

Following the CNT we have

$$J = \frac{\beta}{\sum_{i=1}^{\infty} [s_i n_i]^{-1}} \quad (6.4)$$

where $\beta = \frac{\alpha P}{\sqrt{2\pi m k T}}$, $s_i = (36\pi v^2)^{1/3} i^{2/3}$

Here J is the number of nuclei formed per unit time per unit volume, β is the rate of impingement of atoms from the vapor and s_i is the surface area of the nuclei containing I

molecules; P is the pressure, T is the temperature, m is the mass per molecule and α is the mass accommodation coefficient (Katz, 1970).

The distribution of nuclei in the vapor is given by

$$n_i = N_{cl} \exp\left[i \ln S - \gamma i^{2/3}\right] \quad (6.5)$$

Where $\gamma = \left(36\pi v^2\right)^{1/3} \frac{\sigma}{k_B T}$

$S = P/P_\infty$ is the supersaturation, N_{cl} is the total number of clusters of all sizes per unit volume.

In the Volmer theory (Volmer, et al., 1926) the distribution of n_i falls abruptly to zero at n_c (critical). Later Becker and Doring modified this distribution in quasi-steady state to decrease slowly. Owing to this gradual distribution the summation in equation (6.4) can be converted to an integration (Katz, 1970)

$$J = \frac{\beta}{\int_1^\infty [s(x)n(x)]^{-1} dx} \quad (6.6)$$

Now substituting equation (6.5) and the definitions of β and s we have the nucleation rate as-

$$J = \left(\frac{2\sigma}{\pi m}\right)^{1/2} \frac{\alpha N_{cl} P v}{k_B T} \left[1 + \frac{9\bar{x}^{4/3}}{2\gamma} g''(\bar{x})\right]^{1/2} \exp\left[g(\bar{x}) - \bar{x}g'(\bar{x}) - \frac{\gamma}{3}\bar{x}^{2/3}\right] \quad (6.7)$$

\bar{x} is the value of x at minimum $n(x)$ i.e. $n'(\bar{x})=0$

The terms $g(x)$, $g'(x)$ and $g''(x)$ are size-dependent correction factors which have been introduced by various authors. For CNT –

$$g_{CNT} = 0; g'_{CNT} = 0; g''_{CNT} = 0$$

Therefore equation (6.7) is a universal equation of CNT and its modifications which have been discussed later. Figure 6-1 shows the different distributions of nuclei in Volmer and Becker-Doring theory.

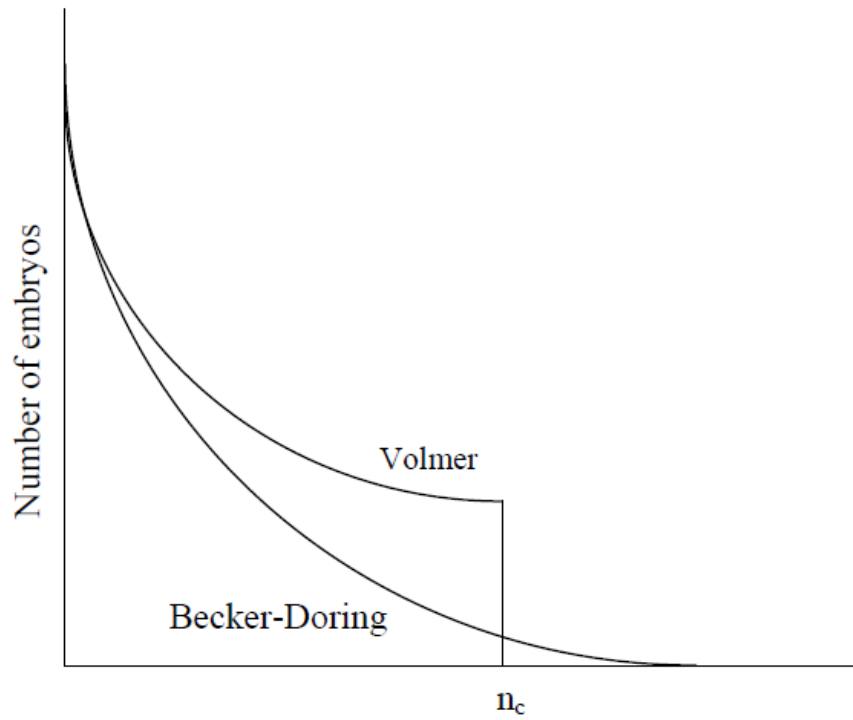


Figure 6-1: Distribution functions of embryos of different sizes according to Volmer and Becker-Doring theories of nucleation (Christian, 2002).

Although equation (6.7) has been written in a form to encompass CNT and its correction factors introduced later on, the general format of an expression for rate of nucleation includes

a factor proportional to the frequency of collision of atoms times the $\exp\left(\frac{-\Delta G_c}{k_B T}\right)$

Obviously the free energy change ΔG_c has been realized through equation (6.5).

CNT includes certain unjustified assumptions and mathematical approximations, some of which are discussed below.

6.1.1 Assumptions in CNT

- i. Small clusters are assumed as small portions of macroscopic phase and their properties are described by macroscopic thermodynamic properties.
- ii. Since the clusters are a couple of atomic diameters across therefore the surface energy is not isotropic.
- iii. The density of the clusters should conform with a transition zone density.

Next we discuss the corrections made to CNT to deal with these inconsistencies.

6.2 Lothe and Pound

The exact determination of ΔG is a matter of disagreement among different researchers. Lothe and Pound (LP) (Lothe, et al., 1962) argued that the free energy of a liquid nuclei in vapor would be considerably different than the free energy of the nuclei in its bulk phase

primarily because of the presence of more degrees of freedom in this scenario. Therefore Lothe and Pound insisted that a more correct expression for free energy would be –

$$\Delta G = \Delta G' + \Delta G_{tr} + \Delta G_{rot} + \Delta G_{rep} \quad (6.8)$$

$\Delta G'$ is the same energy as given in equation (6.2) i.e. $\Delta G = -\frac{4}{3}\pi \frac{r^3}{v_l} k_B T \ln S + 4\pi r^2 \sigma$ which

represents the energy of a nucleus confined in a bulk liquid. The remaining energies are corrections to replace the liquid phase with vapor phase.

ΔG_{tr} and ΔG_{rot} are the contributions of free energy due to the translational and rotational motions gathered by the cluster in the presence of surrounding temperature and pressure.

ΔG_{rep} is the replacement energy which accounts for the loss of six degrees of freedom of the nuclei attributed to the gain of translational and rotational gas like energies (Christian, 2002).

Equation (6.8) gives the free energy change of a cluster with its center of mass stationary.

Consequently ΔG_{tr} and ΔG_{rot} are both negative and signify the increase in entropy of a droplet in vapor whereas ΔG_{rep} is positive and signifies loss of entropy.

The corresponding expressions for partition functions of these motions are –

$$Q_{tr} = \left(\frac{2\pi m k_B T}{\hbar^2} \right)^{3/2} n^{3/2} v_v \quad (6.9)$$

Where m is the mass of the individual atom and v_v is the volume per atom in vapor phase.

$$Q_{rot} = \pi^{1/2} \frac{(8\pi^2 k_B T I)^{3/2}}{\hbar^3} \quad (6.10)$$

Where I is the moment of inertia

$$Q_{rep} = (2\pi n)^{1/2} \exp\left(\frac{s^l}{k_B}\right) \quad (6.11)$$

Where n is the number of molecules in the cluster and s^l is the entropy per atom in the liquid.

Thus

$$\Delta G_{tr} + \Delta G_{rot} + \Delta G_{rep} = k_B T \ln\left(\frac{Q_{tr} Q_{rot}}{Q_{rep}}\right) \quad (6.12)$$

All these terms put together yield the following expressions for the general nucleation equation (6.7)

$$g(\bar{x})_{LP} = \ln\left[1.183 \frac{(WRT)^4}{N_o^8 \hbar^6 dP_e}\right] - \ln S + 4 \ln \bar{x} \quad (6.13)$$

$$g'(\bar{x})_{LP} = \frac{4}{\bar{x}} \quad (6.14)$$

$$g''(\bar{x})_{LP} = -\frac{4}{\bar{x}^2} \quad (6.15)$$

where N_o is the Avogadro's number and W is the molecular weight (Katz, 1970)

6.3 Reiss, Katz and Cohen

Lothe and Pound (Lothe, et al., 1962) had simply assumed that the expression of free energy should include translational and rotational entropy but it was eventually concluded that the correction lacked significant experimental support. Reiss, Katz and Cohen (Reiss, et al., 1968) argued that the fluctuation of the center of mass with restricted boundaries should be

included in the model and the partition functions were calculated using a method called *standard phase integral*. They provide two limits for the rate of nucleation RKC1 and RKC2.

Instead of the term $\frac{Q_{tr} Q_{rot}}{Q_{rep}}$ Reiss, Katz and Cohen obtained the term $\frac{Q_{tr}^c}{Q_{tr}^d}$ which is equivalent to $\frac{V}{v^d}$.

Here Q_{tr}^c is the translational partition function for a liquid cluster in vapor phase and Q_{tr}^d is the corresponding partition function for a droplet in the bulk liquid. V is the volume of the entire assembly and v^d is the volume of the droplet over which the center of mass of the cluster fluctuates.

Again incorporating these changes for the general nucleation equation (6.7) we have (Katz, 1970)

$$g(\bar{x})_{RKC1} = 0.970 + 3/2 \ln \bar{x} \quad (6.16)$$

$$g'(\bar{x})_{RKC1} = 3/(2\bar{x}) \quad (6.17)$$

$$g''(\bar{x})_{RKC1} = -3/(2\bar{x}^2) \quad (6.18)$$

$$g(\bar{x})_{RKC2} = \ln[7.465RTd/WP_e] - \ln S + 1/2 \ln \bar{x} \quad (6.19)$$

$$g'(\bar{x})_{RKC2} = 1/(2\bar{x}) \quad (6.20)$$

$$g''(\bar{x})_{RKC2} = -1/(2\bar{x}^2) \quad (6.21)$$

6.4 On the Use of Classical Nucleation Theory in this Research

Figure 6-2 shows a comparison of experiments with the different theories explained above to choose a theory that easily serves the purpose in this research.

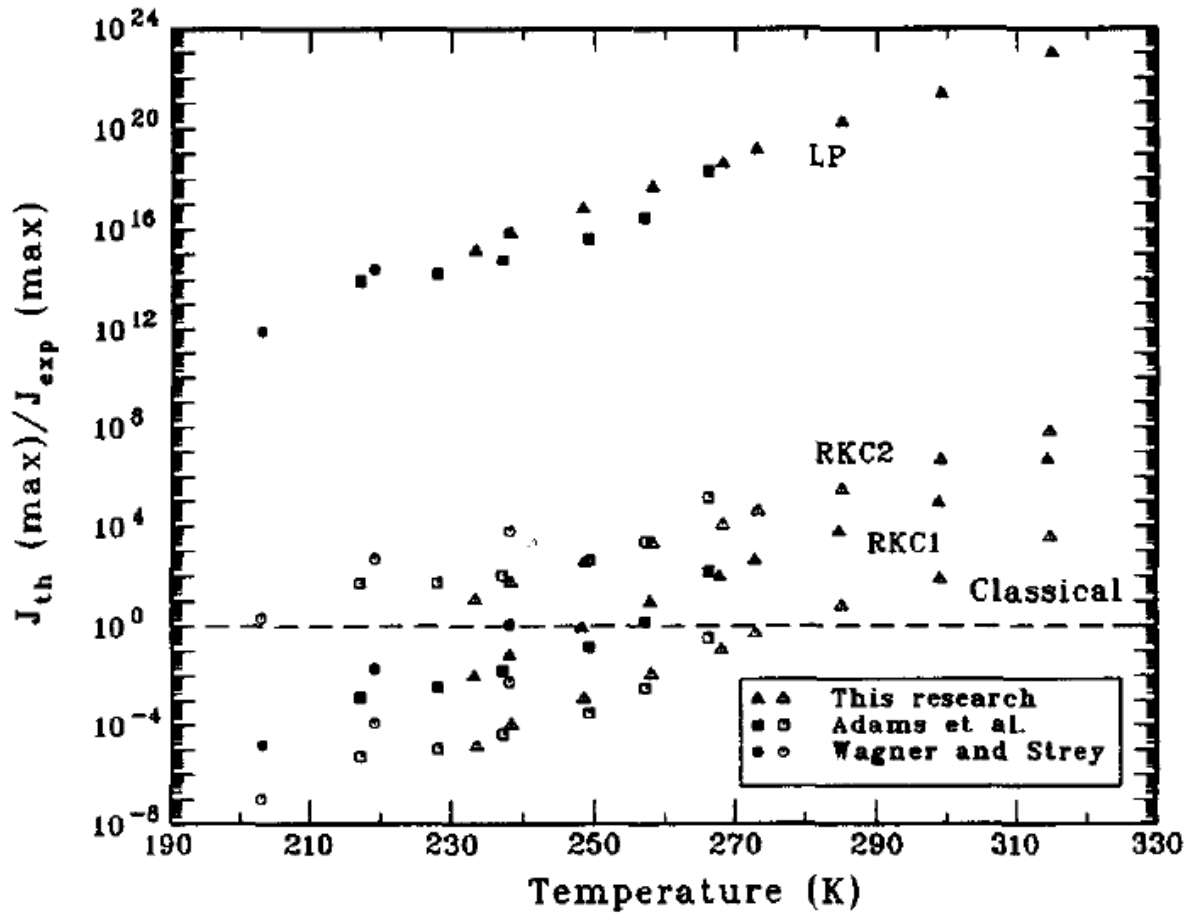


Figure 6-2 Comparison of all three theories to experiment (Hung, et al., 1989)

Figure 6-2 compares the experimental values with the calculated ones for the various nucleation theories (LP, RKC1, RKC2 and CNT). Ideally, if predicted correctly, all the symbols should lie close to ratio equal to 1. Only CNT comes closest to this criteria. As seen here (Hung, et al., 1989) while none of the theories are in perfect agreement with the experiments, the Classical Nucleation Theory happens to be the closest. RKC theories are fairly close as well but LP does not conform with the experiments at all. On further inspection it is seen that each theory has its uncertainties but CNT shows consistencies. Owing to these facts CNT has been used to model nucleation in this research.

For calculating the supersaturation ratio of MoO₂ monomers following equation has been used for saturation pressure for MoO₂ (Burns, et al., 1960)

$$\log P_{MoO_2(g)} = -2.936 \times 10^4 / T + 10.574$$

A new nucleation theory that is showing some promises is the Dillmann – Meier Theory. It is still under development stages, nonetheless a small section has been included in Appendix E for future reference and work.

6.5 Verification of Implementation of Classical Nucleation

Theory

As explained in Section 6.4 CNT has been used to model nucleation in this research. Prior to combining the module for nucleation it is essential to verify its proper operation.

Verification, as done in this section, entails solving the CNT equations for nucleation of *n-nonane* and confirming the values and trends with (Katz, 1970). The data for *n-nonane* needed for the simulation has been taken from (Hung, et al., 1989).

6.5.1 Nucleation with varying temperature

In the first case nucleation has been modeled at three different levels of supersaturation ratio [$S = (P/P_\infty) = 10, 7, 5$] with temperature varying from 300 K to 500 K.

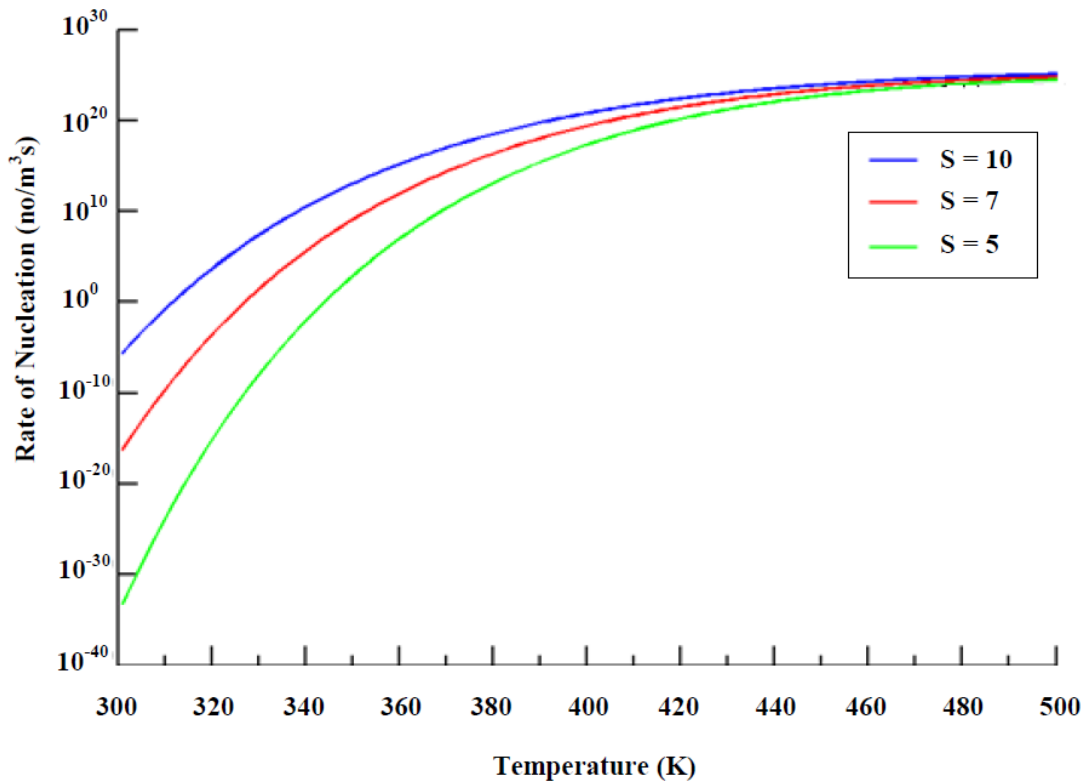


Figure 6-3: Rate of nucleation as a function of temperature at supersaturation ratios 5, 7, 10.

As can be seen in Figure 6-3 the rate of nucleation increases exponentially with temperature. Also for a higher level of supersaturation ratio higher nucleation rate is obtained. This is a result of a decrease in the surface energy of the critical nucleus. The same trend is observed in Figure 6-4. The number of monomer atoms required to create a stable nucleus also goes down with increasing temperature and increasing supersaturation ratio. These trends are in perfect agreement with the results presented in (Katz, 1970)

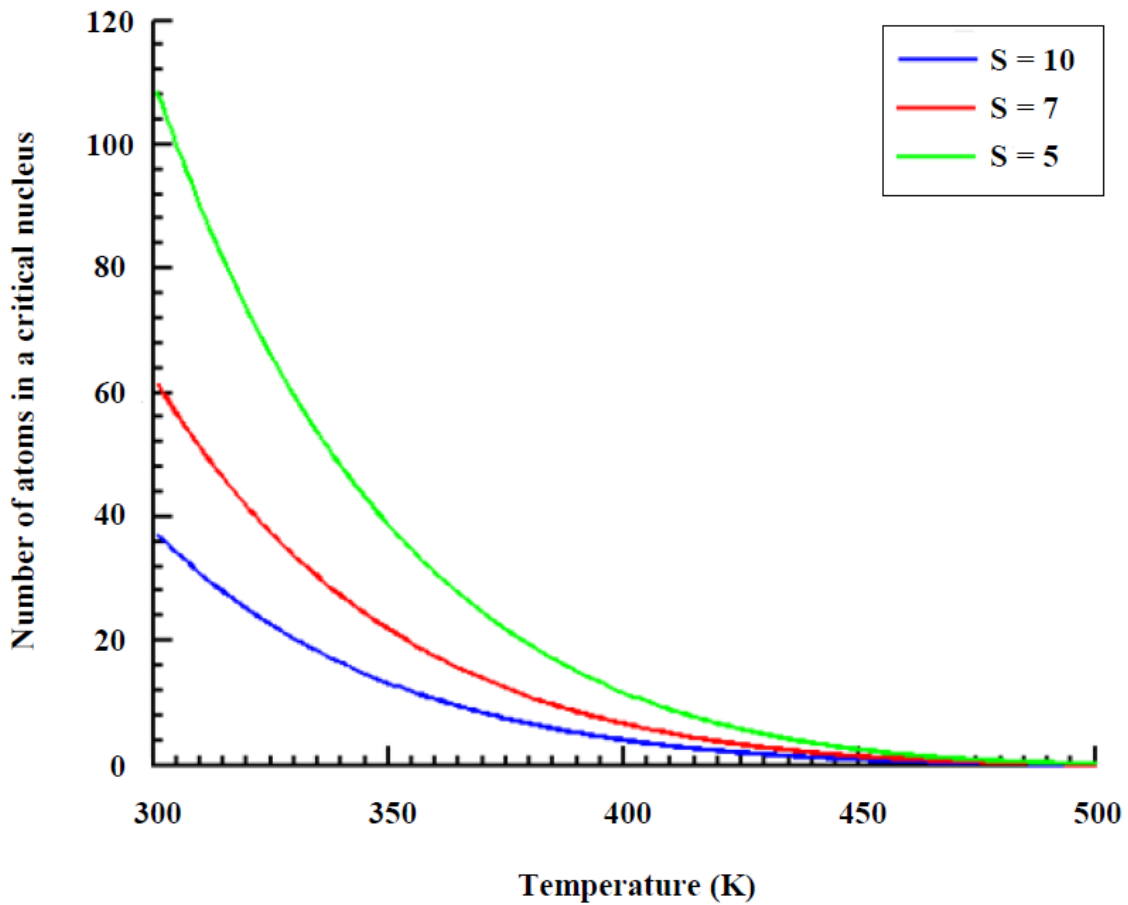


Figure 6-4: Size of critical nucleus vs Temperature for Supersaturation ratio = 10, 7, 5

6.5.2 Nucleation with varying supersaturation ratio

In this segment nucleation simulations of n-nonane have been carried out at varying levels of supersaturation ratios at three temperatures ($T = 300, 400, 500$ K)

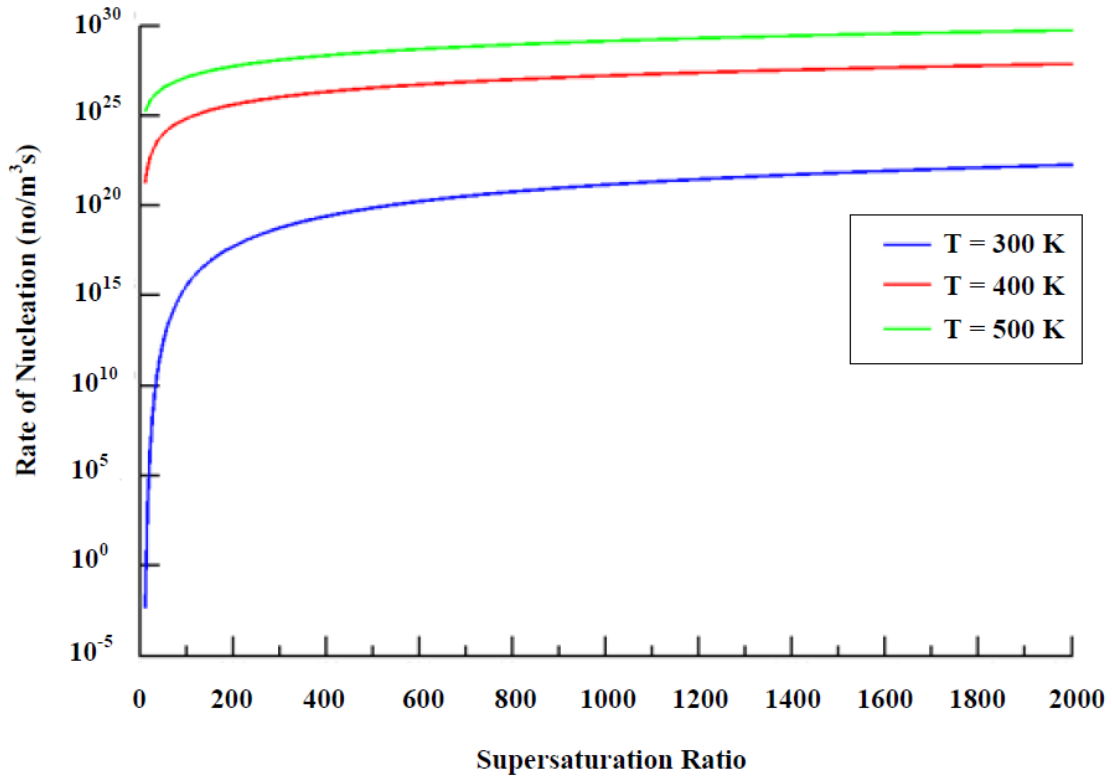


Figure 6-5: Rate of nucleation as a function of supersaturation ratio at $T = 300, 400, 500$ K

Rate of nucleation is extremely sensitive to the levels of supersaturation ratio and changes exponentially with it. In Figure 6-5 too the nucleation rate rises exponentially with supersaturation ratio and also increases with temperature.

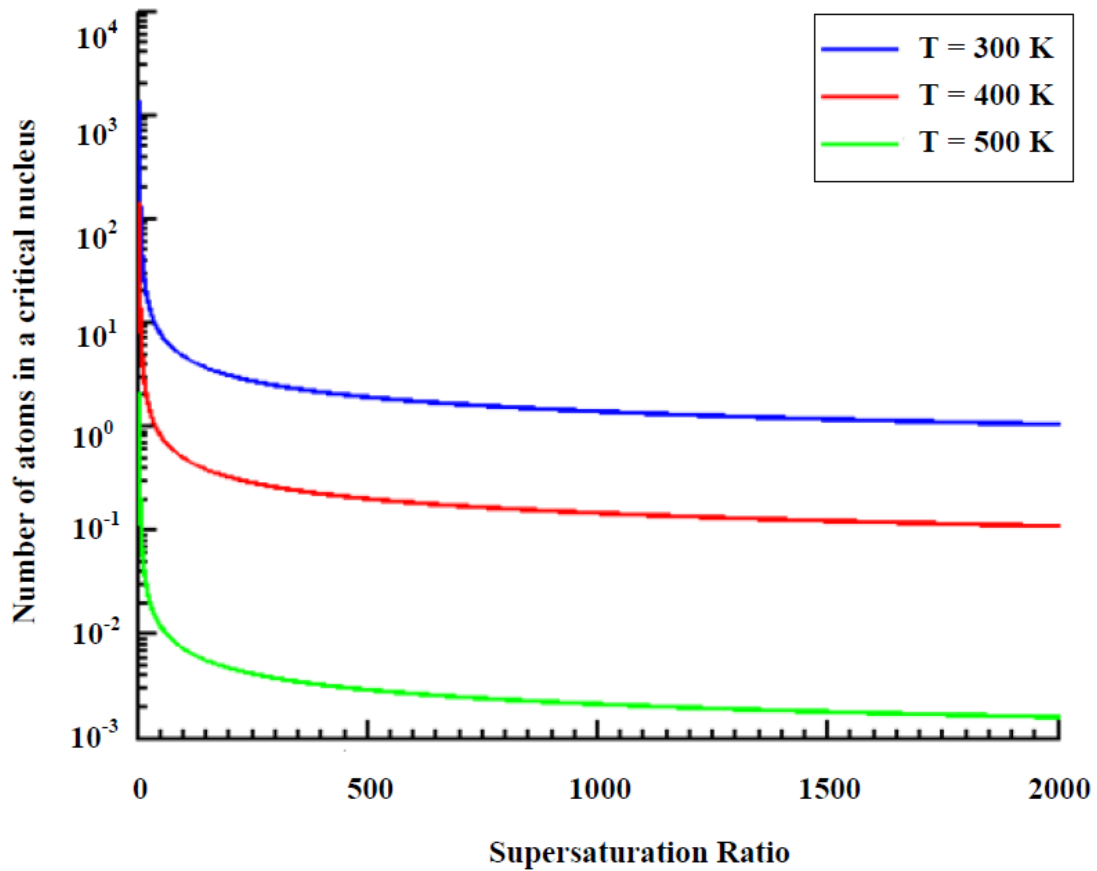


Figure 6-6: Size of critical nucleus vs saturation ratio at T = 300, 400, 500 K

Figure 6-6 shows the decrease in the size of the critical nucleus as the supersaturation ratio rises. The values show a very small critical nucleus, sometimes even less than one atom. This simply means that at these particular values of supersaturation ratio even a single atom is capable of acting as a stable nucleus. The values of supersaturation ratio for this simulation are rather high and are much smaller in a practical scenario. Again these trends follow the results shown in (Katz, 1970)

6.6 Conclusion for Nucleation Theory

Significant progress has been made in modeling nucleation. An alternative way of modeling nucleation which is not limited to the assumptions of macroscopic theories is to use computer simulations namely hybrid Monte Carlo and Molecular Dynamics. But these methods are still restricted due to limited computational capabilities. Until then we will have to rely on nucleation theories. CNT being the oldest of theories has a fair amount of completeness coupled with minimum complexity. As reported above several attempts have been made to improve CNT and remove its assumptions. But currently the level of accuracy of these theories is still being questioned and they are far from being perfect. So the CNT is still the only widely accepted method to predict nucleation behavior. It seems like Dillmann-Meier theory holds some promises but it too has certain contradictions, corrections of which are underway (Ford, 1993). But there still has been no consensus on them and some of them have even resulted in poorer calculations than the original theory. The next logical step seems to be a combination of these theories based on a similarity criterion. These theoretical advancements are being well supported by progress in experimental methods which will further provide impetus to the development of a comprehensive nucleation theory.

Chapter 7

Nanorod Growth Model

The structure of a nanocrystal is strongly dependent on the ambient conditions which affect the growth patterns. Understanding the growth mechanism is key to controlling the development of the nanostructures. Ideally crystal growth takes place under thermal equilibrium conditions dictated by the Wulff theorem (Herring, 1951) which states that the crystal surfaces form in a way to minimize the surface energy. The growth of nanorods however, is a kinetic process taking place deviating from the ideal behavior and proceeding with faster rates than equilibrium processes. The formulation of the dislocation theory in 1949 (Frank, 1949) marks a huge turning point in the knowledge of crystal growth from vapor or solution phase. The formation of acicular structures has been attributed to the Vapor-Solid (VS) mechanism (Pan, et al., 2001) which is primarily governed by surface energy minimization principle and kinetics.

There are two extreme models for the VS growth in a crystal. The first limit is the *layered growth* where the surface is atomically smooth so growth occurs as a consequence of nucleation of new layers and the other limit is *rough growth* where the surface is composed of many atomic layers which increase by addition of individual atoms.

7.1 Rough Growth

Crystals may be rough due to many reasons, either by their crystallographic orientation or due to surface defects. Rough surfaces imply the presence of *kink* sites (Venables, 1994). These are high energy sites readily available to the incoming monomer atoms for easy attachment. To be able to attach themselves to the crystal structure the atoms have to undergo an energy change. They have to overcome a kinetic barrier from their corresponding enthalpy of transition. These new bonds formed between the atom and the crystal are very strong and unlike the atoms landing on the smooth flat substrate these atoms remain attached to their kink positions and do not move. Equations and derivations of rough growth as applied to the model have been illustrated later in Section 7.5.1

7.2 Layered Growth

For atomically smooth surfaces growth proceeds through layered growth phenomena i.e. by formation of atomic layers on the surface and by advancement of these layers parallel to the surface the advancement of the layers involves two parts –

- i. formation of steps
- ii. lateral movement of these steps

The slower of these processes determines the rate of growth.

Crystal faces which lack defects generate steps by 2D nucleation and the rate of growth is determined by the frequency of formation of the 2D nuclei. 2D nucleation just like regular

nucleation is a free energy minimizing process and a critical supersaturation ratio is required to be overcome. The vicinal vertical face of the 2D nucleus becomes the source of steps for the growth of the layer (Figure 7-1). When the smooth crystal faces possess some defects they appear in the form of screw dislocations and again the edge of the screw behaves as an unvanishing source of steps for the atoms to attach (Figure 7-2).

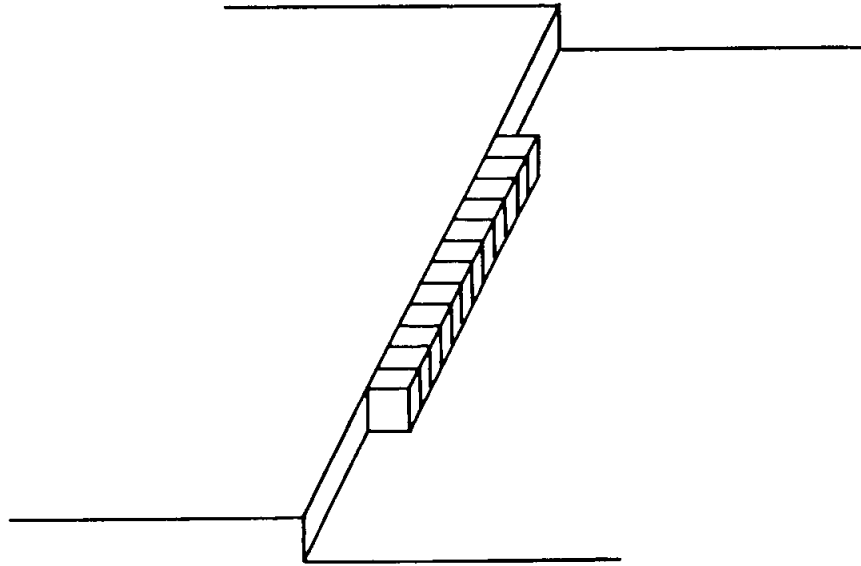


Figure 7-1: 2D nucleation

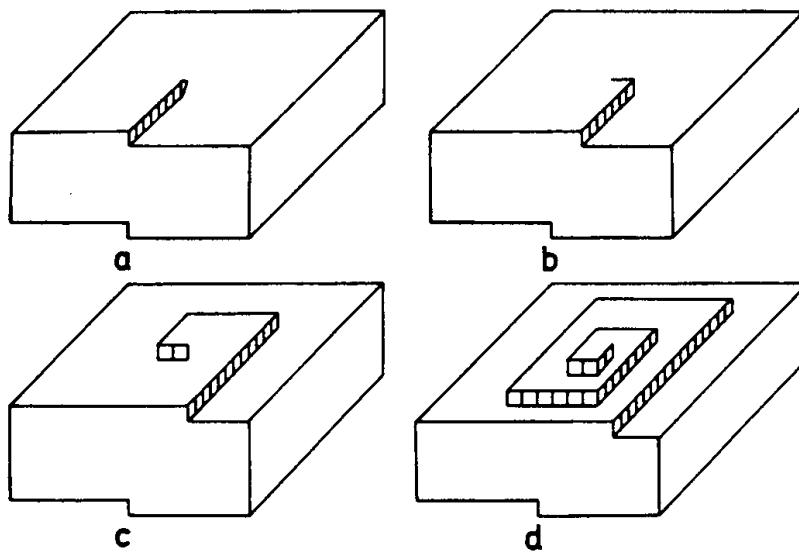


Figure 7-2: Growth by screw dislocation (Venables, 1994)

7.3 Growth Mechanism in Molybdenum Oxide Nanorods

The structure of nanoparticles seems to be highly dependent on the diameter of molybdenum probe used. As observed in the experiments (Figure 2-7) the use of 1.00 mm diameter molybdenum probe resulted in the production of nanorods while 0.75 mm diameter probe gave spherical nanoparticles. The phenomenon is intricately connected with the *supersaturation ratio*.

7.3.1 Chemical Potential and Supersaturation Ratio

The chemical potentials of two phases determine the equilibrium between them (Job, et al., 2006). Chemical potential is defined as the amount of work that is required to be done to change the number of particles in the system by unity

$$\mu = \left(\frac{\partial G}{\partial n} \right)_{P,T} \quad (7.1)$$

The chemical potential has two major characteristics –

- i. chemical potential measures the tendency to diffuse
- ii. chemical potential is a thermodynamic function that measures the phase change

Every substance has a tendency to change and transform into a new state or change its level of aggregation. Examples of this phenomenon are rusting of iron, melting of ice, weathering of rocks etc. This tendency can be quantified by the chemical potential. For a given substance the chemical potential depends on temperature, pressure and the concentration of particles in the substance. It also depends on the phase and degree of aggregation of the substance. So at

the same temperature and pressure liquid water, ice and steam have different values of chemical potential. Substances tend to move towards lower chemical potential values.

7.3.2 Phase Transition and Supersaturation Ratio

$\mu_A > \mu_B$: Phase A would change into phase B

$\mu_A = \mu_B$: No change of phase A into phase B

$\mu_A < \mu_B$: Phase B changes into phase A

Chemical potentials of most stable substances are negative.

Chemical potential changes with temperature, pressure and number of particles. When temperature increases the chemical potential decreases and it increases with pressure and number of particles. So any alteration to these conditions promotes a shift in the equilibrium of the chemical potential.

As long as the chemical potentials between two phases are balanced a perfect equilibrium between them is maintained but if any perturbation in the temperature or pressure causes any deviation in the state then an imbalance sets in which promotes a transition from one phase to another. This difference in the chemical potentials which is a function of pressure, temperature and number of particles behaves as the thermodynamic driving force for the crystallization. This difference in chemical potentials is -

$$\Delta\mu = \mu - \mu_{\infty} \quad (7.2)$$

where μ represents the chemical potential of supersaturated vapor and μ_∞ represents the chemical potential of the saturated phase

For a vapor-solid system (treating vapor as an ideal gas)

$$\Delta\mu = k_B T \ln \frac{P}{P_\infty} \quad (7.3)$$

Where P_∞ is the saturation pressure of the crystal phase and P is the partial pressure of the vapor. The ratio $\frac{P}{P_\infty}$ is termed as the *supersaturation ratio*.

This supersaturation ratio or $\frac{\Delta\mu}{k_B T}$ is expressed as the generalized driving force for crystallization (Sunagawa, 2005).

7.3.3 Variation of Growth Pattern with the Driving Force

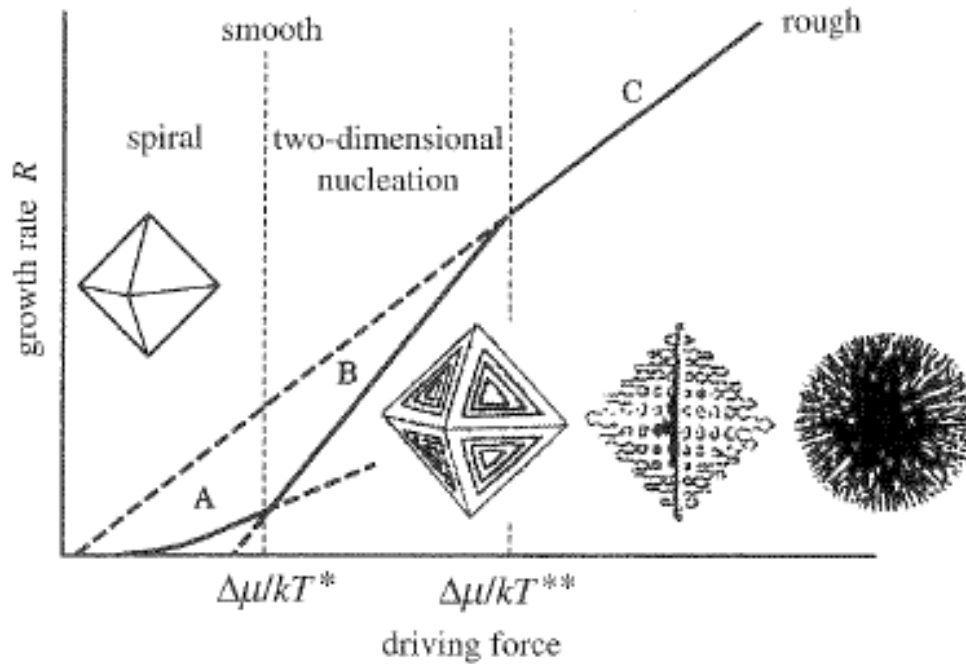


Figure 7-3: Variation in crystal growth pattern with the driving force (Sunagawa, 2005)

There are a couple of notable observations in this Figure 7-3.

- i. As the driving force $\left(\frac{\Delta\mu}{k_B T}\right)$ increases, the surface of the crystal gets rougher.
- ii. As seen in the figure there are three different growth regimes (A, B and C). The limits of driving force to these regimes are $\frac{\Delta\mu}{k_B T^*}$ and $\frac{\Delta\mu}{k_B T^{**}}$. The region C is the rough growth region. Above the second limit the growth takes place by random accumulation and adhesion of material. In the region A the surface is highly smooth and the growth occurs with 2D nucleation on the crystal sides or by spiral growth

mechanism. In the region B i.e. between the two limits is the transition but the growth still is smooth growth and principally by 2D nucleation.

If the driving force increases the rate of nucleation goes up as well resulting in the aggregation of many crystals.

7.3.4 Effect of Probe Diameter on Nanoparticle Morphology

The diameter of the probes plays an important role in determining their temperature once they are inserted into the flame. The probes begin to lose their thermal energy primarily through radiation which is dependent on the surface area of the substrate. Larger diameter probe has larger surface area and hence there is higher energy loss effectively reducing the temperature of the probe. Thus as measured in the experiments (Section 2.2) the temperature of the 1.00 mm probe is 1100°C and that of 0.75 mm probe is 1300°C.

A higher temperature probe (0.75 mm) results in a higher molybdenum oxidation and therefore a higher partial pressure (P) of the precursor atoms. This higher value of P gives a higher saturation ratio (equation (7.3)) and vice versa in the case of 1.00 mm probe. This firmly establishes the role of supersaturation ratio as the driving force behind the structure of the nanoparticles (Sunagawa, 2005).

A higher supersaturation ratio gives rise to spherical nanoparticles whereas nanorods are an outcome of a lower supersaturation ratio.

7.4 Different Growth Modes on Nanorod Surfaces

The source material vaporizes forming MoO_2 monomers. These monomers nucleate through homogeneous nucleation and form the first stage of growth for the nanoparticles. As more atoms arrive to join the nucleus the nanorod begins to take shape owing to the low level of supersaturation ratio. Newly arriving molecules will continue to deposit on the formed nucleus (Figure 7-4). The growth on the rough tips of the nanorod is due to the direct impingement of atoms (Markov, 1941) and diffusion of atoms from the smooth lateral surfaces (Blakely, et al., 1962) (Pan, et al., 2001) whereas lateral surfaces grow by layer growth due to 2D nucleation owing to lower bond energy (Chernov, 1984) (Gretz, 1967). At the high temperature pertinent to the experimental conditions the precursor atoms have high mobility. The side surfaces have low bond energies and in most cases are not able to prevent desorption of the incident atoms back to the flame volume. Although some atoms arriving on the surface are able to diffuse and nucleate into surface layers thus resulting in the slow growth of the lateral surfaces. The rough structure of the tip with high bond energy leads to a rapid accumulation of incoming molecules. Rapid diffusion of atoms takes place from the low energy smooth surfaces to the rough ends where these atoms attach themselves to the growth fronts and further facilitate the one dimensional growth of the nanostructure.

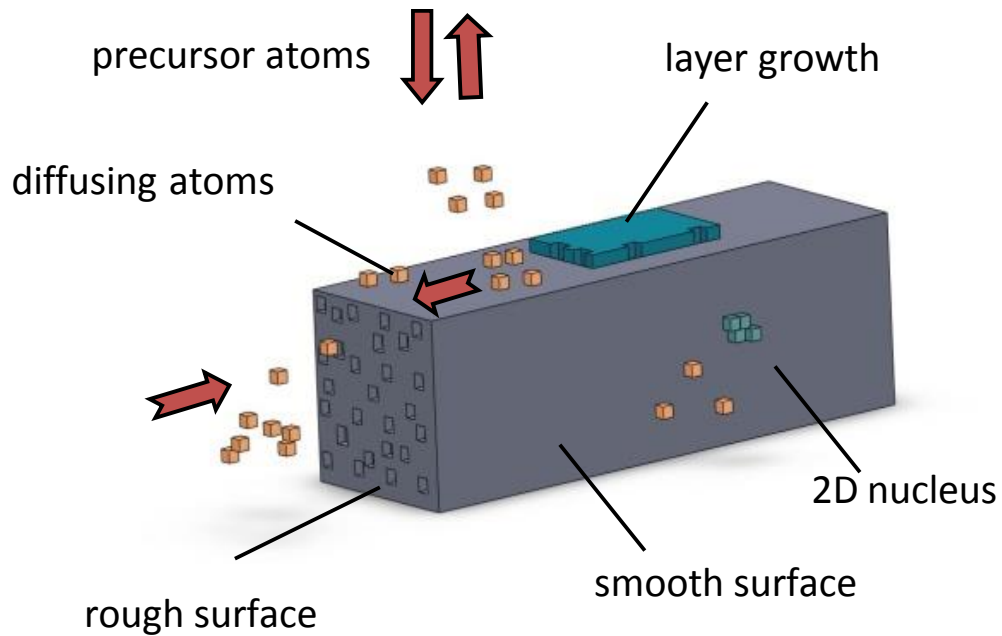


Figure 7-4: Schematic of a nanorod growth process showing direct impingement of atoms on the rough ends, diffusion of atoms on the nanorod surface, and 2-D layered nucleation.

7.5 Mechanism of Growth on Nanorod Tips

As mentioned in the earlier Section 7.4 the end faces of the nanorod are rough probably due to their crystallographic orientation. They possess an abundance of kink sites which are high energy sites that are available for easy attachment for the incoming monomer atoms (Figure 7-5).

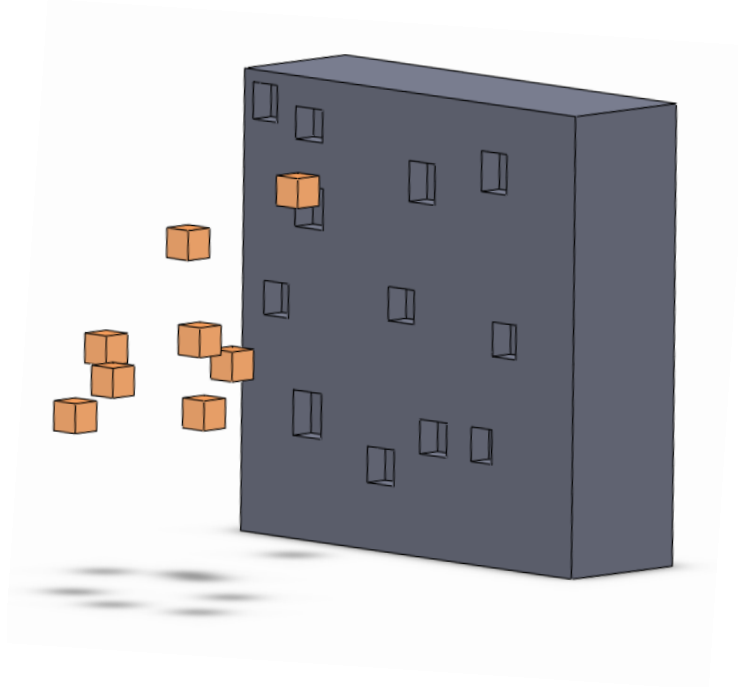


Figure 7-5: Attachment of monomer atoms to nanorod ends.

When the precursor atoms attach themselves to the end surfaces they have to overcome an energy barrier while shifting across the phase boundary between the crystal and the ambient phase (Figure 7-6). The energy at the kink site is much lower than the energy in the ambient phase since the final state is more stable. The difference between the two energy levels gives the enthalpy of the corresponding phase transition.

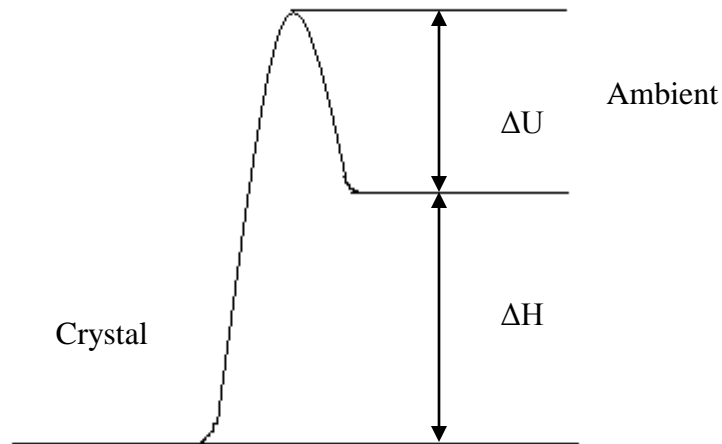


Figure 7-6: Variation of free energy across phases

The addition of precursor atoms to the nanorod ends takes place from two sources –

- i. Direct impingement
- ii. Diffusion of atoms from lateral sides

7.5.1 Direct Impingement

Direct impingement refers to the direct influx of monomer atoms from the ambient atmosphere. In this research the direct impingement implies the flux of MoO_2 atoms from the flame atmosphere.

The rate of growth is proportional to the net flux of atoms (Markov, 1941)

$$R_{dir} = a \left(\frac{a}{\delta} \right)^2 (j_+ - j_-) \quad (7.4)$$

where a is the dimension of the incoming monomer, δ is the average spacing between the kink sites, $(a/\delta)^2$ is the geometric probability of an incoming monomer to find a kink site, j_+ and j_- are respectively the fluxes of attachment and detachment of the monomers.

If $\frac{P}{\sqrt{2\pi mk_B T}}$ is the flux of atoms per unit area then from Figure 7-6 we have –

$$j_+ = \frac{P}{\sqrt{2\pi mk_B T}} a^2 \exp\left(-\frac{\Delta U}{k_B T}\right) \quad (7.5)$$

$$j_- = \nu \exp\left(-\frac{\Delta H + \Delta U}{k_B T}\right) \quad (7.6)$$

ν is the frequency of vibration of atom on the surface

In equilibrium $j_+ = j_-$ and $P = P_\infty$ where P_∞ is the saturation pressure

Thus

$$j_- = \frac{P_\infty}{\sqrt{2\pi mk_B T}} a^2 \exp\left(-\frac{\Delta U}{k_B T}\right) \quad (7.7)$$

Substituting (5.5) and (5.7) into (5.4)

$$R_{dir} = \left(\frac{a}{\delta} \right)^2 \frac{(P - P_\infty) a^3}{\sqrt{2\pi mk_B T}} \exp\left(-\frac{\Delta U}{k_B T}\right) \quad (7.8)$$

As can be seen from equation (7.8) the rate of growth of length of nanorod is directly proportional to the surface roughness in terms of the probability to find a kink site $(a/\delta)^2$

R_{dir} is the rate of increase of nanorod in (m/s) by the contribution from direct impingement.

7.5.2 Diffusion of Atoms from Lateral Sides

The precursor atoms landing on the nanorod lateral surface undergo various processes as shown in Figure 7-7.

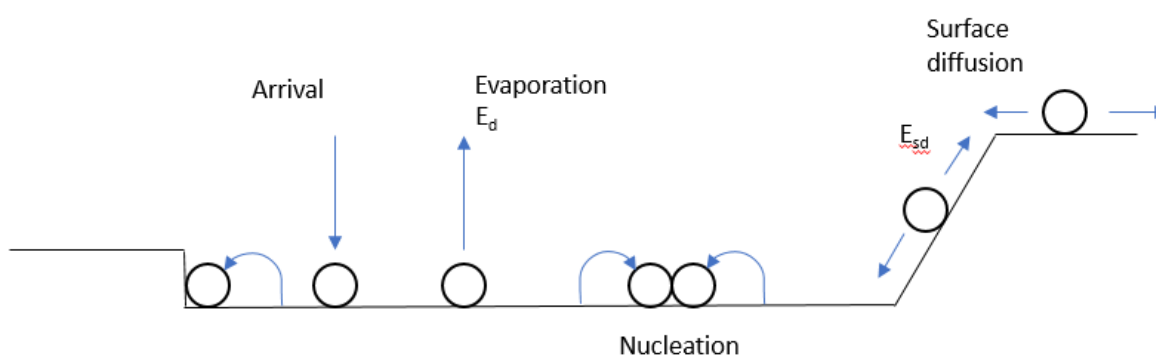


Figure 7-7: Various atomic processes taking place on the surface

As explained before the lateral surfaces of the nanorod are low energy surfaces. The incoming atoms are highly energetic and thus start to migrate owing to their inherent thermal energy. They follow a principle of *Competitive Capture*. Some of these highly energetic atoms, after traversing a mean displacement on the surface escape back into the ambient atmosphere. However some of the atoms, after diffusing on the low energy surface are able to bind together to form small islands of growth. Thus promoting 2D nucleation discussed later in Section 7.6. A few of these diffusing atoms cross from the lateral surfaces over to the

nanorod ends and attach themselves to the available kink positions. This diffusion flux acts as the second source of increase of length of the nanorod. The numerics of this phenomenon are presented in this section.

A flux of atoms N arrives on the surface (Venables, 1994)

$$N = \frac{P}{\sqrt{2\pi mk_B T}}$$

This constantly increases the number density (n_1) of single atoms on the surface with time

$$n_1 = Nt$$

The characteristics of diffusion of atoms on the nanorod surface are dictated by the energy of surface diffusion E_{sd} and the energy of adsorption E_d . Typically E_d is several times that of

E_{sd}

The diffusion coefficient of the surface is given by –

$$D_s = \left(\frac{\nu_{sd} a^2}{4} \right) \exp\left(-\frac{E_{sd}}{k_B T} \right) \quad (7.9)$$

ν_{sd} is the frequency of vibration parallel to the surface, a is the jump distance equal to the dimension of one atom.

The atoms leave the surface of the nanorod after a certain residence time τ_d

$$\tau_d^{-1} = \nu_d \exp\left(-\frac{E_d}{k_B T} \right) \quad (7.10)$$

ν_d is the atomic vibration frequency parallel to the surface which is of the order of 1-10 THz.

The diffusion coefficient and the residence time determine the average displacement (x) of an atom from the time of its arrival to the time of its desorption.

$$x = \sqrt{D_s \tau_d}$$

$$x = a \sqrt{\frac{v_{sd}}{v_d}} \exp\left[\frac{(E_d - E_{sd})}{2k_B T}\right] \quad (7.11)$$

Since $E_d \gg E_{sd}$ the ratio of x to a is quite large and hence during its journey the atom comes across many other diffusing atoms and either binds with them depending on the binding energy or maintains its course.

During this interval the diffusing atom encounters a number of substrate sites given by $\frac{D\tau_d}{N_d}$

where N_d is the average site density.

Some atoms incident on the lateral surface close to the nanorod ends diffuse towards the rough ends and attach themselves. To calculate the increase in length due to this attachment process it is imperative to compute the concentration of the adsorbed atoms.

Let N be the number of atoms condensing on the whisker per cm^2 per second and let N_A be the number of adsorbed atoms per cm^2 on the whisker lateral surface. Then from the transport balance

$$\left(\frac{\partial N_A}{\partial t}\right) dx = D_s \left(\frac{\partial^2 N_A}{\partial x^2}\right) dx + N dx - \left(\frac{N_A dx}{\tau_d}\right) \quad (7.12)$$

For the steady state this equation reduces to –

$$\frac{\partial^2 N_A}{\partial x^2} + \frac{N}{D_s} - \frac{N_A}{D_s \tau_d} = 0 \quad (7.13)$$

To solve this equation a variable grid was set up on the nanorod lateral surface to track all the transport processes taking place. The grid changes its shape with the growing nanorod and also varies its resolution depending on the concentrations and gradients of diffusion present on the surface. *Equation (7.13) forms a system of implicit equations and the procedure of solution has been given in detail in Appendix D.*

The rate of increase in length of the nanorod due to diffusion is given by –

$$R_{diff} = N_A' \left(\frac{4a^3}{\pi d^2} \right) \quad (7.14)$$

where N_A' is the number of atoms reaching the rough ends through diffusion and d is the diameter of the nanorod

$$N_A' = D_s \frac{\partial N_A}{\partial x} \pi d \quad (7.15)$$

So the total increase in length of the nanorod is the sum of R_{dir} and R_{diff}

7.6 Mechanism of Growth of Lateral Surfaces

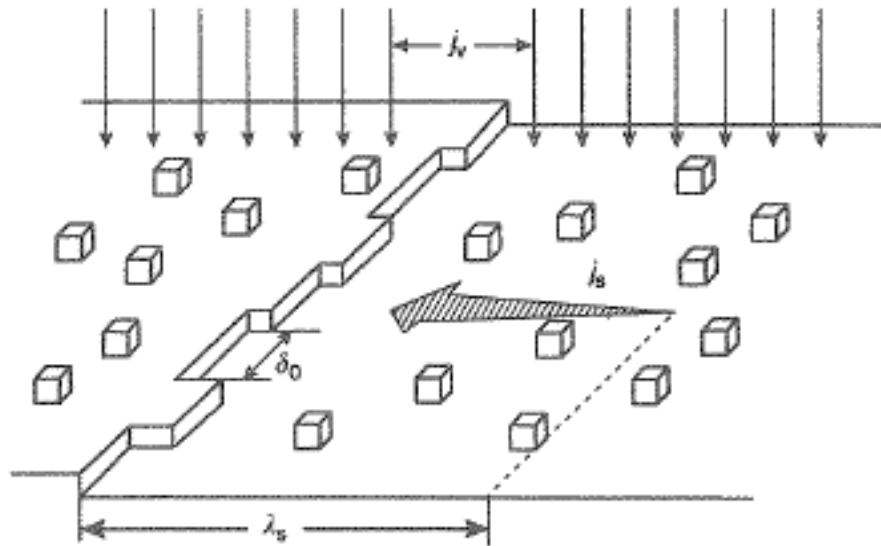


Figure 7-8: Depiction of the monomer flux and the diffusion flux of atoms (Markov, 1941)

During the course of its migration over the nanorod surface an atom encounters surface vacancies as well as other atoms. Depending on the probability of finding a vacancy or an atom the growth process of the surface will either involve attachment or 2D nucleation. The probability of forming a 2D nucleus again depends on the binding energy of the atoms and the inherent thermal energy of the migrating atoms. If 2D nucleation takes place they will form small clusters which will then grow to form large clusters in the form of two or three dimensional islands.

Surface diffusion is a perpetual process. Only at very low temperatures is it possible to suppress surface diffusion. However, at a very high value of supersaturation ratio the critical

size of a 2D nucleus could become equal to one atom. This forms the kinetic limit of surface nucleation and now the layer would grow just by cumulating atoms which stick as they fall onto the nanorod surface (Venables, 1994). At a low value of supersaturation ratio the growth of the surface is not at a significant speed but is mostly guided by dislocations and formations of layers (Burton, et al., 1951). These processes are comparatively more complex to model since they largely depend on the particular system and the surface conditions.

The newly formed 2D nuclei increase in size and number and finally merge together to form a new MoO₂ layer, thereby increasing the diameter of the nanorod. Details of this process are given as –

$$J_o = 4l^* aN\Gamma n_o \exp\left(\frac{E_{des} - E_{sd}}{k_B T}\right) \exp\left(\frac{\Delta G_2^*}{k_B T}\right) \quad (7.16)$$

$$\Gamma = \left(\frac{\Delta G_2^*}{4\pi k_B T n^{*2}}\right)^{1/2}, l^* = \frac{2\chi s_c}{\Delta\mu}, \Delta G_2^* = \frac{4\chi^2 s_c}{\Delta\mu}$$

where J_o is the rate of 2D nucleation, s_c is the area occupied by the surface atom, χ is the specific edge energy, E_{sd} is the energy of surface diffusion and ΔG_2^* is the free energy of nuclei formation on the lateral surface, n^* is the number of atoms in the critical nucleus and n_o is the density of sites.

The lateral rate of increase of diameter of nanorod is given by-

$$R_{dia} = J_o \pi d L a \quad (7.17)$$

where a is the size of the incoming monomer, L is the length of the nanorod and d is the nanorod diameter.

From equations (7.14), (7.15) and (7.17) it can be easily shown that the variation of nanorod length with respect to the nanorod diameter (R_{diff} / R_{dia}) is inversely proportional to d^2 . The limits to the smooth layered growth phenomenon are set by the rough growth by direct impingement. Rough growth takes over once this limit is reached.

Chapter 8

Particle Transport Model

A rigorous understanding of particle transport is essential in determining the crystal structure formed. Monomers and nanoparticles inside a flame experience a combination of various forces which govern the path that the particle takes. The trajectory of the nanoparticle decides the ambient conditions encountered by it which in turn are instrumental in shaping up the particle through the synergy of temperature and chemical species gradients. Particle trajectory also determines the residence time of the particle which plays a huge role in the development process. Higher residence time for the particle ensures sintering which further reduces the surface area of the particle.

Stokes, Einstein and Millikan have been credited with much of the concept for particle transport. The particle behavior being subjected to different forces was studied by them under ideal conditions of spherical particles. The non-ideal conditions involving non-spherical particles are usually studied in terms of deviations from this ideal behavior (Friedlander, 2000). Aerosol transport acts on different scales. On the large scale groups of particles are affected by the presence of concentration gradients, temperature gradients and electric fields if the particles possess charges. The gradients are mostly instrumental in bringing about the

diffusion of the clouds under various effects. The picture on the smaller scale however changes. On the individual particle level there is an exchange of mass, energy and momentum. These factors are highly dependent on the size of the particles and there is a coupling between large scale and small scale transport.

Particle behavior specifically depends on the Knudsen number (Kn).

$$Kn = \frac{2\lambda_m}{d_{part}} \quad (8.1)$$

where λ_m is the mean free path of the gas molecules and d_{part} is the characteristic diameter.

Mean free path is the distance travelled by a gas molecule between two successive collisions.

This depends on the average separation between two molecules in a gas but also takes into account the constant motion of the molecules.

$$\lambda_m = \frac{1}{\sqrt{2}n\pi\sigma_d^2} \quad (8.2)$$

n is the number of molecules per unit volume of the gas and σ_d is the diameter of the molecule.

Based on the Knudsen number where regions are defined in the particle field –

- i. Free molecular regime
- ii. Continuum regime

In the event of the particle diameter being much smaller than the mean free path ($Kn \gg 1$) molecules bouncing from a surface rarely collide with other adjacent molecules until far away from the surface, hence they are unable to affect the neighboring molecules and thus do

not have an effect on the rate of exchange of heat, mass, momentum etc. This range of flow is known as the *free molecular regime*.

When the diameter of the particle is much larger than the mean free path ($Kn \ll 1$) the dynamics changes. Now the particles leaving after striking a surface are easily able to affect their surroundings by imparting their momentum and energy. This kind of a scenario is called a *continuum regime*. Since a particle is strongly affected by its surroundings, the drag exerted on a particle now is much larger than in the free molecular regime.

The particle transport model developed here takes into account the flow regime of the particle and computes the trajectory based on their presence whether in the free molecular regime or the continuum regime. The primary forces considered in calculating the path of the particle are –

- i. Drag
- ii. Thermophoretic force
- iii. Weight of the particle

8.1 Drag

When a particle travels in a medium composed of large number of particles it experiences impacts from these surrounding particles which are at rest and imparts momentum to them. This resistance offered by the medium to the motion of the particles is experienced as *drag*. The momentum transferred by the particles depends on the type of collisions, whether they

are elastic or inelastic. Also, the entire shape of the particle is important not just the projected area as the molecules can receive or impart momentum to the sides as well as the rear.

There are mainly three types of resistance experienced by a moving particle in a stationary fluid (Reist, 1993) –

- i. Deformation drag which represents the force required to deform the medium to make path for the particle. This deformation affects the medium in all directions.
- ii. Frictional resistance which acts on the surface of the body.
- iii. Pressure drag because of the compression of the medium.

8.1.1 Stokes' Law

The resistance force experienced by a particle in a low Reynolds number flow is given by the Stokes' Law. Stokes Law has the following assumptions –

- i. Medium should be continuous
- ii. Medium should be incompressible
- iii. Medium should be viscous
- iv. Particles should be spherical
- v. Particles should be rigid

Any deviations from these assumptions are treated as a variation to the Stokes' Law.

Stokes' Law states that

$$F = 3\pi\mu\omega d_{part} \quad (8.3)$$

where F is the resistance force, μ is the dynamic viscosity, v is the relative velocity between the particle and the medium and d is the diameter of the sphere. The conditions encountered by the nanoparticles in their growth don't always satisfy the assumptions stated above. To broaden the application of the Stokes Law to include the possible realistic scenarios various correlations and correction factors have been suggested.

Non-Continuous Medium

For a large particle ($Kn \ll 1$) the medium behaves as a continuous medium i.e. the particle undergoes rapid collisions but for a small particle the medium ceases to be continuum since the particle now approaches the dimensions of the mean free path. For a large particle the viscosity plays the role of the major resisting force whereas for a small particle viscosity is no longer essential. This is now done by the inertial of the particles in the rarified medium. Due to this the resisting force for the particle should also decrease in the right measure. Instead of the entire shape the resistance force. For this a correction factor has been introduced by (Cunningham, 1910).

$$F = \frac{3\pi\mu v d_{part}}{C_c} \quad (8.4)$$

$$C_c = 1 + Kn \left[A + Q \exp\left(-\frac{bd_{part}}{2\lambda_m}\right) \right] \quad (8.5)$$

Kn is the Knudsen number given by equation (8.1). A , Q and b are empirical constants given in Table 8-1

Table 8-1: Values for various Cunningham corrections constants

<u>Constant</u>	<u>Value</u>
A	1.257
Q	0.40
b	1.10
A + Q	1.65

The value of C_c goes to 1 as the diameter of the particle goes to about 10 μm

Non-Spherical Particles

Stokes' law as derived is applicable only to spherical particles. Aerosols being in liquid form always possess spherical structure but nanoparticles can have varied shapes depending on the amount of sintering, agglomeration and flow gradients e.g. nanorods. In such cases variations to the Stokes law have been suggested (Leith, 1987).

According to Stokes' formulation the pressure drag amounts to one-third of the total drag on the spherical particle and friction drag amounts to the remaining two-thirds. Hence it was conjectured that the form drag in non-spherical particles came from the projected cross-sectional area of the object normal to its motion and the frictional drag was from its surface area. The correction to the law is as follows –

$$F = 3\pi\mu\omega d_n \kappa_n \quad (8.6)$$

From experiments following formula was developed (Johnson, 1985)

$$\kappa_n = 0.357 + 0.684 \frac{d_s}{d_n} + 0.00154\psi + 0.0104A$$

ψ = (axis parallel to direction of motion)² / (projected area normal to direction of motion)

A = ratio of the longest axis to the shortest axis in the projected area normal to the direction of motion.

d_n is the diameter of the sphere whose projected area is the same as the normal projected area of the moving particle, d_s is the diameter of the sphere whose effective surface area equals that of the particle.

8.2 Thermophoretic Force

Thermophoretic force is the result of thermal gradients and differs from convective force as it acts on individual particles rather than the entire group. A dust free region was first reported surrounding a hot body (Tyndall, 1870) which formed a seemingly impenetrable zone and it was observed that particles moved from hot to the cold region of space.

At significant temperature gradients thermophoretic forces have great effects. Particularly when hot gases flow over cooler surfaces e.g. in heat exchangers the particles carried by these gases accumulate on the heat exchanger surface forming scales, thereby reducing the heat transfer coefficient. Another such phenomenon is observed in boilers and chimneys before equilibrium temperatures are reached. Thermophoretic forces also have some beneficial effects including *thermophoretic sampling* of particles as has been used in this research (Section2.1.1).

8.2.1 Theory

Gas molecules are in a state of continuous motion. The energy of these molecules is governed by the temperature of the gas. The region which has a higher temperature has more energetic molecules than the colder region and hence they have higher velocities. When a particle is placed in this velocity gradient the momentum imparted to the particle from the hot region is much more than the momentum imparted from the cold region. This difference in momentum creates a net force directed from the hot region to the cold region. Therefore a section of the hot region becomes permanently impenetrable for the particles. The thermophoretic force among other things depends on –

- i. Ratio of particle size and pressure of the medium
- ii. Knudsen number (free molecular regime or continuum regime)
- iii. Velocity distribution of the gas molecules

8.2.2 Thermophoretic Force in the Free Molecular Regime

A particle is said to be in the free molecular regime when its diameter is much smaller than the mean free path of the gas molecules. The Knudsen number in this case is greater than one ($Kn \gg 1$). In such a case molecules colliding with a particle have to travel a significant distance before they can collide with the particle again or before colliding with other molecules. Due to this a colliding molecule is unable to alter the velocity distribution of the neighboring gas molecules and the effect of the collision is immediately lost. Hence each molecule behaves as an individual entity and transfers its own momentum to the particle.

The expression for the thermophoretic force as given by (Waldmann, 1959) (Derjaguin, et al., 1960) –

$$F_T = -\frac{1}{2} \pi \mu \nu \frac{d^2}{\lambda_m} \frac{\nabla T}{T} \quad (8.7)$$

where μ is the dynamic viscosity, ν is the kinematic viscosity

For a detailed derivation please see Appendix C

To determine the thermophoretic velocity the expression for thermophoretic force is equated to the Stokes force using the Cunningham factor $C_c \approx Kn(A+Q)$

$$v_T = \frac{1}{3} \nu (A+Q) \frac{\nabla T}{T} \quad (8.8)$$

Applying the value of $A+Q = 1.65$

$$v_T = 0.55 \nu \frac{\nabla T}{T} \quad (8.9)$$

As seen here thermophoretic velocity is independent of particle diameter d .

8.2.3 Thermophoretic Force in the Continuum Regime

A particle is said to be in the continuum regime when its diameter is greater than the mean free path of the gas. Thermophoretic analysis in the continuum regime is increasingly complex than the free molecular regime because of several factors which alter the distribution of velocity of the gas molecules in the presence of the particle.

Firstly, by changing the velocity of surrounding molecules on impact. After colliding with the particle the molecules are certain to collide with it again. Also these molecules with their

altered velocities collide with their neighboring molecules. Thus changing the entire distribution of the molecular velocity.

Secondly, the particle surface itself is instrumental in altering the velocities of the neighboring molecules through thermal energy and momentum exchange. The surface of the particle dictates the type of rebound, whether the collision will be diffuse or specular. The kind of rebound depends both on the particle as well as the gas composition. So both the factors should be taken into consideration.

The effect of the particle surface on the thermal energy transfer is rather complicated. The thermal conductivity of the particle controls whether the particle will act as a heat source or sink for the colliding molecules. If the particle acts as a heat source then it adds to the velocities of the outgoing molecules and if the particle behaves as a heat sink then it subtracts a portion of the velocity from the outgoing particles. Thus again altering the nearby velocity distribution. Another source of thermal affect is known as *thermal creep*. It has been long established that the molecules in a gas flowing over a surface slide from colder to the hotter regions (Niven, 1965). However, if there is a flow of gas at the surface of the particle up the temperature gradient, then the force causing this flow must be countered by an opposite force acting on the particle so that the particle itself moves in an opposite direction down the temperature gradient. This is known as *thermal creep* that induces a *velocity jump*. The complex phenomena of this thermal force is difficult to be described accurately even with most of the variables described.

A theoretical equation was set up by (Derjaguin, et al., 1965) to describe the thermophoretic effect on large particles

$$F_T = -H_D \frac{9\pi\mu^2 d_{part}}{4\rho_m T} \nabla T \quad (8.10)$$

where $H_D = \frac{2}{3} \frac{4 + C/2 + C_i Kn C}{1 + C/2 + C_i Kn C}$

C is the ratio of thermal conductivity of particle to the thermal conductivity of the surrounding medium (κ_p / κ_m)

$$C_i = \frac{15}{8} \left(\frac{2 - a_t}{a_t} \right)$$

where a_t is the thermal accommodation coefficient.

Derjaguin and Yalamov considered the particles to be large molecules submerged in a cloud of smaller molecules. Importance was also given to the slight movements initiated in the gas due to thermal stresses produced by the presence of the particle.

Earlier investigators had considered a temperature jump from the particle surface to the gas which produced a velocity jump in the molecules. However, Derjaguin and Yalamov concluded that the effect of the velocity jump was too small to produce any appreciable change in the system and hence this phenomenon was duly dropped in their analysis.

As in the previous case the thermophoretic velocity was calculated as –

$$v_T = -\frac{3}{4} H_D \nu \frac{\nabla T}{T} C_c \quad (8.11)$$

Chapter 9

Results of the Growth Model

As shown in Figure 3-1 the Growth Model consists of Monomer formation, Nucleation, Nanorod growth and Particle transport. All these models work in tandem to generate the resultant nanorod. The results presented in this section encompass the collective physics of all these above mentioned models and the discussions that follow give a holistic picture of the Growth model. As discussed earlier, the nucleation and growth stages are assumed to be occurring independently. So growth of the formed nuclei is considered only after the nucleation has ceased. Hence in all the plots presented below two different time scales are used (mentioned in the caption): *nucleation time* and *growth time*.

The molybdenum probes are inserted into the flame at a distance of 13 mm from the fuel nozzle. As the probe gets oxidized the monomers are formed in the *precursor vapor zone* and travel with the flame velocity towards the fuel nozzle as the gas velocity is directed towards it. Conditions in the flame dictate the onset of other growth processes. On finding favorable conditions nucleation starts in the *nucleation zone*. The nuclei that are formed travel further with the flame as they aggregate more material on their surfaces. This process of size increase occurs in the *growth zone*. Having completed the different phases of development

they finally reach the *stagnation plane* shown in Figure 9-1. The probe position of 13 mm has the highest temperature in the flame so as the monomers travel through the flame they encounter lower temperatures and a reducing atmosphere.

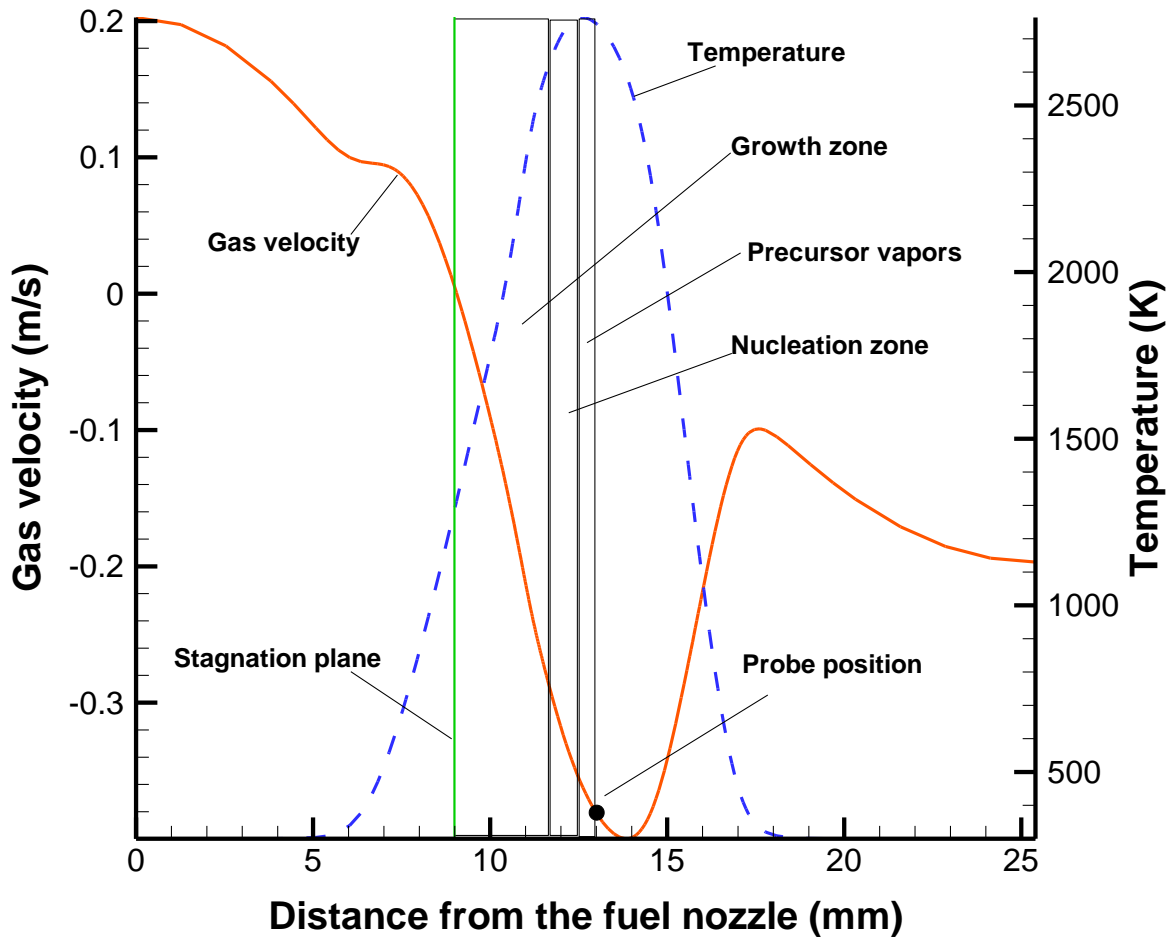


Figure 9-1: Zones in the flame for various nanorod growth processes

Now through their trajectory the saturation pressure of molybdenum dioxide varies as given below (Burns, et al., 1960)

$$\log P_{MoO_2(g)} = -2.936 \times 10^4 / T + 10.574 \quad (9.1)$$

The saturation pressure of molybdenum dioxide is directly proportional to the temperature. A decrease in temperature causes a decrease in the saturation pressure of the material. This decrease of saturation pressure of molybdenum dioxide results in the increase of supersaturation ratio $S = (P / P_\infty)$ which, as described in the previous chapters, is the primary driving force behind nucleation and crystal growth. The variation of saturation pressure through the trajectory of the nanorods is given in Figure 9-2.

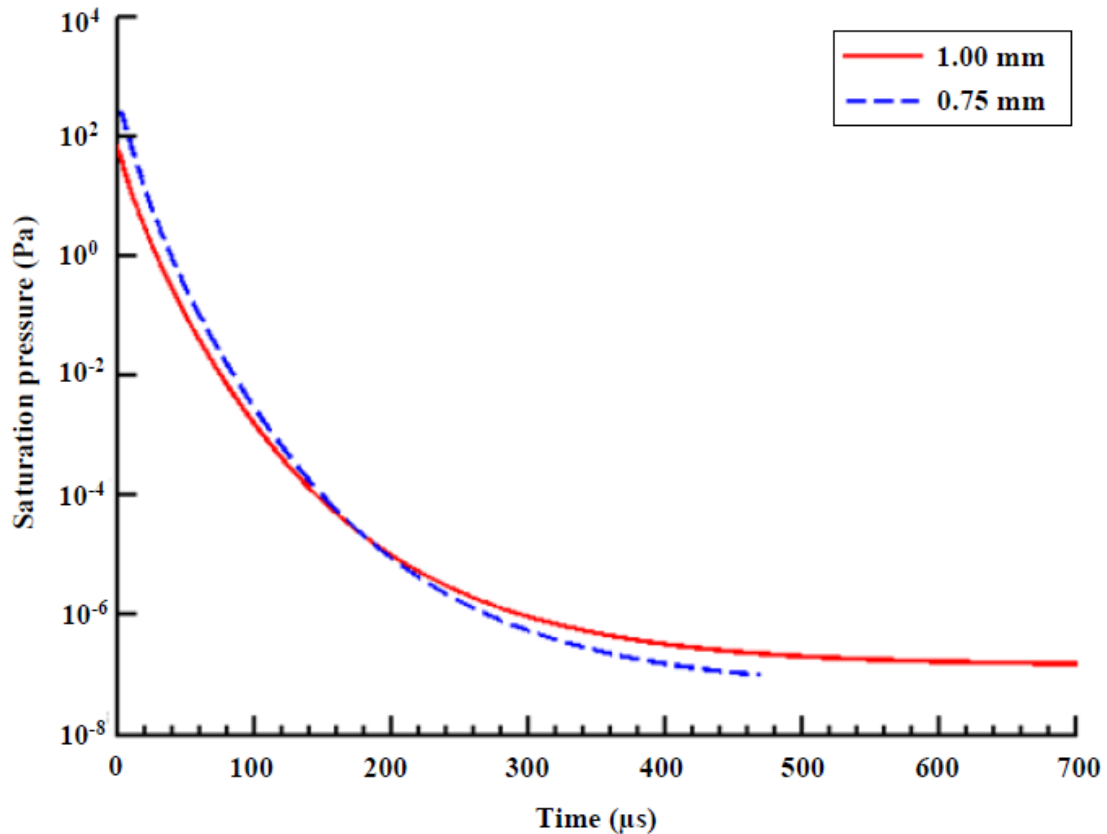


Figure 9-2: Variation of saturation pressure of MoO₂ through the nanoparticle trajectory with the growth timespan

Figure 9-2 shows the decrease of saturation pressure for the nanorods produced by the two different diameter molybdenum probes as they travel through the flame. Since the nanorods produced by these two different sources have a slightly different trajectory (as explained later in this section) they also experience slightly different temperature conditions. The saturation pressure decreases exponentially with temperature and hence provides favorable circumstances for the monomers to nucleate and grow quickly.

Molybdenum dioxide monomers are formed by material etching from the molybdenum probes placed in the flame. As discussed in Section 7.3.4 the 0.75 mm diameter probe results in a higher supersaturation ratio as compared to the 1.00 mm diameter probe. A higher value of the supersaturation ratio provides a higher impetus to the formation of critical nuclei. Due to this enhanced driving force the nuclei start to form earlier and also the rate of nucleation increases as given by equation (6.7). These stable nuclei form the centers of growth and later develop into molybdenum dioxide nanorods. Nucleation is a high monomer consuming process and depletes the quantity of monomers available for further nanorod growth. So there seems to be a tradeoff between the number of nanorods formed and the size the nanorods can grow up to. Lower supersaturation ratios reduce the rate of nucleation and at the same time also increase the size of stable nuclei by increasing the requirement of the number of atoms to form a critical nucleus.

Figure 9-3 presents the rate of nucleation by the two different sizes of molybdenum probes. As seen here the rate of nucleation is higher for 0.75 mm probe as compared to the 1.00 mm probe. Nucleation in 0.75 mm probe also begins earlier and attains a peak value much before the nucleation from 1.00 mm probe. There is however an assumption in the model. Nucleation is assumed to cease after it attains its maximum value. After that the growth phase starts and the model assumes all the stable nuclei to grow into nanorods.

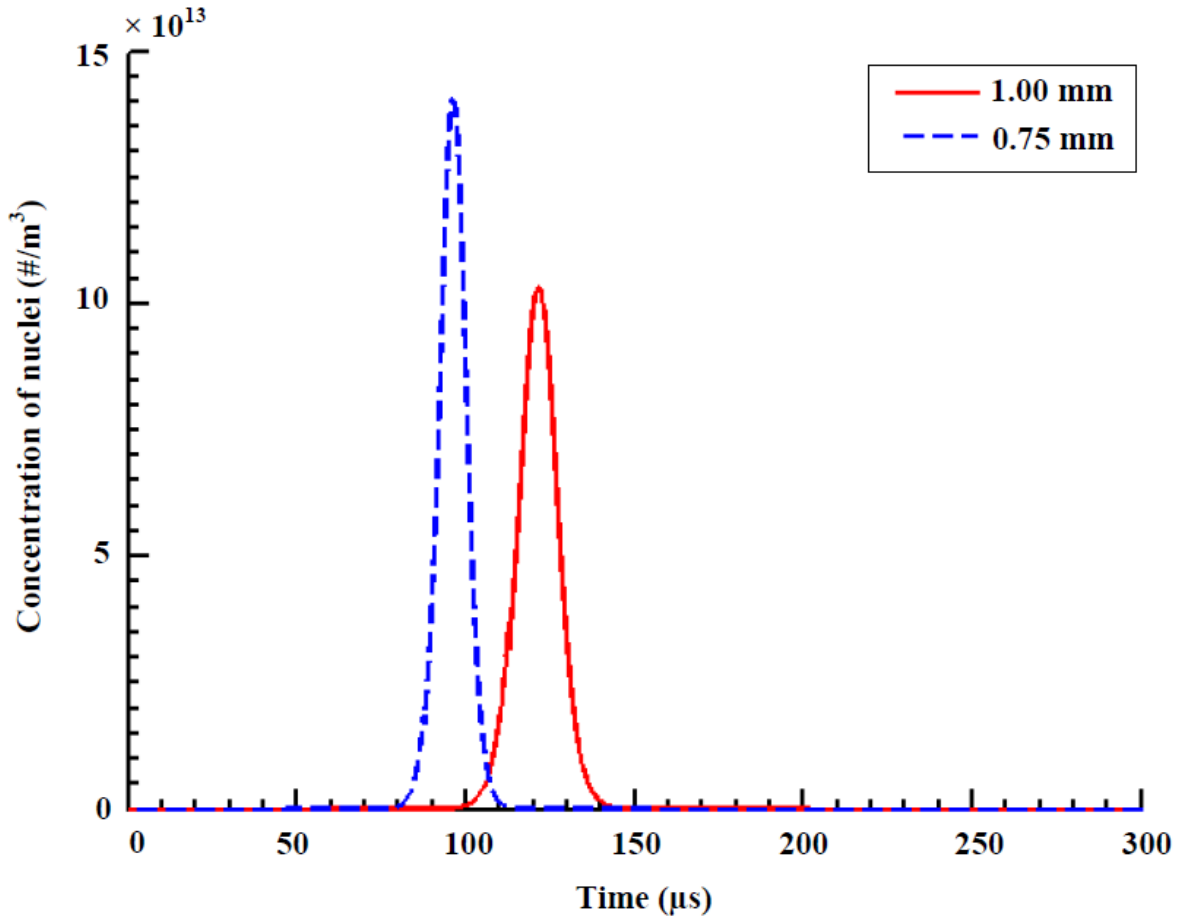


Figure 9-3: Rate of nucleation for 0.75 mm and 1.00 mm molybdenum probes during the nucleation timespan

As the material evaporates from the molybdenum probes the concentration of the formed monomers is represented in terms of their partial pressures. Nucleation and growth processes eat into the supply of these monomers until they are exhausted. To find the concentration of monomers equation (10.6) has been solved. It takes into account the depletion of atoms due to nucleation as well as nanorod growth. Figure 9-4 shows the change in concentration of

these monomers as the process of nanorod growth proceeds. The 0.75 mm diameter probe results in a monomer partial pressure of 6200 Pa and the 1.00 mm diameter probe results in a partial pressure of 4840 Pa.

The monomer partial pressure has been obtained from the monomer evaporation rates by calculating the monomer density in the instantaneous finite volume and using the ideal gas law.

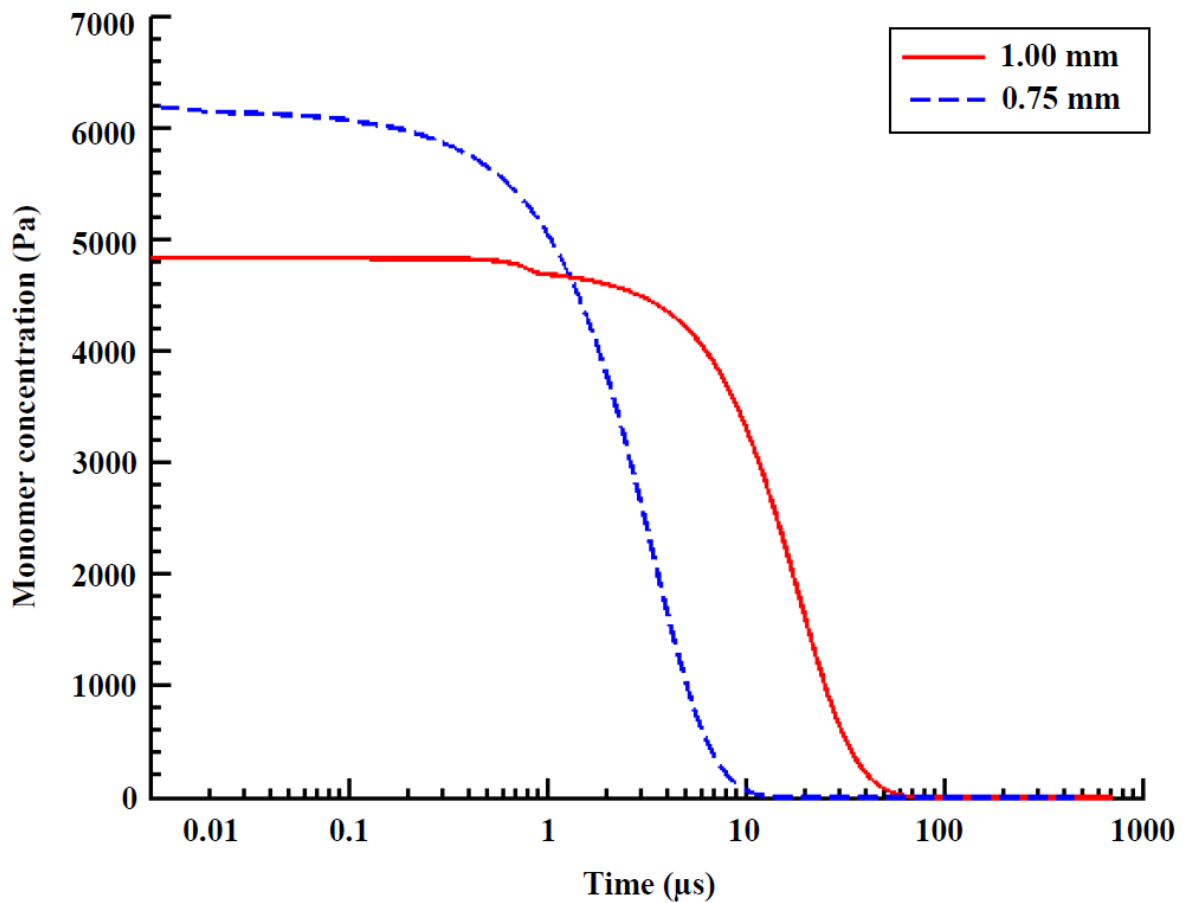


Figure 9-4: Variation of monomer partial pressure with the growth timespan

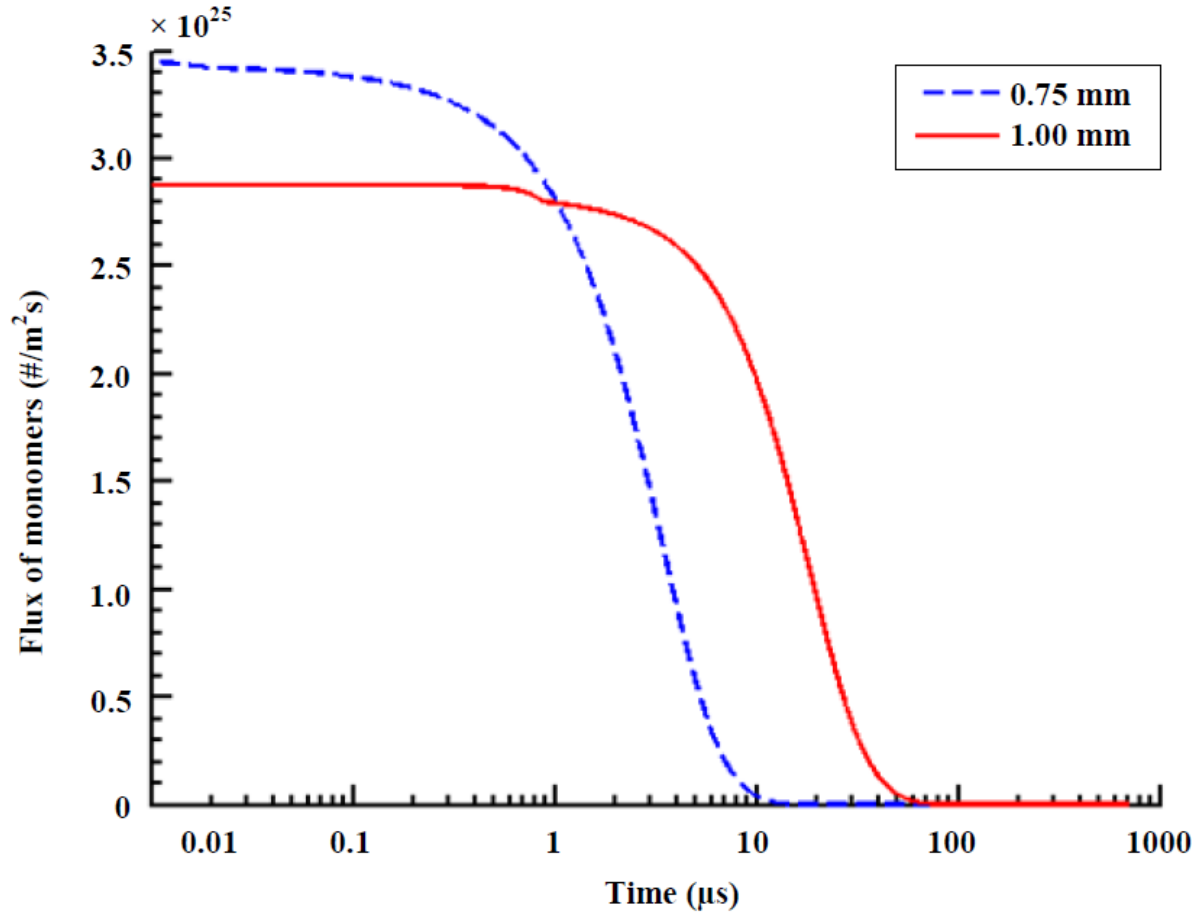


Figure 9-5: Variation of atomic flux on the growing nanorods with the growth timespan

Figure 9-5 shows the variation of the flux of monomer atoms on the surface of the growing nanorods. Figure 9-4 and Figure 9-5 bear resemblance since the monomer concentration in the atmosphere regulates the atomic flux by the equation $N = \frac{P}{\sqrt{2\pi mk_B T}}$. As the partial pressure (P) of the monomers falls due to depletion the monomer flux also decreases until all the supply is exhausted and the flux becomes equal to zero. This is when the nanorod stops to

grow and just traverses the path until it comes to rest at the stagnation plane. Again as can be seen in Figure 9-4 the concentration of monomers in the case of 0.75 mm diameter probe drops to zero before 1.00 mm probe. The reason for this is higher nucleation in the case of 0.75 mm probe. As stated earlier the smaller diameter probe produces more monomers and a higher saturation ratio but this also translates into higher nucleation taking place. More number of nuclei signify more growth centers and more number of growing nanorods. This large number of developing nanorods utilize the available monomers faster and hence in spite of having a monomer concentration in the beginning the partial pressure of monomers drops quickly to zero.

The next two figures (Figure 9-6 and Figure 9-7) show the nanorod growth patterns resulting from 1.00 mm and 0.75 mm diameter molybdenum probes. Figure 9-6 shows the variation of length and diameter of the nanorod from 1.00 mm probe whereas Figure 9-7 shows the variation of length and diameter of the nanoparticle from 0.75 mm probe. A comparison between the differing growth patterns of the two nanoparticles gives interesting insight into the underlying processes.

The length and diameter respectively of 1.00 mm probe nanorod are 48 nm and 3.6 nm. This results in an aspect ratio of 13.2 showing it to be an elongated structure. The larger diameter probe (1.00 mm) provides a smaller concentration of monomers and hence a lower value of supersaturation ratio. Low values of supersaturation ratio, as discussed in section 7.3.3, cause selective addition of incoming monomer atoms making smooth growth of lateral surfaces possible. The low energy side surfaces allow diffusion of atoms to take place which eventually join the nanorod ends and act as an additional source of building material. The

lateral surfaces however, grow at a slower pace than the rough ends which also accumulate incoming atoms through direct impingement. The reason for slower growth of side walls as stated in section 7.6 is the layer growth process which adds material through 2-D nucleation. This difference in the rates for the two surfaces causes the growth of an elongated structure in the case of a larger diameter probe.

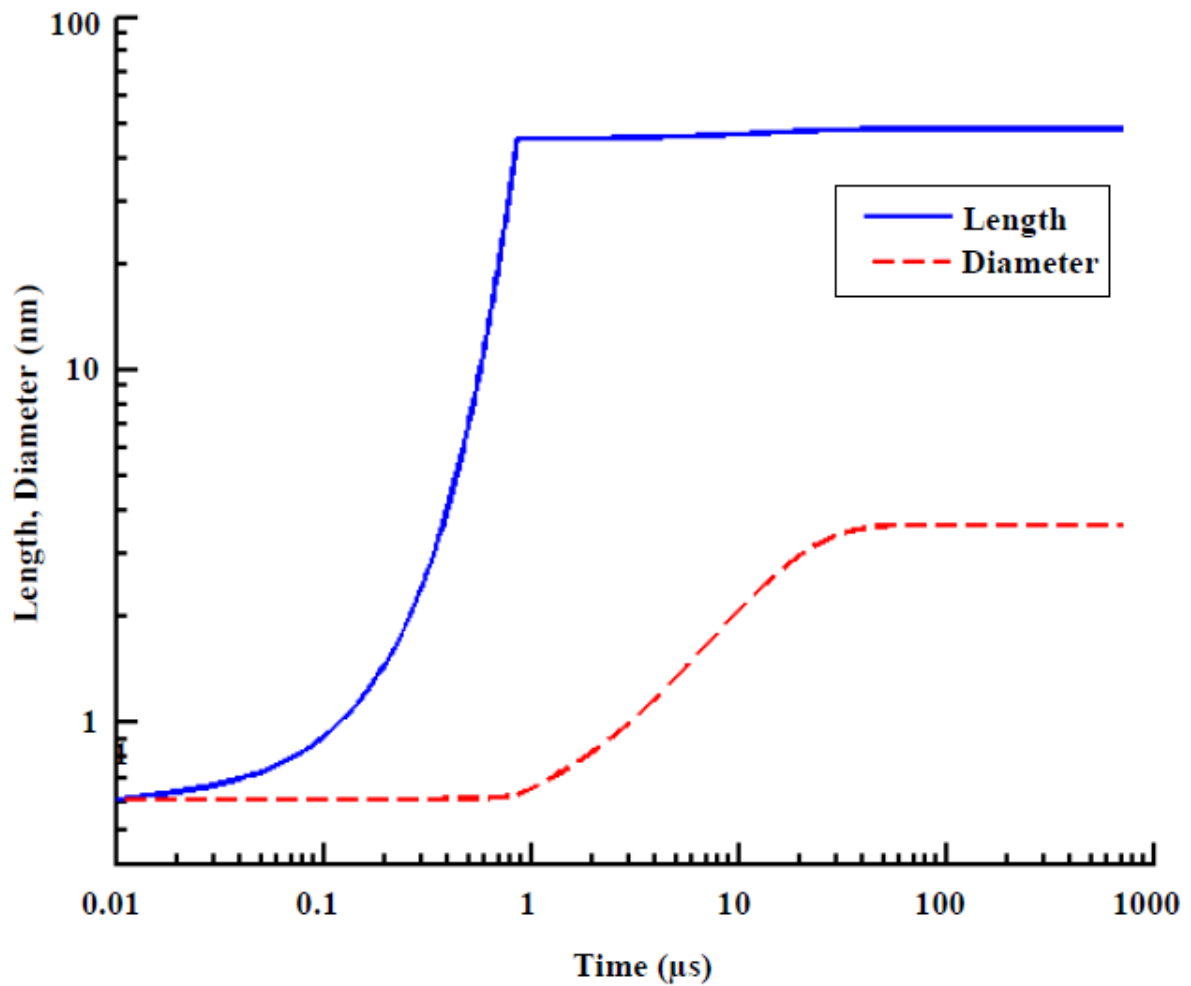


Figure 9-6: Variation of length and diameter of nanorod from 1.00 μm diameter probe with the growth timespan

Figure 9-7 compares the variation of length and diameter of the nanoparticle formed by the 0.75 mm diameter probe. This is markedly different from the result obtained with 1.00 mm probe. The length of the nanoparticle is 1.45 nm and the diameter is 1.4 nm giving it an aspect ratio of 1.02. This is akin to obtaining a spherical nanoparticle. There are no processes like surface diffusion or 2-D nucleation here. The spherical nanoparticle grows by accreting atoms which stick where they fall. The higher concentration of monomers resulting in a higher supersaturation ratio clumps the material together and there is no growth in a selective direction. Another important observation to make here is the small dimensions of the spherical nanostructure. This is because of the higher number of growing nanorods due to higher nucleating centers. The available material gets distributed among the huge number of particles.

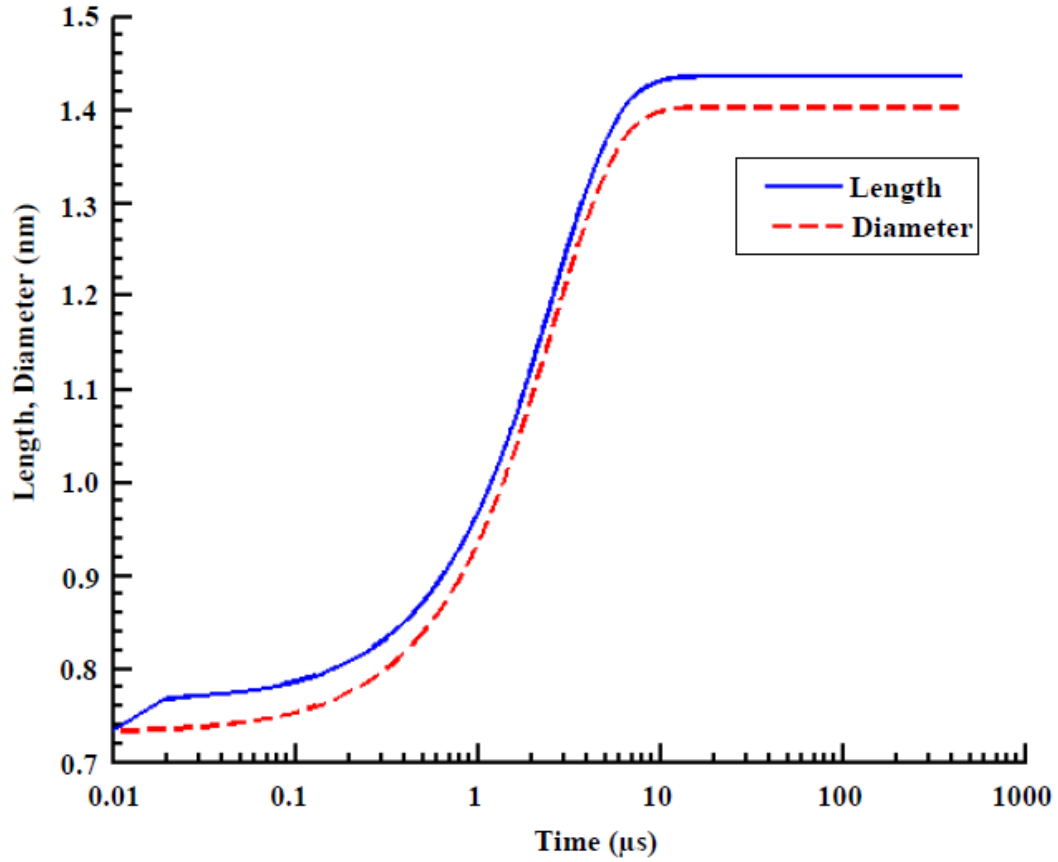


Figure 9-7: Variation of length and diameter of nanorod from 0.75 mm diameter probe with growth timespan

Another noteworthy observation is the plateau that exists in both Figure 9-6 and Figure 9-7. It represents the termination of significant growth for the nanoparticles. For 1.00 mm diameter probe it occurs around 60 μs and for 0.75 mm probe it occurs around 10 μs . This change in the growth pattern also conforms with Figure 9-5 which shows the decrease in the monomer flux. Since substantial supply of monomer is exhausted the growth of both the nanostructures slows down.

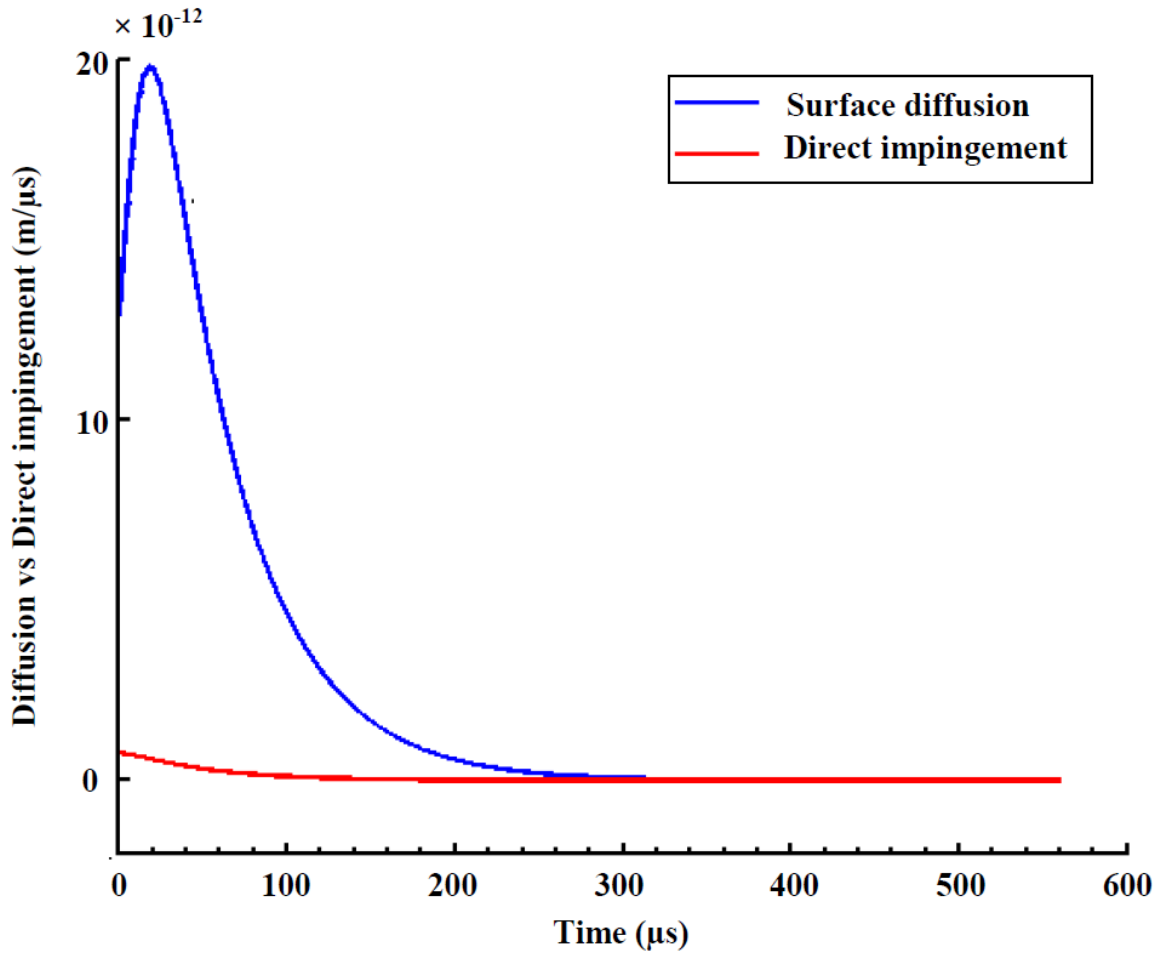


Figure 9-8: Comparison of the contribution to the rate of increase in nanorod length by surface diffusion and direct impingement with growth timespan

The one dimensionally growing nanorod has two sources of atoms to increase its length –

- i. direct impingement
- ii. surface diffusion

The purpose of Figure 9-8 is to compare the contributions that these two sources make towards the rate of increase in length of the nanorod. As can be seen, diffusion results in a much higher influx of atoms towards the rough ends than direct impingement. The prime reason for this phenomenon is that the surface area of the lateral sides within the migration distance of the atoms is larger than the area of the nanorod end. As shown in Section 7.5.2 diffusion is inversely proportional to the diameter of the nanorod. Hence as the diameter of the nanostructure increases with time the value of diffusion decreases asymptotically. The initial rise of the diffusion is owing to the small length of the nanorod at inception. In the beginning the length of the nanorod is much smaller than the surface diffusion distance for the monomer atoms before their desorption. Since most of the atoms reach the ends without leaving the nanorod surface the flux of atoms towards the ends is huge and results in the large value of rate of diffusion before it starts to decrease due to increase in nanorod length.

The formed nanoparticles travel through the flame experiencing various forces, namely Stokes' force and thermophoretic forces. These forces determine the trajectory taken by the particle (Figure 9-9). To solve for particle transport is absolutely imperative because the particle trajectory decides the residence time of the developing nanostructure in the flame. The residence time plays a huge role in the growth characteristics of the particle. Larger residence times promote sintering and shrink the size of the particle while smaller residence times promote coagulation and also help in selective aggregation of particles which is instrumental in giving various shapes to the developing nanostructures.

Another thing to note in Figure 9-9 is that thermophoretic velocity is independent of particle size in both the flow regimes (free molecular regime and continuum regime). Hence irrespective of their sizes, the nanoparticles come to rest at almost the same stagnation plane.

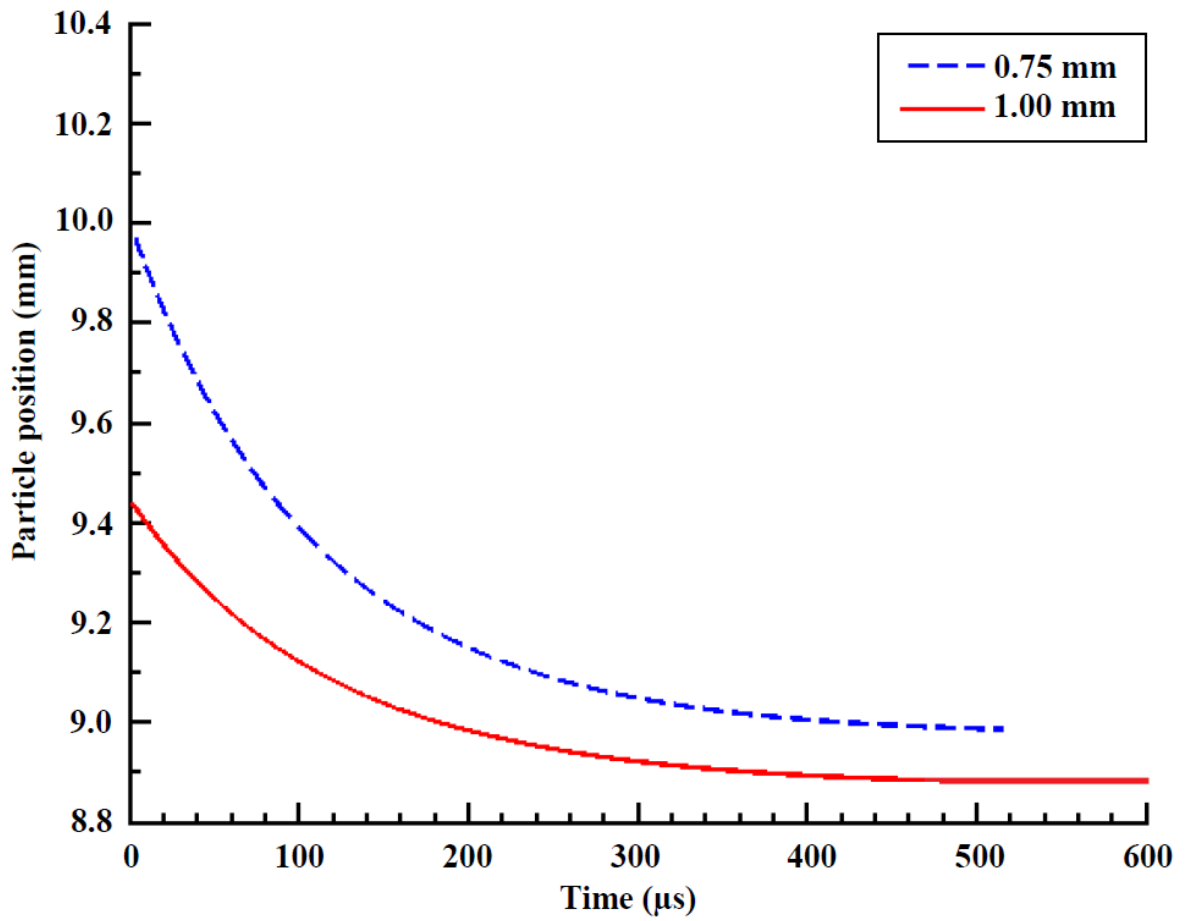


Figure 9-9: Trajectory followed by the nanoparticles from 1.00 mm and 0.75 mm probes during the growth timespan

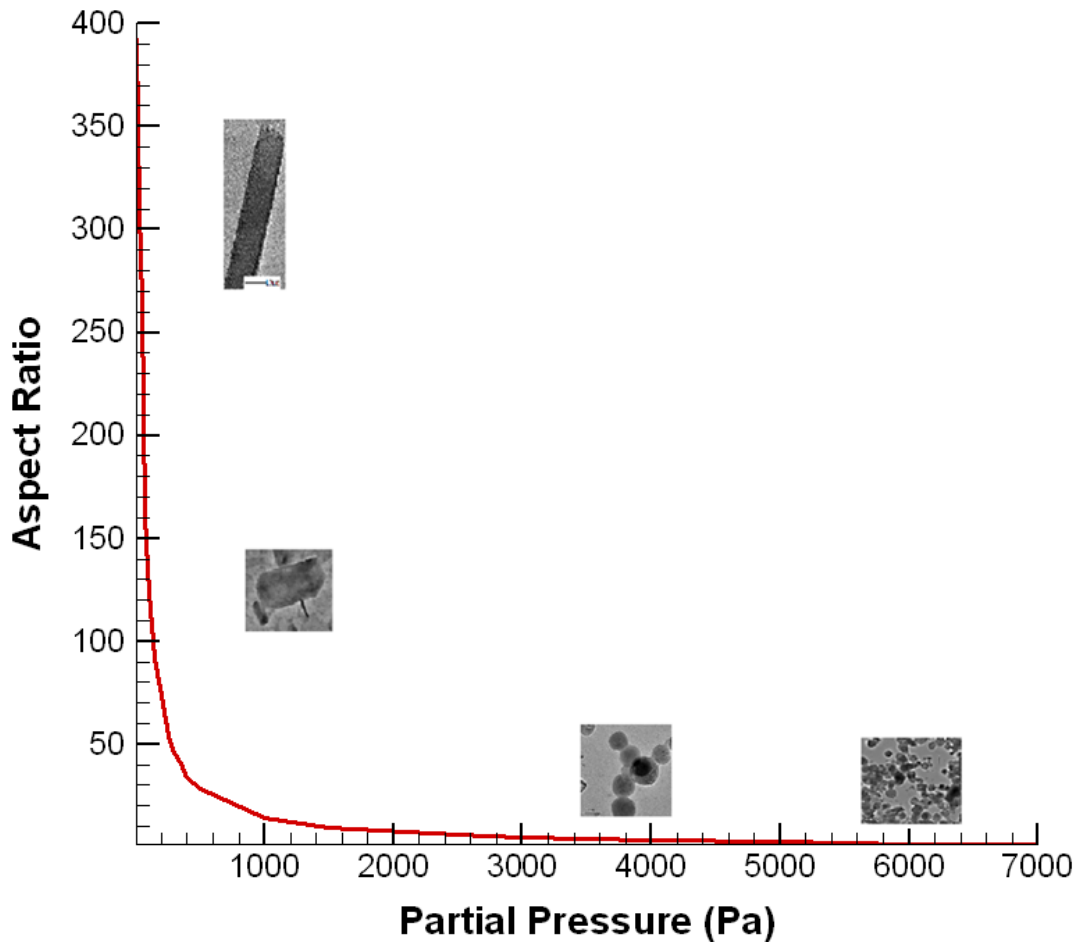


Figure 9-10: Variation of aspect ratio of nanoparticles with monomer partial pressure

Figure 9-10 incorporates the basic crux of the entire numerical model. It shows the decrease in the aspect ratio (length-to-diameter ratio) of the nanorod as the concentration of the precursor atoms is increased. The concentration of the monomer atoms has been represented by their partial pressure. At low pressures the aspect ratio is as high as 300 and exponentially decreases to around 1. The change in aspect ratio shows that the longitudinal and the lateral

growth of the nanostructure is taking place at equal rates and the structure of the nanorod essentially changes from one dimensional to quasi-spherical.

Chapter 10

General Dynamic Equation

Modeling

In the previous chapters attention was given towards the understanding of the growth mechanism of a single molybdenum oxide nanorod by modeling all the relevant processes. However, simply concentrating on a single nanorod will not provide the adequate capabilities for predicting other attributes of nanoparticles. Most of the nanoparticles produced by various processes or found in nature are *polydisperse*, i.e., they are present in variety of sizes. Sometimes characterizing all nanoparticles with one single size satisfies most of the demands but on many occasions a wide range of information about the various attributes of nanoparticles is needed. For instance for pharmaceutical aerosols the particle size and its distribution is of utmost importance.

To make accurate quantitative predictions of nanorod formation and growth other characteristics of the population are important. These include the total numbers, sizes and shapes of the entire range of nanoparticles produced in the flame. The evolution of nanoparticles in flames involves complex processes of nucleation, surface growth and

aggregation which are intricately coupled to the flow field which brings in additional effects of particle transport (Hulburt, et al., 1964) (Pratsinis, 1988). An equation that includes all of these processes is known as the General Dynamic Equation (GDE).

10.1 General Dynamic Equation

To conveniently explain the size distribution of a nanoparticle its frequency distribution $f(l)$ is defined such that the fractions of the nanorods that have lengths between l and $l+dl$ is $f(l)dl$.

The count distribution $n(l)$ is defined such that the number of nanorods between length l and $l+dl$ is $n(l)dl$

$$n(l) = Nf(l) \quad (10.1)$$

where N is the total number of particles in the system.

If we integrate $f(l)dl$ over all particle lengths we obtain the total fraction of nanoparticles in all sizes

$$\int_0^{\infty} f(l)dl = 1 \quad (10.2)$$

Hence on integrating $n(l)dl$ we obtain the total number of particles

$$\int_0^{\infty} n(l)dl = N \quad (10.3)$$

The dynamic behavior and formation of particles in complex flow fields is described by the GDE. It describes the evolution of particle size and distribution of morphology. It is a nonlinear integral-differential equation which can be univariate or multivariate depending on the required details. Also GDEs can be either discrete or continuous as per the scheme of things. The complete evolution of nanoparticles can be obtained by the solution of the GDE. GDEs when represented in the rigorous form give infinite set of nonlinear ordinary differential equations which are impractical to solve. Hence continuous GDEs are a viable option where the particle size is taken as a continuous variable.

The following set of equations suitable to describe the behavior of nanoparticles is the General Dynamic Equation (GDE)

$$\frac{\partial n}{\partial t} + \nabla \cdot nv = \nabla \cdot D \nabla n + \left[\frac{\partial n}{\partial t} \right]_{growth} + \left[\frac{\partial n}{\partial t} \right]_{nucl} - \nabla \cdot cn \quad (10.4)$$

By solving equation (10.4) for different initial and boundary conditions, the size distribution function can be calculated for geometries and flow conditions of practical interest. Various terms that appear in the GDE such as the velocity and diffusivity depend on the gas temperature and pressure. Hence it is important to have independent information on the gas properties as function of time and position. This information can either be obtained through experiments or calculations based on equations of fluid and energy transport.

The GDE is tedious to solve and analytical solutions are not possible for relevant cases. The two most important problems are –

- i. the large size of the system of ordinary differential equations
- ii. the nonlinearity of the equation

Surface reactions and particle inception also cause severe numerical challenges. Hence models have been developed to solve the GDE. Some numerical methods that approximate the size distribution of particles are sectional models, stochastic methods, Galerkin methods and moment methods.

10.1.1 Sectional Methods

Sectional methods have recently become quite popular as a way to solve the GDE. In Sectional methods the entire size spectrum of the nanoparticles is subdivided into smaller bins of different sizes. The solutions are approximated by low order polynomials. For each interval an ordinary differential equation is obtained which is coupled to the neighboring solutions depending on the type of scheme. This scheme has been used by (Hounslow, et al., 1988) (Litster, et al., 1995)

However, there are huge numerical errors in solving for discontinuities and surface growth and the method seems to suffer from the problem of numerical diffusion. To alleviate this problem (Kumar, et al., 1996a) (Kumar, et al., 1996b) came up with a pivot technique combined with a moving grid and a method of characteristics. Sectional methods have also been used in bivariate systems (Koch, et al., 1990). However, the use of these methods has been rather restricted due to their high computational cost.

10.1.2 Monte Carlo Methods

The greatest advantage of Monte Carlo methods is the use of multivariate distributions. These methods are easy to implement and can accommodate fluctuations as well (Kraft, 2005). (Gillespie, 1975) used the Direct Simulation Monte Carlo (DSMC) to solve the GDE. The Monte Carlo algorithm consists of the following steps –

- i. A system of N nanoparticles is assumed.
- ii. Initial state is approximated by these N particles.
- iii. The numerical error in the approximation is determined.
- iv. Probabilities for nucleation, growth and coagulation etc. are calculated and accordingly one of these processes occurs.
- v. The entire system is updated according to the new configuration.

Again, a full scale simulation of aggregation of millions of these nanoparticles has not been feasible due to excessive computing cost.

10.1.3 Moment Methods

Among all the major methods for solving the GDE moment methods are the most efficient. They are superior in terms of cost effectiveness as compared to Sectional methods or Monte Carlo. They provide all the integral quantities such as total number density and volume fraction. There are two approaches that are used most frequently –

- i. method of moments (MOM) (Frenklach, 2002)
- ii. quadrature method of moments (QMOM) (McGraw, 1997)

The QMOM being the most efficient and the most uncomplicated of all has been used in this research. The next sections are dedicated to the implementation of QMOM and the understanding of MOM as it forms the conceptual foundation for QMOM.

10.2 Method of Moments

The Method of Moments (MOM) is a unique way to simulate particle dynamics in a flow. It incorporates all the processes through the GDE. The numerical efficiency of MOM comes from replacing the differential equations of the GDE with corresponding equations of the moments (Frenklach, et al., 1987). It simulates the growth of particles by tracking the lower order moments of their distributions in time to give meaningful information. It has unique advantages in describing the dynamics of nucleation, condensation and evaporation.

The basis of MOM is the *k*th moment of a distribution μ_k given by –

$$\mu_k = \int l^k f(l) dl \quad (10.5)$$

10.2.1 Physical Significance of Moments

The moments of size distributions of *spherical particles* have physical significance

- The zeroth moment μ_0 is the total concentration of particles in the aerosol at a given point and time.

- The first moment μ_1 when divided by the zeroth moment gives number averaged particle diameter
- The second moment is proportional to the surface area of the particles composing the aerosol. The average surface area per particle is obtained by μ_2 / μ_0
- The third moment μ_3 is proportional to the total volume of the particles per unit volume of the gas
- The fourth moment μ_4 is proportional to the total projected area of the material sedimenting from the stationary fluid.
- The fifth moment μ_5 is proportional to the mass flux of the material sedimenting from the fluid.
- The sixth moment μ_6 is proportional to the total light scattering by particles when they are much smaller than the wavelength of the incident light.

Unfortunately for nanorods only μ_0 and μ_1 carry physical significance. The other moments do not have physical significance in the real world, nonetheless, they are required for the computation of the lower moments of the distribution.

10.2.2 General Dynamic Equation for Method of Moments

Applying equation (10.5) to equation (10.4) we get a set of equations governing the monomer as well as the particle behavior (Hulburt, et al., 1964) (McGraw, 1997)

$$\frac{\partial}{\partial t} f_1 = R - S - \nabla \cdot D \nabla f_1 - \nabla \cdot (f_1 v) + \left(\frac{\partial}{\partial t} f_1 \right)_{nucl} - \frac{\pi}{4v_1} \int l^2 \phi(l) f(l) dl \quad (10.6)$$

$$\frac{\partial}{\partial t} \mu_0 = -\nabla \cdot D \nabla \mu_0 - \nabla \cdot (\mu_0 v) + \int J(l) dl \quad (10.7)$$

$$\frac{\partial}{\partial t} \mu_k = -\nabla \cdot D \nabla \mu_k - \nabla \cdot (\mu_k v) + \int l^k J(l) dl + k \int l^{k-1} \phi(l) f(l) dl \quad (10.8)$$

Equation (10.6) gives the rate of change of monomer. R and S are source and sink rates respectively. D is the diffusivity and v is the velocity of flow. $\phi(l)$ is the nanorod growth law, $\phi(l) = dl/dt$. The last term in equation (10.6) denotes the loss of monomers to the growth of the nanorod. Equations (10.7) and (10.8) provide the evolution of zeroth and k th moments of the nanorod growth.

10.2.3 Restrictions to Method of Moments

Equations (10.6), (10.7) and (10.8) cannot be solved directly since they involve integration over the distribution function $f(l)$ which is unknown. MOM accomplishes this task due to the availability of certain special cases where the growth law $\phi(l)$ forms closed set of equations in terms of moments of $f(l)$. The necessary condition for MOM to for a closed set of equations is –

$$\phi(l) = a + bl$$

where a and b are constants. However, there are umpteen practical cases where closure of the equations is not possible and these closure requirements pose serious restrictions to the

applicability of MOM. The simplest way to circumvent this problem is to presume the functional form of the particle size distribution function (Lee, 1983) (Whitby, 1981) (Peterson, et al., 1978). But, again there are many important applications where the particle size distribution is unknown apriori.

10.2.4 Method of Moments with Interpolative Closure

MOM shows deficiencies where the particle size distribution is not known apriori. For this reason a new method was developed called Method of Moments with Interpolative Closure (MOMIC). The central theme of MOMIC is to attain closure through interpolation among instantaneous values of computed moments. In most cases this is achieved through logarithmic polynomial interpolation. MOMIC has been used to describe univariate distribution of soot particles in the free molecular regime (Frenklach, et al., 1994). The authors in this work have solved two sets of moments simultaneously, one for the size distribution of PAH and the other for the size distribution of soot particles. For unimodal particle size distributions with no surface reactions MOMIC shows promising results with high accuracy and speed (Balthasar, et al., 2003). However, MOMIC seems inadequate to represent the bimodal nature of soot formation. The first mode corresponds to the inception and nucleation of soot particles whereas the second mode represents the growth of large particles (Zhao, et al., 2005). Later it was also observed (Mueller, et al., 2009) that MOMIC entirely missed the effect of the smaller particles. Due to this some other closure schemes

were proposed for MOMIC (Frenklach, 2002) (Frenklach, et al., 1987) but they were not very easily capable of being generalized to multivariate systems (Mueller, et al., 2009)

10.3 Quadrature Method of Moments

As seen above MOM has severe complications in achieving closure of the moment equations which severely restricts its application. In this light the Quadrature Method of Moments (QMOM) was introduced (McGraw, 1997). QMOM also includes tracking the changes in moments of the particle size distribution through time but the requirement of exact closure is replaced by an approximate closure condition. In QMOM the particle size distribution is approximated through a combination of weighted multi-dimensional Dirac delta function. The abscissas and weights are then chosen to satisfy the moment equations (Balthasar, et al., 2003). The MOM is also obtained as a special case of the QMOM if the growth law is used as stated above. (Rosner, et al., 2003) simulated a univariate and bivariate population balances of alumina nanoparticle evolution with coagulation and sintering, using the QMOM. Later they also used the Monte Carlo approach to validate their results. QMOM has also been extensively tested and validated by other researchers (Barret, et al., 1998) (Marchisio, et al., 2003) (Marchisio, et al., 2003)

10.3.1 Quadrature-Based Closure

The growth term in equation (10.8) is the subject of focus for the QMOM since it involves integration over an unknown particle size distribution function $f(l)$. A much less restrictive closure method is utilized by approximating the growth integral using n -point Gaussian quadrature (Lanczos, 1988). To achieve this the abscissas r_i and weights w_i are specified in terms of the lower order moments of $f(l)$. For n -point quadrature the moments are represented as -

$$\mu_k = \int l^k f(l) dl = \sum_{i=1}^n l_i^k w_i \quad (10.9)$$

where $k = 0$ to $2n-1$

This ensures that the weights and abscissas remain independent of the distribution function $f(l)$, except through its lower order moments. Hence the growth law can now be written as

$$k \int l^{k-1} \phi(l) f(l) dl \cong k \sum_{i=1}^n l_i^{k-1} \phi(l_i) w_i \quad (10.10)$$

Substitution of equation (10.10) into equation (10.8) provides approximate closure for the growth term as the equality in equation (10.10) is approximate. These equations are close since the moments are no longer dependent on the distribution function. Instead they depend only on the abscissas and weights calculated which are carried forward in time as the moments themselves are advanced. Hence, the premise of QMOM is to calculate the growth contribution to the moments in an approximate fashion.

As the moments progress, QMOM demands the search for corresponding abscissas and weights. This rapid conversion of moments to abscissas and weights is provided by the Product Difference Algorithm (Gordon, 1968) given in Section 10.3.2

10.3.2 Product Difference Algorithm

The most efficient approach is to use the moments to construct a tridiagonal Jacobi matrix from which the weights and abscissas can be obtained. The entire process consists of two steps. First, a 3 x 3 symmetrical tridiagonal matrix is formulated where the diagonal and off-diagonal elements are derived from the moments using the Product Difference algorithm. Second, the matrix is diagonalized to obtain three abscissas and three weights (McGraw, 1997) (Gordon, 1968).

The Product Difference algorithm begins with setting up a triangular array of elements

$$P(i, j)$$

$$P(i, 1) = \delta_{i,1}$$

where $\delta_{i,j} = 0$ for $i \neq j$ and $\delta_{i,j} = 1$ for $i = j$

$$P(i, 2) = (-1)^{i-1} \mu_{i-1}$$

The remaining elements are found by the general formula –

$$P(i, j) = P(i-1, j-1)P(i+1, j-2) - P(i-1, j-2)P(i+1, j-1)$$

After obtaining the matrix P we generate a new vector –

$$\alpha(1) = 0$$

$$\alpha(j) = P(1, j+1) / [P(1, j)P(1, j-1)]$$

Finally the elements of the Jacobian are obtained –

$$a_j = \alpha(2j) + \alpha(2j-1)$$

$$b_j = \alpha(2j+1)\alpha(2j)$$

The Jacobian has the form

$$J = \begin{bmatrix} a_1 & b_1 & \\ b_1 & a_2 & b_2 \\ & b_2 & a_3 \end{bmatrix}$$

The eigenvalues of J are the abscissas l_j whereas weights w_j are calculated in terms of the corresponding eigenvectors (v) (Press, et al., 1990)–

$$w_j = \mu_0 v_{j,1}^2$$

10.3.3 Verification of the Quadrature Method of Moments Algorithm

For the purpose of verification the approach followed by (McGraw, 1997) has been followed.

A univariate initial distribution having the Khrigian-Mazin (KM) cloud drop size distribution (Pruppacher, et al., 1980) has been assumed

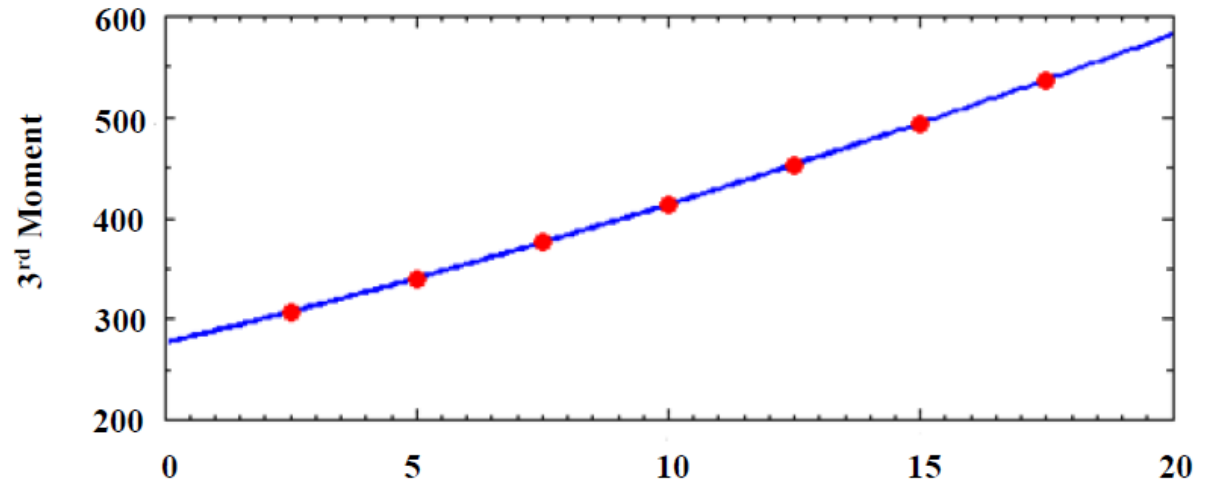
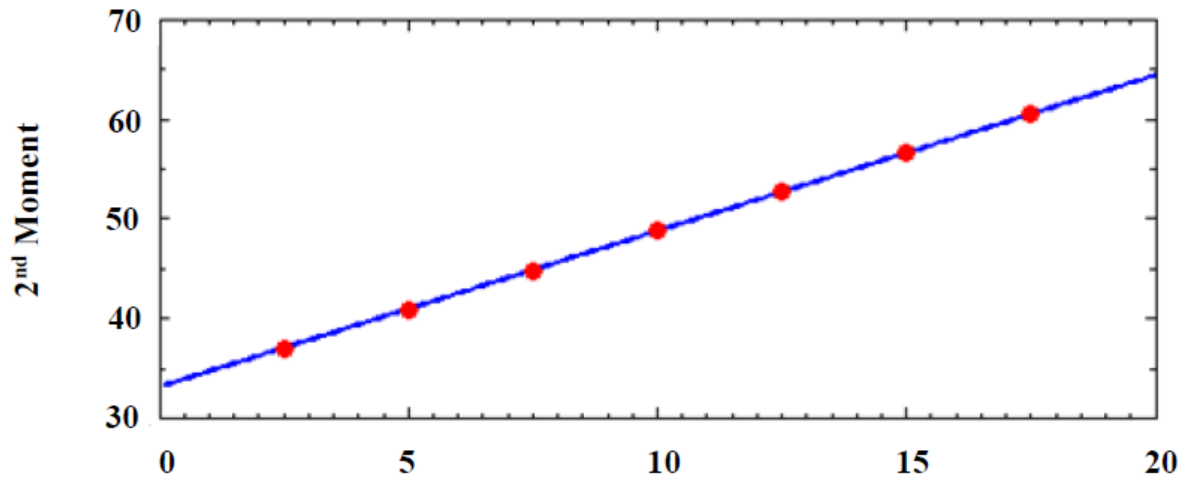
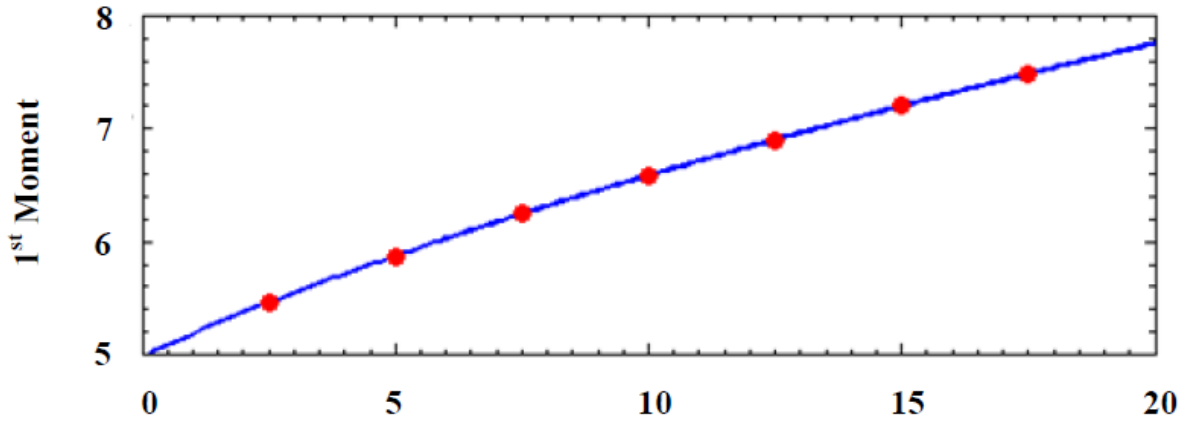
$$f(r) = ar^2 \exp(-br)$$

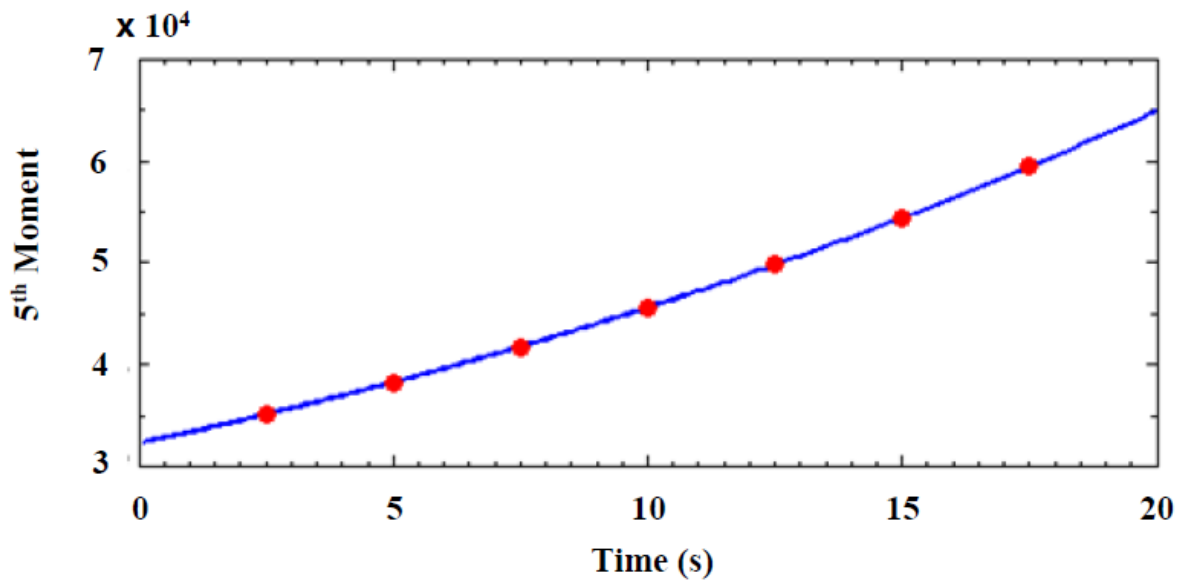
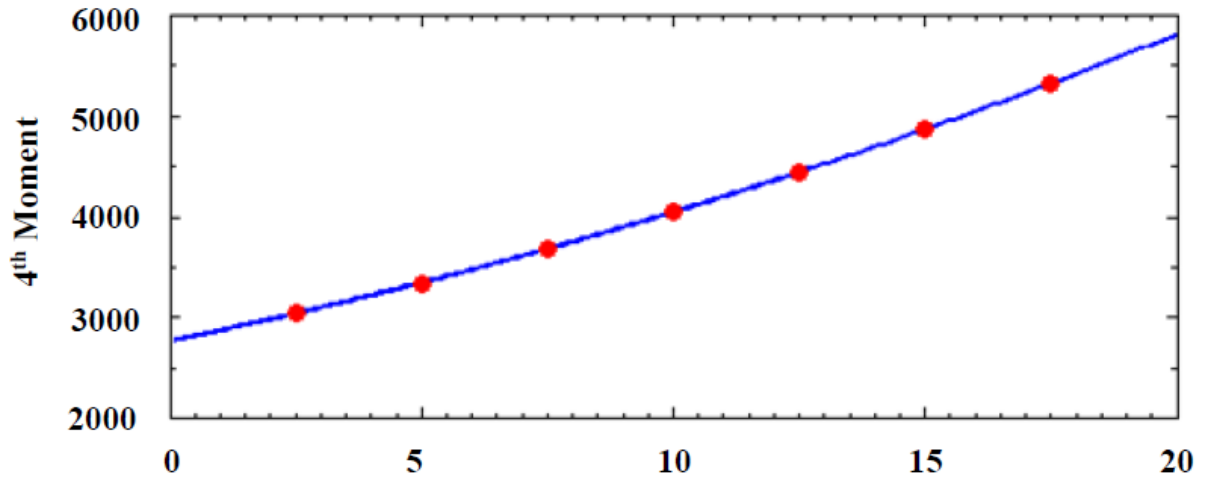
where r is the particle size, $a = 0.108 \mu m^{-3} cm^{-3}$ and $b = 0.6 \mu m^{-1}$ with an initial particle radius of $5 \mu m$.

The growth law is $\phi = \frac{k_2}{r}$ with $k_2 = 0.78 \mu m^2 / s$

The five moments μ_1 to μ_5 are shown here along with the analytical solution. The plots also match perfectly with the ones shown by (McGraw, 1997)

Figure 10-1: Solution of the Khrgian-Mazin size distribution, QMOM (solid), analytical
(dots)





A second sanity check is done by applying the Product-Difference algorithm to obtain the abscissas and weights and later to substitute them back into equation (10.9) to recover the moments.

In Table 10-1 the initial values of the normalized moments and their respective abscissas and weights are given.

Table 10-1: Inversion of initial moments for Fig. 10-1

n	$\mu_n(t=0)$	r_n	w_n
0	1.0		
1	5.0	15.2853	0.0283
2	33.33	7.1862	0.4528
3	277.78	2.5291	0.5187
4	2777.78		
5	32407.4		

The code for Product-Difference algorithm has been given in Appendix B.

Figure 10-2 illustrates the procedure for Quadrature Method of Moments.

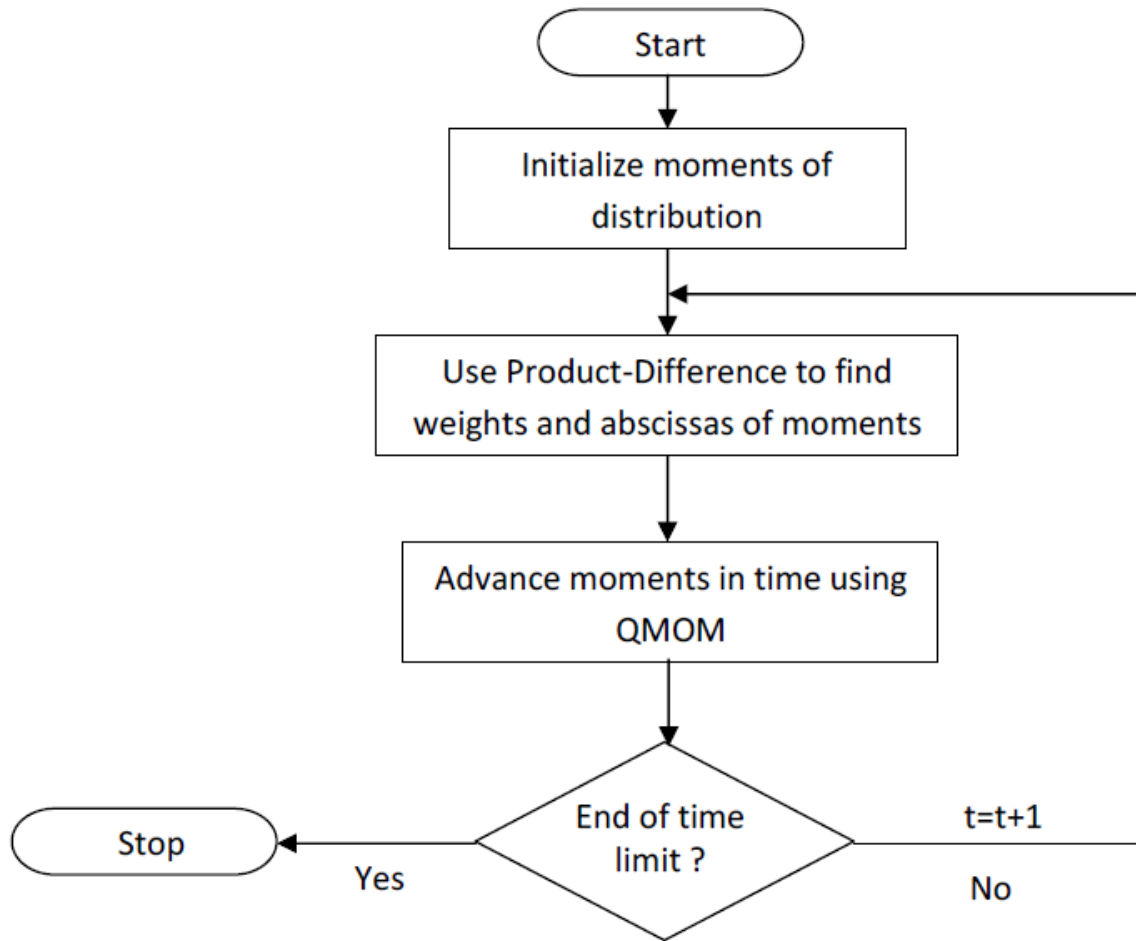


Figure 10-2: Procedure for Quadrature Method of Moments

10.4 Quadrature Method of Moments Applied to Nanorod

Synthesis

QMOM provides for tracking of the nanoparticle evolution by following the changes in the moments of the particle size distribution function. The advancement of these moments

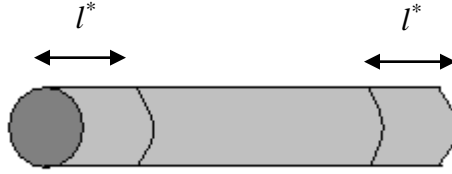
requires the closed form solution of the GDE which is provided by the abscissas and weights calculated. The GDE tracks the temporal evolution of the moments by including the effects of transport, nucleation and growth of the particles, each of which has a separate term to be modeled. The GDE solved here is *univariate in length* since the characteristic dimension of nanorods is their length. This section provides the details for modeling each term in the GDE using the concepts of QMOM.

10.4.1 Growth

The GDE in the analysis presented here is assumed to be univariate in length and the diameter of the nanorods has been taken as constant. The increase in nanorod length is dictated by two sources –

- i. Direct impingement
- ii. Diffusion of atoms from side surfaces

The atoms have a characteristic average displacement (l^*) on the nanorod surface given by equation (7.11), before they escape into the atmosphere. The growth follows one pattern for the nanorods which are smaller than this characteristic distance and another when they are longer than this distance. Accordingly the analysis of the growth term changes for the two cases.



Nanorod length greater than average displacement for atoms ($l > l^*$)

$$\frac{dV}{dt} = \frac{dl}{dt} \pi r^2 \quad (10.11)$$

where V is the volume of the nanorod. l and r are the length and radius respectively.

Flux of atoms from direct impingement –

$$j = \frac{P - P_\infty}{\sqrt{2\pi mkT}}$$

Increase in length due to attachment of atoms from direct impingement –

$$2\pi r^2 ja^3 \quad (10.12)$$

here a is the dimension of a single monomer atom

Since only the migrating atoms within l^* on the nanorod surface are only able to reach the ends therefore the increase in the length of the nanorod due to this diffusion flux –

$$2 \cdot 2\pi r l^* ja^3 \beta \quad (10.13)$$

β is the fraction of the incident atoms that migrate and reach the ends of the nanorod.

From equation (10.11), (10.12) and (10.13) we get –

$$\frac{dl}{dt} = a^3 \left(2j + \frac{4l^*}{r} \beta j \right) \quad (10.14)$$

Now the growth law $\phi = \frac{dl}{dt}$

Assuming the incident flux of atoms j to be constant for a given location, all the other terms on the right side of equation (10.14) are constants. Therefore ϕ in this case is constant.

Nanorod length smaller than average displacement for atoms ($l < l^*$)

$$\frac{dV}{dt} = \frac{dl}{dt} \pi r^2 \quad (10.15)$$

Increase in length due to attachment of atoms from direct impingement –

$$2\pi r^2 ja^3 \quad (10.16)$$

Since now all the migrating atoms on the nanorod surface of length l are capable of reaching the ends therefore the increase in the length of the nanorod due to this diffusion flux –

$$2 \cdot 2\pi r l \cdot ja^3 \beta \quad (10.17)$$

From equations (10.15), (10.16) and (10.17)

$$\phi = \frac{dl}{dt} = a^3 \left(2j + \frac{4l}{r} \beta j \right) \quad (10.18)$$

Assuming the incident flux of atoms j to be constant for a given location, ϕ varies linearly with the increasing length of the nanorod.

10.4.2 Nucleation

Nucleation affects the particle size distribution by creating new centers of aggregation for the nanorods. It also consumes a sizable part of the monomers thus depleting their supply to the

growing nanoparticles. In the present model nucleation has been assumed to cease after its maximum rate is reached. When the nucleation stops the aggregation of monomers starts on the formed nuclei which eventually grow into mature nanorods. Thus the contribution of nucleation in tracking the moments of the nanoparticle distribution is only present during the nucleation phase and is absent during the growth phase. The equation for tracking the concentration of monomers also takes nucleation into account.

10.4.3 Particle Transport

Historically the effect of diffusion has been neglected when solving the moment equations (Kraft, 2005). For steady flames the space coordinate can be transformed into the time coordinate by following a Lagrangian specification rather than an Eulerian perspective. If the effects of diffusion are to be included then additional equations for moments are to be solved.

10.4.4 Final Equations and Procedure for Quadrature Method of Moments

As explained above there are two sets of equations, one for the nucleation phase and the other for the growth phase

Nucleation phase

For nucleation only the birth term remains and the growth term vanishes. Thus the moment equation becomes

$$\frac{\partial \mu_0}{\partial t} = J \cdot \delta(x - x_o) \quad (10.19)$$

where J is the nucleation rate and $\delta(x - x_o)$ is the Dirac delta function centered at the size of the nuclei x_o .

$$\Delta \mu_k = \begin{cases} J \cdot \Delta t, k = 0 \\ 0, k \neq 0 \end{cases}$$

This shows that the zeroth moment that is equal to the total number of particles increases linearly with time whereas the higher order moments are zero at all times since no growth takes place.

Growth phase

As mentioned in the previous section, nucleation is assumed to cease after it attains its peak value. Thereafter the growth phase begins. For the growth phase we have -

$$\frac{\partial}{\partial t} f_1 = \left(\frac{\partial}{\partial t} f_1 \right)_{nucl} - \frac{\pi}{4\nu_1} \int l^2 \phi(l) f(l) dl \quad (10.20)$$

$$\frac{\partial}{\partial t} \mu_0 = 0 \quad (10.21)$$

$$\frac{\partial}{\partial t} \mu_k = k \int l^{k-1} \phi(l) f(l) dl \quad (10.22)$$

Initial conditions:

μ_0 is the total number of nuclei present after nucleation phase ends

$\mu_k = 0$, for $k = 1, 2, 3, 4, 5$

Solving equations (10.20) to (10.22) gives us the complete description of the monomer concentration as well as the nanorod growth dynamics with time.

10.5 Results of Quadrature Method of Moments applied to

Nanorod synthesis

For the nucleation phase equation (10.19) has been solved. The result obtained is shown in

Figure 10-3

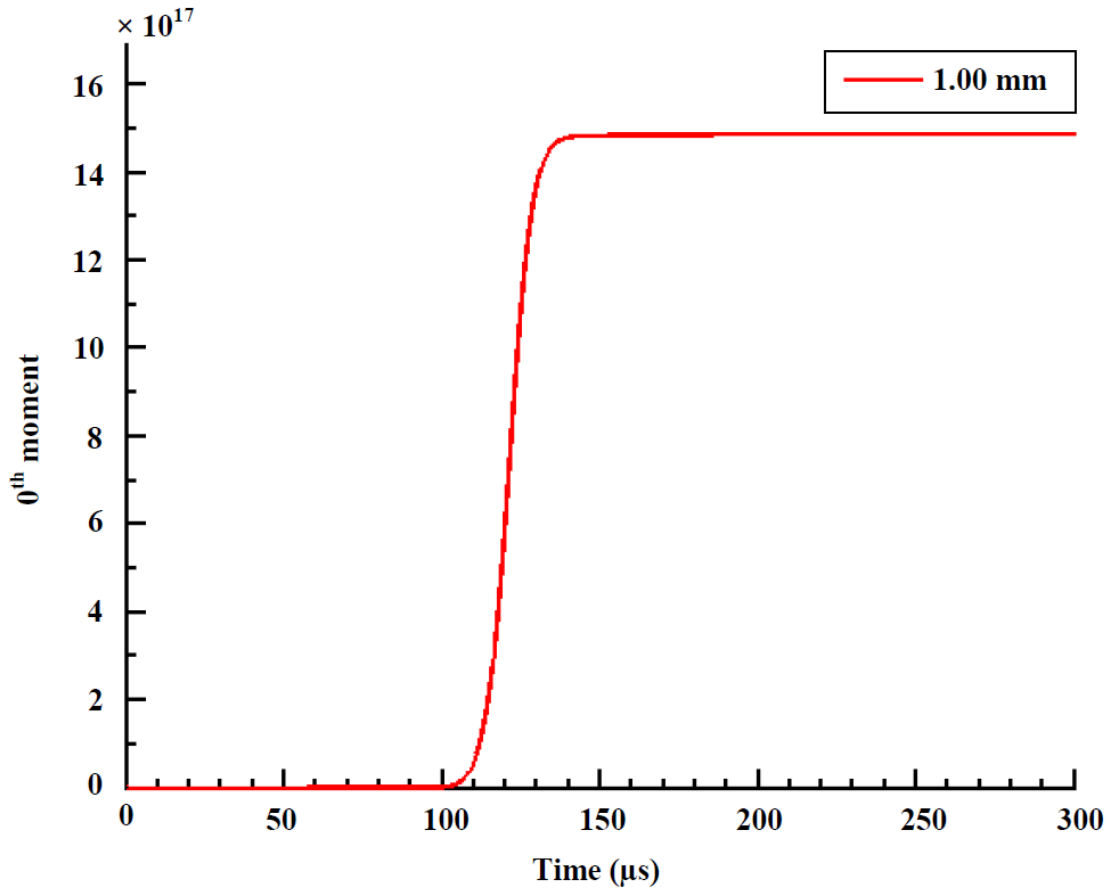


Figure 10-3: Variation of 0th moment during nucleation with nucleation timespan

As discussed in Section 10.4.4 during nucleation only the 0th moment changes with all the other moments staying constant due to absence of growth. In the physical sense the 0th moment represents the number density of particles. Hence Figure 10-3 represents the total number of nuclei formed during the nucleation phase and also gives the total number of nanorods that will grow in the flame volume as no new particles are assumed to nucleate during the growth phase. Initially there is no nucleation but later on finding suitable

conditions nucleation starts and the concentration of nuclei starts to build up until it stagnates after the peak nucleation has been achieved. Figure 10-3 follows the dynamics of Figure 9-3.

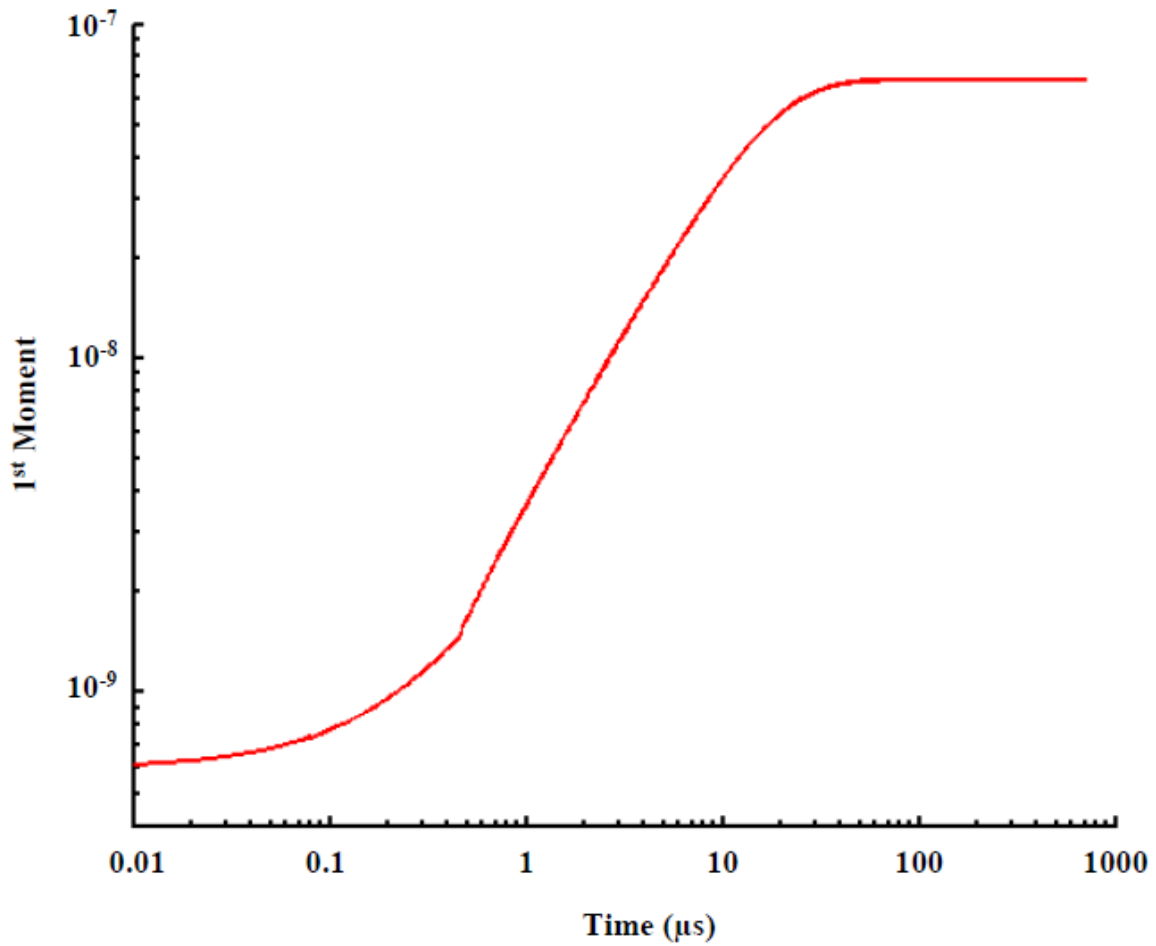


Figure 10-4: Variation of 1st moment during growth with growth timespan

The growth phase starts after the nucleation phase is assumed to achieve completion. For studying the evolution of the particle size distribution a normal distribution is assumed at the

onset. Since nanorod synthesis begins from the nucleus stage the critical size of the stable nuclei during peak nucleation has been chosen as the mean and the difference in the size of the nuclei at the beginning and end of nucleation forms the standard deviation. Figure 10-4 shows the variation of the 1st moment of the nanorod size distribution with time. Physically the 1st moment of a size distribution gives the average length of the nanorods in the flame volume. The average length of nanorods as predicted by QMOM is 70 nm. As the nanorods grow in size the moment grows as well. It is noteworthy that the trend shown by the 1st moment follows that of the growth of a single nanorod as shown in Figure 9-6. Unlike spherical particles higher moments in nanorods do not carry any physical significance. However, they are needed to compute the lower moments of the distribution. Hence they have been presented in Figure 10-5.

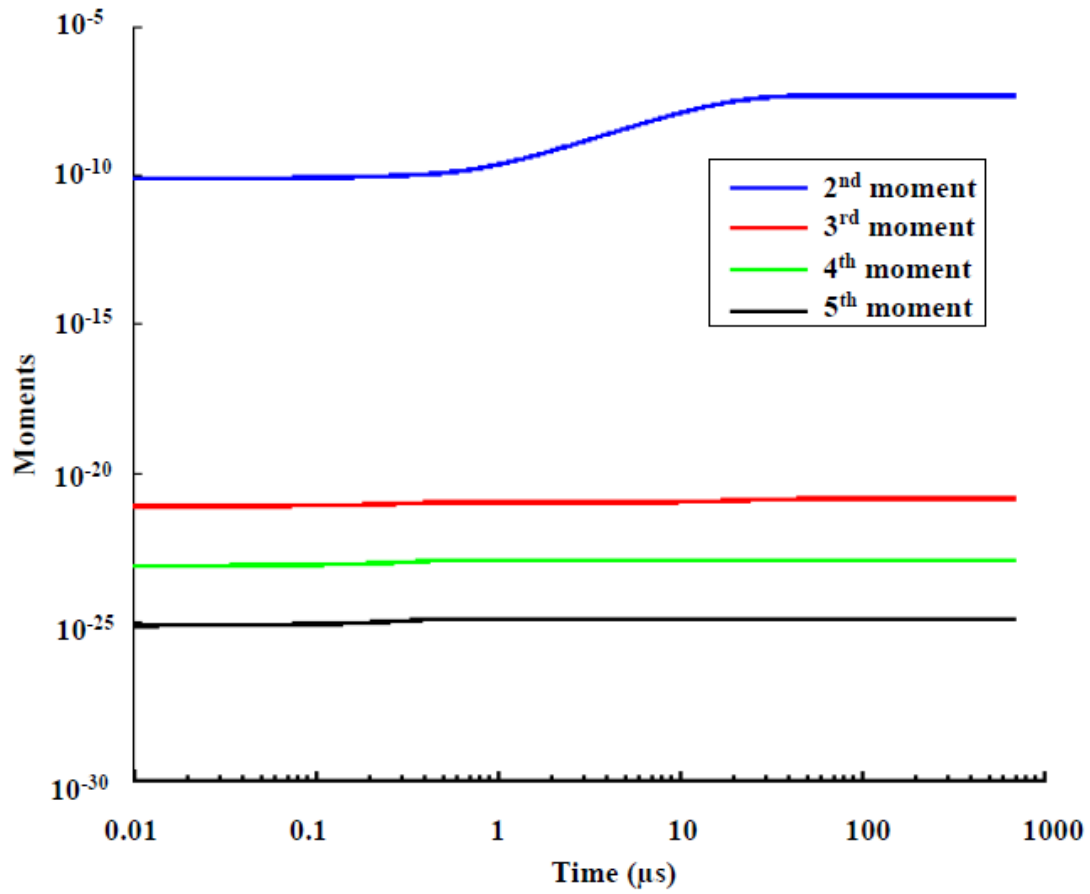


Figure 10-5: Variation of higher moments for the nanorod size distribution with growth timespan

Chapter 11

Conclusions

The thesis proposed and analyzed a numerical model, the first of its kind, to simulate the synthesis of one-dimensional nanostructures in an opposed flow flame environment. This effort was principally aimed at gaining a better insight into the processes that occur in a combustion synthesis procedure and the way flames affect every aspect of particle synthesis. This would help in refining the control parameters of the processes and achieve desired end products.

The entire scheme of the model was presented and validated using the experimental results of the *Flame Gradient Method*. The model includes mathematical simulation of every stage of nanoparticle development including monomer formation, nucleation, nanorod growth and particle transport through the flame. Complex processes occurring on an individual nanoparticle surface were tracked and simultaneous coupling was implemented between the flame and the particle growth model to enable detailed examination of the effect of flow processes. The results showed a remarkable agreement with the experiments. The numerical model was successfully able to predict the growth patterns of the nanorod along with their trajectory. It proved that the region of the flame for the actual longitudinal growth is rather

thin where most of the building material is consumed. A significant accomplishment of the model was the ability to capture the decrease in the aspect ratio of the nanoparticles with increasing monomer concentration i.e. decreasing molybdenum probe diameter. The model demonstrated that low supersaturation ratio is a requirement for the growth of one-dimensional nanostructures and also quantified its limits.

Further, to understand the effect of conditions on the growth characteristics of all the nanoparticles in the flame volume moment methods were implemented to track the particle size distribution functions with time. This gave a clear picture of the collective processes rather than the detailed processes going on the surface of individual particles.

Overall, this work established the control parameters for one-dimensional nanoparticle growth in flames and how manipulating them could enable us to obtain nanoparticles of all aspect ratios and group characteristics.

Future work can involve applying this theory to turbulent flame simulations to make this synthesis process scalable for industrial use. Monte Carlo or molecular dynamic simulations could be performed to gain even more detailed insight as well as using more complex nucleation theories.

REFERENCES

- Anderson Jr. J. D.** Computational Fluid Dynamics: The Basics with Application [Book]. - Singapore : McGraw-Hill Inc., 1995.
- Anisimov M.P.** Nucleation: Theory and Experiment [Journal] // Rus. Chem. Rev.. - 2003. - Vol. 72. - p. 591.
- Bakrania S.D., Perez C. and Wooldridge M.S.** Methane Assisted Combustion Synthesis of Noncomposite Tin Dioxide Materials [Journal] // Proc. Comb. Inst.. - 2007. - Vol. 31. - p. 1797.
- Balthasar M and Kraft M.** A Stochastic Approach to Calculate the Particle Size Distribution Function of Soot Particles in Laminar Premixed Flames [Journal] // Comb. Flame.. - 2003. - Vol. 133. - p. 289.
- Barnard A. S. and Curtiss L. A.** Computational Nano-Morphology: Modeling Shape as well as Size [Journal] // Rev. Adv. Mater. Sci.. - 2005. - Vol. 10. - p. 105.
- Barret J.C. and Webb N.A.** A Comparison of Some Approximate Methods for Solving the Aerosol General Dynamic Equation [Journal] // J. Aerosol Sci.. - 1998. - Vol. 29. - p. 31.
- Bartlett E.S. and Williams D.N.** The Oxidation Rate of Molybdenum in Air [Journal] // Trans. AIME. - 1958. - Vol. 212. - p. 280.
- Bartlett E.S. and Williams D.N.** The Oxidation Rate of Molybdenum in Air [Journal] // Trans. Met. Soc. AIME. - 1958. - Vol. 212. - p. 280.
- Beck D.D. and Siegel R.W.** The Dissociative Adsorption of Hydrogen Sulfide over Nanophase Titanium Dioxide [Journal]. - 1992. - Vol. 7. - p. 2840.

- Beltrame Andrea Luigi** Study on Oxygen Enriched Laminar Counterflow Diffusion Flames [Report] / Mechanical Engineering ; University of Illinois . - Chicago : [s.n.], 2000.
- Blakely J.M. and Jackson K.A.** Growth of Crystal Whiskers [Journal] // J. Chem. Phys.. - 1962. - Vol. 37. - p. 428.
- Braun J. H.** Titanium dioxide: A Review [Journal] // J. Coat. Tech.. - 1997. - Vol. 69. - p. 59.
- Burns R.P. [et al.]** Mass Spectrometric Investigation of the Sublimation of Molybdenum Dioxide [Journal] // J. Chem. Phys.. - 1960. - Vol. 32. - p. 1363.
- Burton W.K., Cabrera N. and Frank F.C.** The growth of crystals and the equilibrium structure of their surfaces [Journal] // Philos. Trans. Roy. Soc. A. - 1951. - Vol. 243. - p. 293.
- Cao G.** Nanostructures and Nanomaterials [Book]. - [s.l.] : World Scientific Publishing Co., 2004. - Vol. 1.
- Cengel Yunus A.** Heat Transfer [Book]. - New Delhi : Tata McGraw-Hill, 2003. - 2nd : Vol. 1.
- Chernov A.A.** Modern Crystallography III [Book]. - Tokyo : Springer-Verlag, 1984.
- Christian J. W.** The Theory of Transformation in Metals and Alloys [Book]. - [s.l.] : Newnes, 2002. - Vol. 1.
- Chung S. L. and Katz J. L.** The Counter Flow Diffusion Flame Burner: A New Tool for the Study of the Nucleation of Refractory Compounds [Journal] // Combust. Flame. - 1985. - Vol. 61. - p. 271.
- Cui Y. [et al.]** Nanowire Nanosensors for Highly Sensitive and Selective Detection of Biological and Chemical Species [Journal] // Science. - 2001. - Vol. 293. - p. 1289.

Cunningham E. On the Viscosity of Steady Fall of Spherical Particles through Fluid Medium [Journal] // Proc. Roy. Soc. A. - 1910. - Vol. 83. - p. 357.

Derjaguin B.V. and Bakanov S.P. The motion of a small particle in a non-uniform gas mixture [Journal] // Discuss. Faraday Soc.. - 1960. - Vol. 30. - p. 130.

Derjaguin B.V. and Yalamov Yu Theory of thermophoresis of large aerosol particles [Journal] // J. Col. Sci.. - 1965. - Vol. 20. - p. 555.

Desai M. Gas Phase and Solid Support Flame Synthesis of Transition Metal Oxide Structures in a Counter-Flow Diffusion Flame [Report] / University of Oklahoma. - 2010.

Dillmann A. and Meier G.E.A. A Refined Droplet Approach to the Problem of Homogeneous Nucleation from the Vapor Phase [Journal] // J. Chem. Phys.. - 1991. - Vol. 94. - p. 2872.

Dillmann A. and Meier G.E.A. Homogeneous Nucleation of Supersaturated Vapor [Journal] // Chem. Phys. Lett.. - 1989. - Vol. 1. - p. 160.

Douglass D.L. Oxidation of Metals and Alloys [Book]. - [s.l.] : American Society for Metals, 1970.

Eckert E.R.G. Heat and Mass Transfer [Book]. - [s.l.] : McGraw Hill Co., 1959. - 2nd.

Figgis B. N., Lewis J. and Wilkins R. G. The Magnetochemistry of Complex Compounds. Modern Coordination Chemistry [Book]. - New York : Wiley Interscience, 1960. - Vol. 1.

Ford I.J. Modification of the Dillmann - Meier Theory of Homogeneous Nucleation [Journal] // J. Chem. Phys.. - 1993. - Vol. 1. - p. 99.

Frank F.C. The Influence of Dislocations on Crystal Growth [Journal] // Discuss. Faraday Soc.. - 1949. - Vol. 5. - p. 48.

- Frenklach M. and Harris S.J.** Aerosol dynamics modeling using the method of moments [Journal] // J. Coll. Inter. Sci.. - 1987. - Vol. 118. - p. 252.
- Frenklach M. and Wang H.** Detailed mechanism and modeling of soot particle formation [Journal] // Soot Form. Comb.. - 1994. - p. 165.
- Frenklach M.** Method of Moments with Interpolative Closure [Journal] // Chem. Eng. Sci.. - 2002. - Vol. 57. - p. 2229.
- Friedlander S.K.** Smoke, Dust and Haze [Book]. - New York : Oxford University Press, 2000. - 2nd.
- Gibbs J.W.** The Collected Work [Book]. - New York : Longmans Green, 1928.
- Gillespie D.T.** An Exact Method for Numerically Simulating the Stochastic Coalescence Process in a Cloud [Journal] // J. Atm. Sci.. - 1975. - Vol. 32. - p. 1977.
- Goodwin D.** Cantera. - Pasadena : Caltech, 2009.
- Gorbounova K.M. and Arslambekov V.A.** [Journal] // Reunion De La Societe De Chimie Physique. - Paris : [s.n.], 1956.
- Gordon R.G.** Error Bounds in Equilibrium Statistical Mechanics [Journal] // J. Math. Phys.. - 1968. - Vol. 9. - p. 655.
- Greer J.F.** The TWOPNT Program for Boundary Value Problems, SAND91-8238 [Report]. - [s.l.] : Sandia National Lab., 1992.
- Gretz R.D.** Nucleation of Zinc Crystals in Multilayer Adsorption [Journal] // Phys. Stat. Sol.. - 1967. - Vol. 23. - p. 453.
- Gulbransen E. A., Andrew K. F. and Brassart F. A.** Oxidation of Molybdenum [Journal] // Electrochem. Soc.. - 1963. - Vol. 110. - pp. 952-959.

- He T. and Jiannian Y.** Photochromism of Molybdenum Oxide. [Journal] // J. Photochem. Photobio.. - 2003. - Vol. 2. - p. 125.
- Height M. [et al.]** Nanorods of ZnO made by Flame Spray Pyrolysis [Journal] // Chem. Mater.. - 2006. - Vol. 18. - p. 572.
- Herring C.** Some Theorems on the Free Energies of Crystal Surfaces [Journal] // Phys. Rev.. - 1951. - Vol. 82. - p. 87.
- Hirschfelder J.O., Curtiss C.F. and Bird R.B.** Molecular Theory of Gases and Liquids [Book]. - New York : John Wiley and Sons, Inc, 1954.
- Hong Y.C., Kim J.H. and Uhm H.S.** ZnO Nanorods Synthesised by Self-Catalytic Method of Metal in Atmospheric Microwave Plasma Torch Flame [Journal] // Jap. J. Appl. Phys. I. - 2006. - Vol. 45. - p. 5940.
- Hounslow M.J., Ryall R.L. and Marshall V.R.** A Descritized Polpulation Balance for Nucleation, Growth and Aggregation [Journal] // A.I.Ch.E.. - 1988. - Vol. 34. - p. 1821.
- Hulburt H.M. and Katz S.** Some Problems in Particle Technology: A Statistical Mechanical Formulation [Journal] // Chem. Eng. Sci.. - 1964. - Vol. 19. - p. 555.
- Hung C.H., Krasnopoler M.J. and Katz J.L.** Condensation of a Supersaturated Vapor VIII The Homogeneous Nucleation of nNonane [Journal] // J. Chem. Phys.. - 1989. - Vol. 90. - p. 1856.
- Job G. and Herrmann F.** Chemical Potential - a Quality in Search of Recognition [Journal] // Eur. J. Phys.. - 2006. - Vol. 27. - p. 353.

Johannessen T., Pratsinis S. E. and Livbjerg H. Computational Fluid-Particle Dynamics for the Flame Synthesis of Alumina Particles [Journal] // Chem. Eng. Sci.. - 2000. - Vol. 55. - p. 177.

Johnson C. Streamline Diffusion Methods for Problems in Fluid Mechanics [Journal] // Finite Elements in Fluids. - 1985. - Vol. 6. - p. 251.

Jones E.S. [et al.] The Oxidation of Molybdenum [Journal] // Corrosion. - 1958. - Vol. 14.

Kammler H. K., Madler L. and Pratsinis S. E. Flame Synthesis of Nanoparticles [Journal] // Chem. Eng. Technol.. - 2001. - Vol. 24. - p. 583.

Karch J. and Birringer R. Nanocrystalline Ceramics: Possible Candidates for Net-Shape Forming [Journal] // Ceramics Intl.. - 1990. - Vol. 16. - p. 291.

Karch J., Birringer R. and Gleiter H. Ceramics Ductile at Low Temperature [Journal] // Nature. - 1987. - Vol. 330. - p. 556.

Katz J.L. The Critical Supersaturations Predicted by Nucleation Theory [Journal] // J. Stat. Phys.. - 1970. - Vol. 2. - p. 2.

Kee R.J. [et al.] A Fortran Computer Code Package for the Evaluation of Gas phase, Multicomponent Transport Properties [Report]. - [s.l.] : Sandia, 1986.

Kee R.J., Miller J.A. and Evans G.H. A Computational Model of the Structure and Extinction of Strained, Opposed flow, Premixed Methane-Air Flames [Conference] // Twenty-Second Symposium (International) on Combustion. - 1988. - pp. 1479 - 1494.

Kim J.I. [et al.] Numerical and Experimental Study on Silica Generating Counterflow Diffusion Flames [Journal] // Int. J. Heat Mass Trans.. - 2005. - Vol. 48. - p. 75.

Kind H. [et al.] Nanowire Ultraviolet Photodetectors and Optical Switches [Journal] // Adv. Mater.. - 2002. - Vol. 14. - p. 158.

Koch W. and Friedlander S.K. The Effect of Particle Coalescence on the Surface Area of a Coagulating Aerosol [Journal] // J. Col. Interf. Sci.. - 1990. - Vol. 140. - p. 419.

Kraft M. Modelling of Particulate Processes [Journal] // KONA. - 2005. - Vol. 23. - p. 18.

Kubaschewski O. and Hopkins B.E. Oxidation of Metals and Alloys [Book]. - [s.l.] : Butterworths, 1967.

Kumar S. and Ramkrishna D. On the Solution of Population Balance Equations by Discretization I. A Fixed Pivot Technique [Journal] // Chem. Eng. Sci.. - 1996. - Vol. 51. - p. 1311.

Kumar S. and Ramkrishna D. On the Solution of Population Balance Equations by Discretization II. A moving Pivot Technique [Journal] // Chem. Eng. Sci.. - 1996. - Vol. 51. - p. 1333.

Laidler K. J., Glasstone S. and Eyring H. Application of the Theory of Absolute Reaction Rates to Heterogeneous Processes [Journal] // J. Chem. Phys.. - 1940. - Vol. 8. - pp. 659-667.

Lanczos C. Applied Analysis [Book]. - New York : Dover, 1988.

Landau L.D. and Lifshitz E.M. Fluid Mechanics [Book]. - New York : Pergamon Press, 1959.

Lee K.W. Change of Particle Size Distribution during Browning Coagulation [Journal] // J. Coll. Inter. Sci.. - 1983. - Vol. 92. - p. 315.

Leith D. Drag on Non-Spherical Objects [Journal] // Aerosol Science and Technology. - 1987. - Vol. 6. - p. 153.

- Litster J.D., Smit D.J. and Hounslow M.J.** Adjustable Descretized Population Balance for Growth and Aggregation [Journal] // A.I.Ch.E.. - 1995. - Vol. 41. - p. 591.
- Liu J. [et al.]** Flame Synthesis of Tin Oxide Nanorods: A Continuous and Scalable Approach [Journal] // J. Phys. Chem. C. - 2010. - Vol. 114. - p. 5867.
- Lothe J. and Pound G.M.** Reconsiderations of Nucleation Theory [Journal] // J. Chem. Phys.. - 1962. - Vol. 36. - p. 2080.
- Lovette M.A. [et al.]** Crystal Shape Engineering [Journal] // Ind. Eng. Chem. Res.. - 2008. - Vol. 47. - p. 9812.
- Lustman B.** Oxidation of Molybdenum in Air at 1100 to 1600 F [Journal] // Met. Prog.. - 1950. - Vol. 57. - p. 629.
- Lutz A. E. [et al.]** Oppdif: a Fortran Program for Computing Opposed-Flow Diffusion Flames [Report] / Sandia Sand96-8243. - 1997.
- Marchisio D.L. [et al.]** Quadrature Method of Moments for Population-Balance Equations [Journal] // AIChE. - 2003. - Vol. 49. - p. 1266.
- Marchisio D.L., Vigil R.D. and Fox R.O.** Quadrature Method of Moments for Aggregation-Breakage Processes [Journal] // J. Colloidal Inter. Sci.. - 2003. - Vol. 258. - p. 322.
- Markov I.V.** Crystal Growth for Beginners [Book]. - [s.l.] : World Science, 1941. - 2nd.
- McGraw R.** Description of Aerosol Dynamics by the Quadrature Method of Moments [Journal] // Aeros. Sci. Tech.. - 1997. - Vol. 27. - p. 255.
- Megaridis C.M. and Dobbins R.A.** Soot Aerosol Dynamics in a Laminar Ethylene Diffusion Flame [Journal] // Proc. Combust. Inst.. - 1988. - Vol. 22. - p. 353.

Merchan-Merchan W., Saveliev A.V. and Desai M. Volumetric Flame Synthesis of Well-Defined Molybdenum Oxide Nanocrystals [Journal] // Nanotech.. - 2009. - Vol. 20. - p. 475601.

Mueller M.E., Blanquart G. and Pitsch H. A joint volume-surface model of soot aggregation with the method of moments [Journal] // Proc. Combust. Inst. . - 2009. - Vol. 32. - p. 785.

Mueller M.E., Blanquart G. and Pitsch H. Hybrid Method of Moments for Modeling Soot Formation and Growth [Journal] // Comb. Flame. - 2009. - Vol. 156. - p. 1143.

Niven W.D. The Scientific Papers of James Clerk Maxwell [Book]. - New York : Dover Publications Inc., 1965. - Vol. 2.

Pan Z.W., Dai Z.R. and Wang Z.L. Nanobelts of Semiconducting Oxides [Journal] // Science. - 2001. - Vol. 291. - p. 1947.

Peterson R.C. and Fassel W.M. Technical Report VI [Report]. - [s.l.] : Army Ordinance Contract DA-04-495 ORD-237, 1954.

Peterson T.W., Gelbard F. and Seinfeld J.H. Dynamics of Source-Reinforced, Coagulating and Condensing Aerosol [Journal] // J. Coll. Inter. Sci.. - 1978. - Vol. 63. - p. 426.

Pratsinis S. E. Flame Aerosol Synthesis of Ceramic Powders [Journal] // Prog. Energy Combust. Sci.. - 1998. - Vol. 24. - p. 197.

Pratsinis S.E. Simultaneous Nucleation Condensation and Coagulation in Aerosol Reactors [Journal] // J. Coll. Interface Sci.. - 1988. - Vol. 124. - p. 416.

Pratsinis SE. Simultaneous Nucleation, Condensation and Coagulation in Aerosol Reactors [Journal] // J. Coll. Inter. Sci.. - 1988. - Vol. 124. - p. 416.

Press W.H. and Teukolsky S.A. Orthogonal Polynomials and Gaussian Quadrature with Nonclassical Weight Functions [Journal] // Comp. Phys.. - 1990. - Vol. 4. - p. 423.

Pruppacher H. R. and Klett J. D. Microphysics of Clouds and Precipitation [Book]. - Boston : Reidel, 1980.

Reiss H., Katz J.L. and Cohen E.R. Translation-Rotation paradox in Theory of Nucleation [Journal] // J. Chem. Phys.. - 1968. - Vol. 48. - p. 5553.

Reist P.C Aerosol Science and Technology [Book]. - New York : McGraw-Hill, 1993. - 2nd.

Rosner D. E. Flame Synthesis of Valuable Nanoparticles: Recent Progress, Current Needs in Areas of Rate Laws, Population Dynamics and Characterization [Journal] // Ind. Eng. Chem. Res.. - 2005. - Vol. 44. - p. 6045.

Rosner D.E. The Apparent Chemical Kinetics of Surface Reactions in External Flow Systems - Diffusional Falsification of Activation Energy and Reaction Order [Report]. - [s.l.] : AeroChem Res. Labs. Inc., 1961.

Rosner D.E., McGraw R. and Tandon P. Multivariate Population Balances via Moment and Monte Carlo Simulation Methods [Journal] // Ind. Eng. Chem. Res.. - 2003. - Vol. 42. - p. 2699.

Roth P. Particle Synthesis in Flames [Journal] // Proc. Combust. Inst.. - 2007. - Vol. 31. - p. 1773.

Saburi T. [et al.] Oxygen Plasma Interaction with Molybdenum: Formation of Volatile Molybdenum Oxides [Journal] // Journal of Plasma and Fusion Research. - January 2001. - 1 : Vol. 78.

Schryer D.R. and Modisette J.L. An investigation of the effects of gaseous diffusion on the rate of oxidation of a metal forming a volatile oxide [Report]. - [s.l.] : NASA Langley Research Center, 1961.

Schryer D.R. and Walberg G.D. A Theoretical and Experimental Investigation of the Oxidation of Molybdenum at Temperatures at which its Trioxide is Volatile [Report] / Langley Research Center ; NASA. - 1966.

Semmel J.W. High Temperature Materials [Book]. - New York : J. Wiley & Sons, Inc., 1959.

Simmad M. and Spliners A. Kinetics and Mechanism of the Oxidation of Molybdenum [Journal] // Trans. AIME. - 1955. - Vol. 203. - p. 1011.

Smith G.P. [et al.] http://www.me.berkeley.edu/gri_mech/ [Online] // GRI Mech 3.0.

Song L. X. [et al.] Molybdenum Oxide Nanoparticles: Preparation, Characterization, and Application in Heterogeneous Catalysis [Journal] // J. Mater. Chem.. - 2011. - Vol. 21. - p. 7982.

Srivastava S. [et al.] Volumetric Flame Synthesis of One-Dimensional Molybdenum Oxide Nanostructures [Journal] // Proc. Combust. Inst.. - 2014.

Sunagawa I. Crystals: Growth, morphology and Perfection [Book]. - [s.l.] : Cambridge Univ. Pr., 2005.

Tyndall J. On the Action of Rays of High Refrangibility Upon Gaseous Matter [Journal] // Proc. Roy. Soc.. - 1870. - Vol. 160. - p. 333.

Vekilov P.G. Dense Liquid Precursor for the Nucleation of Ordered Solid Phases from Solutions [Journal] // Crystal Growth and Design. - 2004. - Vol. 4. - p. 4.

- Venables J.A.** Atomic Processes in Crystal Growth [Journal] // Surface Science. - 1994. - Vol. 299. - p. 798.
- Volmer M. and Weber A.** Nucleation in Supersaturated Products [Journal] // Z. Phys. Chem.. - 1926. - Vol. 119. - p. 277.
- Waldmann L.** Über die Kraft eines inhomogenen Gases auf kleine suspendierte Kugeln [Journal] // Zeitschrift Naturforschung Teil A. - 1959. - Vol. 14. - p. 589.
- Wegner K. and Pratsinis S.E.** Innovative Processing of Films and Nanocrystalline Powders [Book]. - London : Imperial College Press, 2002.
- Whitby K.T.** Determination of Aerosol Growth Rates in the Atmosphere Using Lumped Aerosol Dynamics [Journal] // J. Aero. Sci.. - 1981. - Vol. 12. - p. 174.
- Wikipedia** Periodic Table [Online] // Wikipedia, The Free Encyclopedia. - 2014.
- Wooldridge M. S.** Gas-Phase Combustion Synthesis of Particles [Journal] // Prog. Energy Combust. Sci.. - 1998. - Vol. 24. - p. 63.
- Xiao Y. [et al.]** "Plugging into Enzymes": Nanowiring of Redox Enzymes by a Gold Nanoparticle [Journal] // Science. - 2003. - Vol. 299. - p. 1877.
- Xu X. [et al.]** A Kinetic Model for Nanocrystal Morphology Evolution [Journal] // Chem. Phys. Chem.. - 2007. - Vol. 8. - p. 703.
- Yau S.T. and Vekilov P.G.** Direct Observation of Nucleus Structure and Nucleation Pathways in Apoferritin Crystallization [Journal] // J. Amer. Chem. Soc.. - 2001. - Vol. 123. - p. 1080.
- Yu S. [et al.]** A Two-Dimensional Discrete Sectional Method for Metal Aerosol Dynamics in a Flame [Journal] // Aerosol Sci. Technol.. - 1998. - Vol. 28. - p. 185.

- Zachariah M.R. [et al.]** Silica Particle Synthesis in a Counterflow Diffusion Flame Reactor [Journal] // Comb. Flame. - 1989. - Vol. 78. - p. 287.
- Zhao B. [et al.]** [Journal] // Proc. Comb. Inst.. - 2005. - Vol. 30. - p. 2569.
- Zhao B. [et al.]** Particle size distribution function of incipient soot in laminar premixed ethylene flames: effect of flame temperature [Journal] // Proc. Combust. Inst.. - 2005. - Vol. 30. - p. 1441.
- Zhou J. [et al.]** Synthesis of Large-Scaled MoO₂ Nanowire Arrays [Journal] // Chem. Phys. Lett.. - 2003. - Vol. 382. - p. 443.
- Zhu W. and Pratsinis S E.** Synthesis of SiO₂ and SnO₂. Particles in Diffusion Flame Reactors [Journal] // AIChE. - 1997. - Vol. 43. - p. 2657.
- Zhuo Y. [et al.]** A Reagentless Amperometric Immunosensor Based on Gold Nanoparticles/Thionine/Nafion-Membrane-Modified Gold Electrode for Determination of α -1-Fetoprotein [Journal] // Electrochem. Commun.. - 2005. - Vol. 7. - p. 355.

APPENDICES

Appendix A

Derivation for Rate of Oxidation of Molybdenum

NOMENCLATURE

C	concentration of oxygen (kg/m^3)
C_p	specific heat capacity (J/kg K)
D	diffusivity (m^2/s)
h	heat transfer coefficient ($\text{W/m}^2 \text{K}$)
h_m	mass transfer coefficient ($\text{kg/m}^2 \text{s}$)
k	rate of oxidation at the surface expressed as oxygen consumed ($\text{kg/m}^2 \text{s}$)
M	molecular weight
Nu	Nusselt number
Pr	Prandtl number
Sc	Schmidt number
Re	Reynolds number
T	temperature (K)
U	average speed of gas molecules (m/s)

Y	mass fraction
κ	thermal conductivity (W/m K)
μ	viscosity (kg/m s)
ρ	density (kg/m ³)

The oxidation of molybdenum in the high temperature environment of the flame begins with the adsorption of oxygen on the surface of the molybdenum probe (Rosner, 1961) (Bartlett, et al., 1958). Some part of the adsorbed oxygen reacts with the molybdenum by the reaction given in Section 5.3

$$k = \frac{CU}{4} \exp\left(-\frac{E_a}{RT}\right) \quad (\text{A.1})$$

$$U = \sqrt{\frac{8RT}{\pi M_{O_2}}}$$

The portion of the formula A.1 outside the exponent denotes the flux of oxygen on the surface of the molybdenum probe and the exponential denotes the activated portion of the adsorbed gas.

In terms of mass fraction this can also be written as –

$$k = \frac{Y_{O_2,w} \rho U}{4} \exp\left(-\frac{E_a}{RT}\right) \quad (\text{A.2})$$

Since the oxidation of molybdenum is fast for steady state conditions rate of consumption of oxygen on the probe surface should be equal to the rate of transport of oxygen to the surface

$$\dot{m}_{O_2} = h_m (Y_{O_2} - Y_{O_2,w}) \quad (\text{A.3})$$

Since $k = \dot{m}_{O_2,w}$

$$k = h_m (Y_{O_2} - Y_{O_2,w}) \quad (\text{A.4})$$

Eliminating $Y_{O_2,w}$ from A.2 and A.4 since it is unknown

$$k = \frac{Y_{O_2} h_m \frac{U}{4} \exp\left(-\frac{E_a}{RT}\right)}{\frac{U}{4} \exp\left(-\frac{E_a}{RT}\right) + \frac{h_m}{\rho}} \quad (\text{A.5})$$

Equation A.5 is the general equation for the oxidation of molybdenum. It contains the chemical as well as the mass transfer terms. Depending on a limiting scenario one of them may dominate (Schryer, et al., 1966).

In the case for chemical control A.5 becomes –

$$k = Y_{O_2} \rho \frac{U}{4} \exp\left(-\frac{E_a}{RT}\right)$$

In the case of transport control A.5 becomes –

$$k = Y_{O_2} h_m$$

Values of E_a are known (Schryer, et al., 1966) but the value of the mass transfer coefficient is unknown. Values for mass transfer coefficient are relatively difficult to be found in the literature. However the values of heat transfer coefficient have been extensively studied and are widely available (Eckert, 1959). Suitable analogies can be made between the heat and mass transfer coefficients if certain assumptions are made.

Here we assume a value of unity for the Lewis number ($Le = 1$)

This is quite a valid assumption for oxygen.

Lewis number is the ratio of Schmidt number to Prandtl number

$$\text{Pr} = \frac{\mu C_p}{\kappa}$$

$$\text{Sc} = \frac{\mu}{\rho D}$$

Equating Pr and Sc and multiplying h_m on both sides

$$h_m C_p = h$$

$$\frac{h}{\kappa} = \frac{h_m}{\rho D_{O_2}} \quad (\text{A.6})$$

Now Nusselt number $Nu = \frac{hx}{\kappa}$

For flow over a thin cylinder

$$Nu_{cyl} = 0.3 + \frac{0.62 \text{Re}^{1/2} \text{Pr}^{1/3}}{\left[1 + \left(\frac{0.4}{\text{Pr}}\right)^{2/3}\right]^{1/4}} \left[1 + \left(\frac{\text{Re}}{282000}\right)^{5/8}\right]^{4/5} \quad (\text{A.7})$$

Using the definition of Nusselt number, A.6 and A.7 we can say that

$$h_m = \frac{Nu_{cyl}}{d} \rho D_{O_2} \quad (\text{A.8})$$

The value of h_m found from A.8 is then fed into A.5 and the rate of oxidation can now be conveniently calculated.

Appendix B

Product – Difference Algorithm

```
% M is the moment set
n = size(M);
n = n(1,1);
N = n/2;
mu = M;
mu = mu/mu(1);
ms = mu(2);
i=[2:n]';
mu(i) = mu(i)./ms.^(i-1);
P = zeros(n+1,n+1);
P(1,1) = 1;
i=[1:n]';
P(i,2) = mu.*(-1).^(i-1);
for j=3:n+1
for i=1:n-j+3-1
    P(i,j) = P(1,j-1)*P(i+1,j-2) - P(1,j-2)*P(i+1,j-1);
end
end
alph =zeros(n,1);
alph(1) = 0;
i=[2:n]';
alph(i) = P(1,i+1)./(P(1,i).*P(1,i-1));
i=[1:N]';
a=zeros(N,1);
b=a;
a(i) = alph(2*i) + alph(2*i-1);
i=[1:N-1]';
b(i) = sqrt(alph(2*i+1).*alph(2*i));
J=diag(a,0) + diag(b(1:N-1),1) + diag(b(1:N-1),-1);
[V, x] = eig(J);
absc_wts = [diag(x) [V(1,:).^2]'*M(1)];
i = [1:3]';
r(i) = absc_wts(i,1);
```

```
w(i) = absc_wts(i,2);
```

Appendix C

Derivation for the Thermophoretic Force Expression in Free Molecular Regime

Assume a particle of diameter d placed in the middle of a cylinder having the same diameter but with a length equal to twice the length of the mean free path i.e. 2λ . Gas molecules are having a mass m traversing inside the cylinder on both the sides of the particle. They collide with the particle on either side and impart their moment to it(Reist, 1993).

Assuming the number of molecules per unit volume on the right and the left side of the particle to be n_1 and n_2 . Their respective velocities are v_1 and v_2

Therefore the momentum imparted to the particle per unit time from the right side is –

$$P_1 = \left(\frac{1}{6} n_1 v_1 \right) \left(\frac{\pi}{4} d^2 \right) (m v_1) \quad (\text{C.1})$$

Momentum from the left side is –

$$P_2 = \left(\frac{1}{6} n_2 v_2 \right) \left(\frac{\pi}{4} d^2 \right) (m v_2) \quad (\text{C.2})$$

Net change in momentum per unit time is –

$$\Delta P = -\left(\frac{1}{3}\right)\left(\frac{\pi}{4}d^2\right)\left(\frac{n_1 m v_1^2}{2} - \frac{n_2 m v_2^2}{2}\right) \quad (\text{C.3})$$

Assuming $n_1 \approx n_2 \approx n$

$$F_T = -\left(\frac{n}{3}\right)\left(\frac{\pi}{4}d^2\right)\left(\frac{1}{2}m v_1^2 - \frac{1}{2}m v_2^2\right) \quad (\text{C.4})$$

Now for a gas molecule $\frac{1}{2}m v^2 = \frac{3}{2}kT$ and multiplying equation C.4 by $\frac{\lambda}{\lambda} = 1$

$$F_T = -\frac{n\pi d^2}{4}k\left(\frac{T_1 - T_2}{2\lambda}\right)\lambda \quad (\text{C.5})$$

T_1 and T_2 are the temperatures on the right and the left side of the particle

Since 2λ is the total length of the cylinder therefore

$$\left(\frac{T_1 - T_2}{2\lambda}\right) = \nabla T \text{ and by ideal gas law } nk = \frac{p}{T}$$

Hence equation C.5 becomes

$$F_T = -\frac{\pi}{4}d^2 p \lambda \frac{\nabla T}{T} \quad (\text{C.6})$$

This is the final expression for thermophoretic force. However using momentum transfer method (Waldmann, 1959) found that –

$$F_T = -\frac{\pi}{4}d^2 p \lambda \frac{\nabla T}{T} = -\frac{1}{2}\pi\mu\nu \frac{d^2}{\lambda} \frac{\nabla T}{T} \quad (\text{C.7})$$

where μ and ν are dynamic and kinematic viscosities

Appendix D

Solution Scheme for Calculating the Diffusion Flux from the Lateral Surfaces

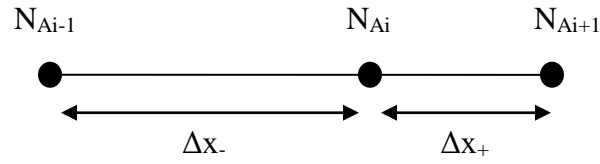
Let N be the number of atoms condensing on the nanorod surface and let N_A be the number of monomer atoms that have been adsorbed on the whisker surface per unit area per unit time. These adsorbed atoms within migrating distance of the nanorod ends diffuse and join to increase the length of the structure. To find the atom diffusion flux we need to solve

$$\frac{\partial N_A}{\partial x^2} + \frac{N}{D} - \frac{N_A}{D\tau} = 0 \quad (\text{D.1})$$

$$N = \frac{P}{\sqrt{2\pi mkT}}$$

To solve this equation a variable grid has been setup on the nanorod lateral surface. The grid spacing varies with the nanorod length and the concentration gradients of the surface atoms.

A central difference scheme has been employed to discretize (D.1)



$$\begin{aligned}
 & \frac{2}{\Delta x_+ + \Delta x_-} \left[\frac{N_{A_{i+1}} - N_{A_i}}{\Delta x_+} - \frac{N_{A_i} - N_{A_{i-1}}}{\Delta x_-} \right] + \frac{N}{D} - \frac{N_{A_i}}{D\tau} \\
 & \frac{2}{\Delta x_+ (\Delta x_+ + \Delta x_-)} N_{A_{i+1}} - \left[\frac{2}{\Delta x_+ (\Delta x_+ + \Delta x_-)} + \frac{2}{\Delta x_- (\Delta x_+ + \Delta x_-)} + \frac{1}{D\tau} \right] N_{A_i} \\
 & + \frac{2}{\Delta x_- (\Delta x_+ + \Delta x_-)} N_{A_{i-1}} = -\frac{N}{D}
 \end{aligned} \tag{D.2}$$

Boundary conditions –

- i. at $x = 0$, $N_A = 0$
- ii. at $x = h$, $N_A = 0$ where h is the instantaneous whisker length

Equation (D.2) forms a tridiagonal system of equations in N_A and is solved using the Thomas algorithm (Anderson Jr., 1995)

Appendix E

Dillmann-Meier Theory

Dillmann and Meier (Dillmann, et al., 1989)(Dillmann, et al., 1991) have proposed a new droplet model whose basis is the semiphenomenological droplet model for the Gibbs free energy of an i-mer. The expression for free energy also includes virial coefficients, pressure and density of the gas at critical points. The model incorporates translational, rotational, vibrational and configurational degrees of freedom of the cluster as well as variation of surface tension with cluster size (Dillmann, et al., 1991).

$$\Delta G = k_n \sigma n^{2/3} + \tau k_B T \ln n - k_B T \ln q_o V - n k_B T \ln S \quad (\text{E.1})$$

where k_n describes deviations of the surface energy of a n molecule cluster compared to a macroscopic spherical liquid droplet. The second and the third terms take into account translational, rotational, vibrational and configurational parts of the droplet free energy whereas the first and last terms allow the inclusion of surface energy of the cluster and relaxation of the metastable state.

k_n , τ and q_o are empirical parameters introduced to calculate the various contributions unlike the other nucleation theories because no equation of state exists which provides the derivatives of density with respect to pressure correctly for all n molecules (Dillmann, et al., 1989). Therefore –

$$k_n = 1 + \alpha_1 n^{-1/3} + \alpha_2 n^{-2/3}$$

where

$$\alpha_1 = \frac{(k_2 - 1) - (k_1 - 1)2^{-2/3}}{2^{-1/3} - 2^{-2/3}}, \quad \alpha_2 = \frac{(k_2 - 1) - (k_1 - 1)2^{-1/3}}{2^{-1/3} - 2^{-2/3}}$$

Equating just the first two terms of the virial expansion we have-

$$k_1 = -\left(\frac{1}{\theta}\right) \ln\left(\frac{P_{sat}}{q_o k_B T}\right), \quad k_2 = -\left(\frac{1}{2^{2/3} \theta}\right) \ln\left[-\left(\frac{P_{sat}}{q_o k_B T}\right)^2 2^{x-1} q_o B\right] \quad (E.2)$$

Where B is the second virial coefficient and θ is the abbreviation for $\frac{\sigma_s}{kT}$

Finally the rate of nucleation is obtained as –

$$J_{DM} = \frac{1}{3} \sqrt{\frac{\theta}{\pi} \left[1 + \alpha_1 (n_c)^{-1/3} + \frac{9\tau}{2\theta} (n_c) \right]^{-2/3}} \frac{s_1 P_{sat}}{\sqrt{2\pi m k_B T}} \rho_c$$

$$\rho_c = q_o \exp\left[-k_n \theta (n_c)^{-2/3} - \tau \ln n_c + n_c \ln S\right]$$

where the size of the critical nucleus is found real root of cubic equation

$$\tau x^3 + \frac{1}{3} \alpha_1 \theta x^2 + \frac{2}{3} \theta x - \ln S$$

$$x = (n_c)^{-1/3}$$

when we neglect additional degrees of freedom i.e. $\tau = 0$ and take a macroscopic droplet i.e.

$k_n = 1$ then equation (E.2) yields the expression for CNT nucleation rate given by Becker-

Doring.

Comparison of Dillmann – Meier Theory and Classical Nucleation Theory

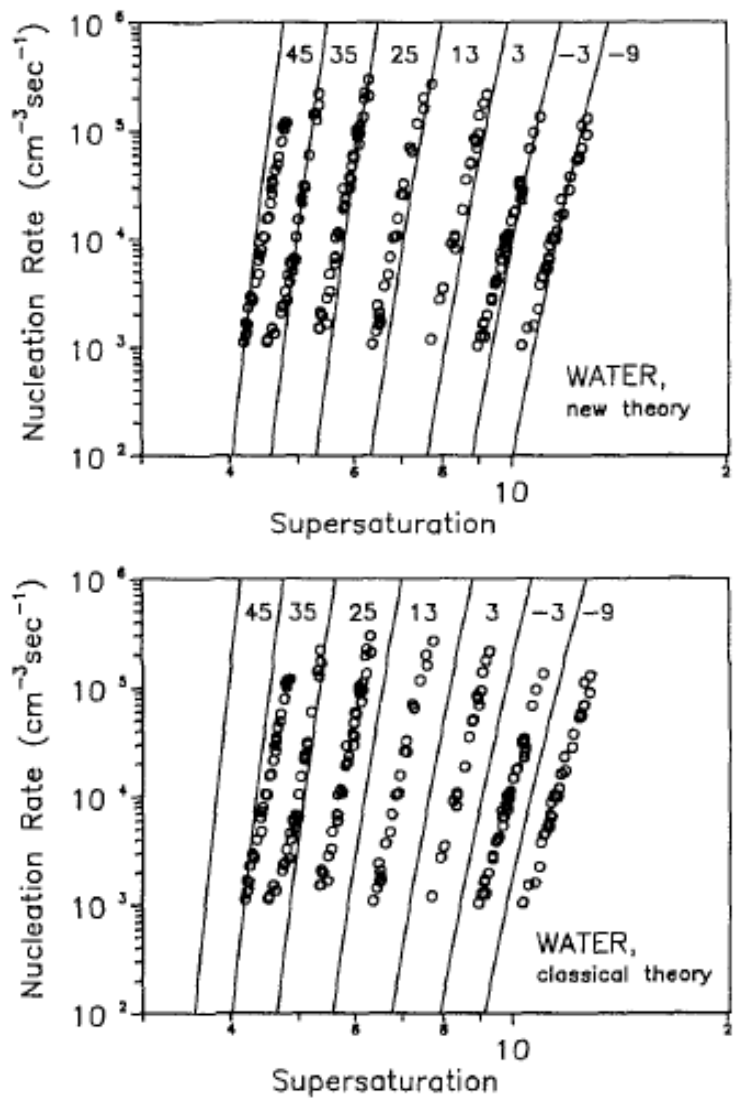


Figure E-1: Comparison of Dillmann - Meier Theory with CNT (Dillmann, et al., 1989)

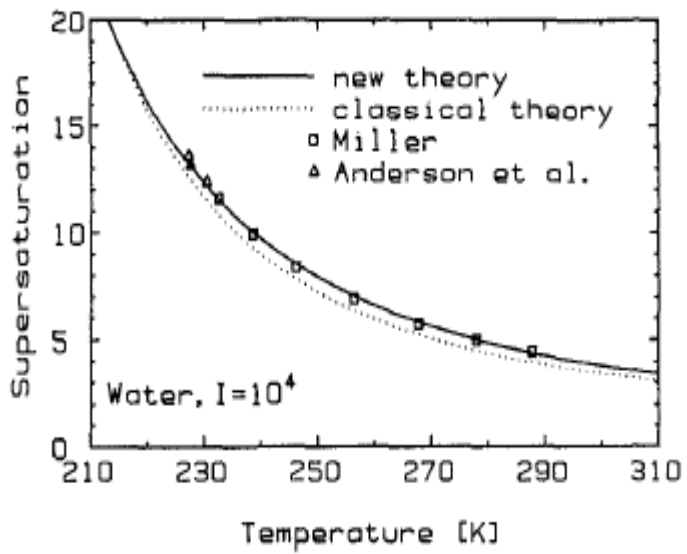
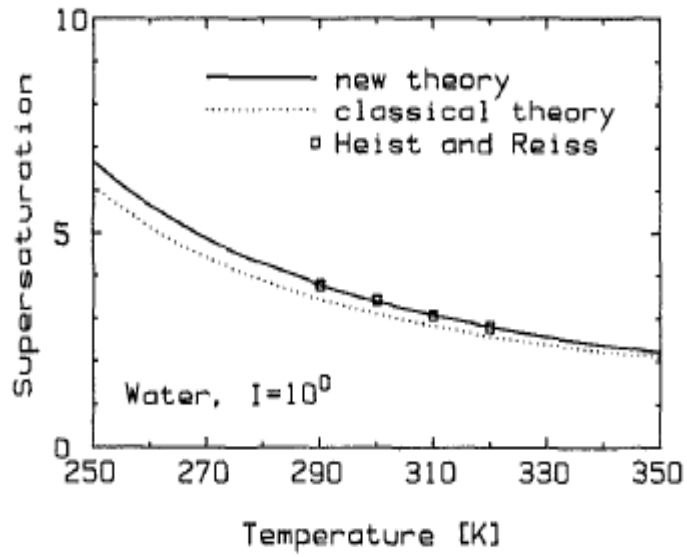


Figure E-2: Comparison of Dillmann - Meier Theory (solid line) and CNT (dotted line)

(Dillmann, et al., 1989)

As seen in Figure E-1 the rate of nucleation of water as predicted by CNT is too high by a factor of 10^2 - 10^3 whereas the Dillmann-Meier theory predicts the rate within the first order of magnitude. Figure E-2 also shows a better agreement of experimental data with the Dillmann-Meier theory. Although the CNT results seem quite close to the experimental results of supersaturation even small errors in supersaturation calculations can result in large errors in nucleation rates due to the exponential dependence of nucleation rate on supersaturation.

Appendix F

Mass Diffusivity Data for Various Species using Cantera

<i>Species</i>	<i>Diffusivity (m²/s)</i>
H2	7.93E-05
H	0.000124531
O	3.27E-05
O2	1.95E-05
OH	3.20E-05
H2O	2.28E-05
HO2	2.07E-05
H2O2	2.05E-05
C	3.09E-05
CH	3.50E-05
CH2	2.31E-05
CH2(s)	2.31E-05
CH3	2.26E-05
CH4	2.25E-05
CO	2.07E-05
CO2	1.57E-05
HCO	1.57E-05
CH2O	1.56E-05
CH2OH	1.54E-05
CH3O	1.54E-05
CH3OH	1.52E-05
C2H	1.68E-05
C2H2	1.66E-05
C2H3	1.65E-05
C2H4	1.60E-05

C2H5	1.49E-05
C2H6	1.47E-05
HCCO	2.52E-05
CH2CO	1.34E-05
HCCOH	1.34E-05
N	2.93E-05
NH	3.45E-05
NH2	3.37E-05
NH3	2.21E-05
NNH	2.05E-05
NO	2.05E-05
NO2	1.73E-05
N2O	1.55E-05
HNO	2.06E-05
CN	2.06E-05
HCN	1.53E-05
H2CN	1.52E-05
HCNN	2.52E-05
HCNO	1.56E-05
HOCN	1.56E-05
HNCO	1.56E-05
NCO	1.57E-05
N2	2.22E-05
Ar	1.99E-05
C3H7	1.14E-05
C3H8	1.13E-05
CH2CHO	1.33E-05
CH3CHO	1.32E-05

Appendix G

Thermal Diffusivity Data for Various Species using Cantera

<i>Species</i>	<i>Thermal diffusivity (m²/s)</i>
H2	-3.13E-16
H	-1.97E-22
O	-1.18E-20
O2	1.30E-07
OH	-6.67E-20
H2O	-1.93E-18
HO2	5.88E-22
H2O2	3.84E-21
C	-8.51E-23
CH	-1.74E-23
CH2	1.66E-23
CH2(s)	2.61E-24
CH3	-9.40E-23
CH4	-1.16E-20
CO	-9.14E-22
CO2	3.51E-20
HCO	-2.19E-23
CH2O	2.73E-22
CH2OH	-2.13E-23
CH3O	-3.44E-23
CH3OH	7.71E-22
C2H	2.74E-23
C2H2	-5.30E-22
C2H3	-4.29E-23
C2H4	2.83E-22

C2H5	2.14E-23
C2H6	-9.43E-25
HCCO	1.91E-22
CH2CO	8.73E-20
HCCOH	6.53E-22
N	-3.93E-23
NH	-1.38E-23
NH2	-1.47E-23
NH3	-9.86E-22
NNH	-4.18E-23
NO	8.99E-22
NO2	7.74E-21
N2O	1.62E-21
HNO	2.89E-22
CN	-9.02E-23
HCN	1.53E-23
H2CN	-2.49E-23
HCNN	1.30E-21
HCNO	4.88E-23
HOCN	2.97E-20
HNCO	3.93E-21
NCO	1.74E-19
N2	-1.30E-07
Ar	3.35E-23
C3H7	1.82E-22
C3H8	2.36E-23
CH2CHO	1.28E-23
CH3CHO	3.09E-21